

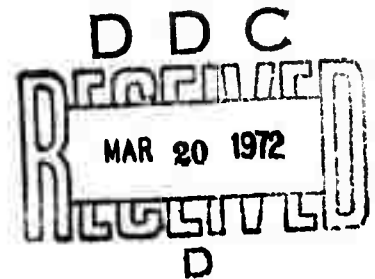


SEMI-ANNUAL TECHNICAL REPORT

RESEARCH ON AMORPHOUS MATERIALS

Contract DAHC04 70 C 0044

July 1 - December 31, 1971



The views and conclusions contained in this document are those of the authors and should not be interpreted as necessarily representing the official policies, either expressed or implied, of the Advanced Research Projects Agency or the U. S. Government.

Approved for public release; distribution unlimited.

BEE
AD719419

Reproduced by
NATIONAL TECHNICAL
INFORMATION SERVICE
Springfield, Va. 22151

CENTER FOR MATERIALS RESEARCH

112
CMR-71-24

STANFORD UNIVERSITY • STANFORD, CALIFORNIA

DISCLAIMER NOTICE

THIS DOCUMENT IS THE BEST
QUALITY AVAILABLE.

COPY FURNISHED CONTAINED
A SIGNIFICANT NUMBER OF
PAGES WHICH DO NOT
REPRODUCE LEGIBLY.

SEMI-ANNUAL TECHNICAL REPORT

July 1 - December 31, 1971

Sponsored by
Advanced Research Projects Agency
ARPA Order No. 1562

Program Code Number: OD10

Contractor: Stanford University

Contract No. DAHC04 70 C 0044

Principal Investigators: W. E. Spicer
Phone: (415) 321-2300, Ext. 4643

A. Bienenstock, Ext. 2617

R. H. Bube, Ext. 2535

Effective Date of Contract: June 1, 1970

Contract Expiration Date: May 31, 1972

Amount of Contract: \$171,525

Contract Title: RESEARCH ON AMORPHOUS MATERIALS

CENTER FOR MATERIALS RESEARCH
STANFORD UNIVERSITY
STANFORD, CALIFORNIA 94305
(415) 321-2300, Ext. 4118

CMR-71-24

Approved for public release; distribution unlimited.

TABLE OF CONTENTS

PHOTOEMISSION AND OPTICAL WORK - W. E. Spicer	1
STRUCTURAL STUDIES - A. Bienenstock	8
PHOTOCONDUCTIVITY IN AMORPHOUS CHALCOGENIDES - R. H. Bube	14

APPENDICES

- A - "The Density of States of Crystalline and Amorphous Ge and Si," W. E. Spicer and T. M. Donovan
- B - "Photoemission Investigation of Amorphous Si and Ge," D. T. Pierce, C. G. Ribbing, and W. E. Spicer
- C - "Investigation of the Band Edges of Amorphous Ge and Si," W. E. Spicer, T. M. Donovan, and J. E. Fischer
- D - "Impurity Electrons in Amorphous Germanium
A Photoemission Argument for the Mott Model," C. G. Ribbing and W. E. Spicer
- E - "UV Dielectric Constants of a-Ge as a Function of Film Density," R. S. Bauer, F. L. Galeener, and W. E. Spicer
- F - "Photoemission Investigation of Amorphous Germanium," C. G. Ribbing, D. T. Pierce, and W. E. Spicer
- G - "Electronic Structure of Amorphous and Polycrystalline GeTe," G. B. Fisher and W. E. Spicer
- H - "Calculation of the Intercrystalline Interference Contribution to the Scattering of X-Rays by Arrays of Small Crystallites," F. Betts and A. Bienenstock
- I - "Neutron and X-Ray Diffraction Radial Distribution Studies of Amorphous $\text{Ge}_{.17}\text{Te}_{.83}$," F. Betts, A. Bienenstock, D. T. Keeting, and J. deNeufville.
- J - "Structure and Bonding in Amorphous $\text{Ge}_x\text{Te}_{1-x}$ Alloys," F. Betts, A. Bienenstock, and C. W. Bates, Jr.
- K - "Radial Distribution Studies of Glassy $\text{Ge}_x\text{S}_{1-x}$ Alloys," S. C. Rowland, S. Narasimhan, and A. Bienenstock
- L - "Analysis of Photoconductivity in Amorphous Chalcogenides," T. C. Arnoldussen, R. H. Bube, E. A. Fagen, and S. Holmberg

PHOTOEMISSION AND OPTICAL WORK

Introduction (W.E. Spicer)

The photoemission and optical work accomplished during this period can be divided into two parts: Continuing work on amorphous Ge and Si*, and work of more recent origin on increasingly complex systems; such as, GeTe and As₂Se₃.

*The Si is partially supported by contract 5220 with the U. S. Army Research Office - Durham.

I. Studies of Amorphous Ge and Si

W. E. Spicer, C. G. Ribbing, and D. T. Pierce

In the Ge and Si work, our prior work has emphasized samples prepared so as to minimize the effect of extrinsic defects. It is now clear that differences between our own results and those obtained elsewhere are due to differences in sample preparation. Further, we concluded from examination of the existing data, that these differences are due to large densities of extrinsic defects in much of the work done elsewhere. In order to obtain better insight into this, much of our recent amorphous Ge and Si work has been directed at developing better methods of sample preparation and specification. Because of the limited effort available at Stanford, cooperation with the Michelson Laboratory at China Lake, California, and Xerox Laboratory in Palo Alto has been important.

The Si work has undertaken principally to see if the general conclusions which we had previously drawn from the work on amorphous Ge also apply to amorphous Si. This appears to be the case. In particular, it appears that the lack of importance of \bar{k} as an optical selection rule is true for Si as well as Ge. In addition, the loss of density of states structure due to Bragg gaps (see Appendix A and B) occurs in amorphous Si as well as Ge. The sharp band edged (see Appendix C) which occur in properly prepared amorphous Ge also occur in properly prepared amorphous Si; however, as the literature shows (see Appendices D and F; and Ref. 1), if sufficient care is not taken in sample preparation, Si, as well as Ge (see Ref. 2), can be prepared which does not exhibit sharp band edge.

In Appendix C we present criteria for the preparation of materials sufficiently free of defects so that sharp band edges are obtained. If one examines the literature, good correlation is found between these criteria and the occurrence of sharp edges. However, from density measurements,³ electron micrograph studies,⁴ and the newly

developed optical reflective methods discussed below, it is clear that sharp edges can occur even when measurable numbers of defects in the form of microvoids are present in the films; however, the band gap energy is changed by the presence of defects^{2,3} even though it stays sharp. It is suggested that these band edge shifts are due to internal strains produced by the microvoids and that more massive densities of defects or other types of defects are necessary to destroy the sharp band edge.

Galeener⁵ has developed a theory relating the presence of microvoids to changes in the visible and ultra-violet reflectivity from amorphous films. He analyzes the data of Donovan, Ashley, and Spicer in terms of a system of plate-like microvoids perpendicular to the surface. This system is in remarkable agreement with the pattern of microvoids found by Donovan and Heinemann in their electron micrograph study.

Experimental work done at Stanford in collaboration with the Xerox Laboratory has measured the change in reflectance as the sample is deposited on substrates at various temperatures so as to reduce the microvoid density. Some of those results are given in Appendix E. As can be seen from that paper, the experimental results are in good agreement with theory. Of extreme importance is the fact that such measurements provide a very sensitive and relatively easy method by which the presence of microvoids can be detected and critical information concerning their shape and orientation obtained.

II. Summary and Future Plans

It is now clear that the properties of amorphous Ge and Si can be vastly changed by the presence of microvoids and/or other defects in the films. Sharp absorption edges can be destroyed if the preparation conditions are sufficiently bad; however, if reasonable care in preparation is taken, sharp edges can be produced. For certain types and magnitudes of microvoids the sharp edge is retained but the value of the band gap may be a function of the microvoid density. In the range of imperfections where sharp edges occur the microvoid density and geometry has been well defined. However, for the case where the sample preparation is so far from ideal that the sharp edge is destroyed, very little is known about the details of the defects. In the coming months, we will attempt to make such films and learn more about the details of the defects.

In relation to theoretical work, our sample preparation, specification, and band edge studies have shown that defect free amorphous Ge and Si can be produced which approaches the perfection of the Polk-Turnbull model.⁶ Weaire has shown that if the local order in amorphous Ge and Si approaches sufficiently closely the local order in the crystalline material that a sharp band edge remains in the amorphous material. The fact that we can make amorphous Ge and Si which approaches the Polk-Turnbull ideal model and which has sharp band edges shows that the local order in amorphous Ge and Si can be sufficiently like that of the crystalline material to preserve the sharp edge.

References:

1. T. E. Fischer and M. Erbudak, Phys. Rev. Letters 27, 1220 (1971)
2. M. L. Theye, Optics Comm. 2, 329 (1970); Mat. Res. Bull 6, 103 (1971)
3. T. M. Donovan, E. J. Ashley, and W. E. Spicer, Phys. Rev. Letters 32A, 85 (1970)
4. T. M. Donovan and K. Heinemann, Phys. Rev. Letters 27, 1794 (1971)
5. F. L. Galeener, Phys. Rev. Letters 27, 421 (1971); 27, 1716 (1971)
6. D. Turnbull and D.E. Polk, Proc. of International Conf. on Amorphous and Liquid Semiconductors, Ann Arbor, Mich. (in press); J. Noncryst. Solids 5, 365 (1971)

III. Compound Amorphous Materials

G. B. Fisher, R. A. Powell, C. G. Ribbing and W. E. Spicer

A. Introduction

Once some understanding of pure, elementary amorphous materials is obtained, it becomes interesting to study amorphous materials containing more than one element. Of particular interest in such studies are the details of the bonds formed between the various components. One possible approach to such a study is to put large amounts of impurities in an elementary amorphous material such as Ge. The results of placing as much as 1% of As in Ge are given in Appendix G. As can be seen from that paper, little effect of this large As concentration is found in amorphous Ge. This is in agreement with the suggestions of Mott.

B. Studies of the Amorphous Ge-Te System (G.B. Fisher and W. E. Spicer)

The photoemission study of the $\text{Ge}_x\text{Te}_{1-x}$ system has progressed since the First Annual Technical Report. The bulk of our results along with our new ultra-violet reflectance data on amorphous and polycrystalline GeTe are reported in Appendix H. In our present work we are determining if there is significant tailing of the density of states into the gap in amorphous GeTe and we are setting up a photoemission experiment on another composition in the system near GeTe_2 .

We are currently conducting the experiment to look for the tailing of bulk states into the gap in amorphous GeTe. Since high energy edges of the EDCs move directly with photon energy, they are representative of the top of the valence band density of states. Photon energies just below threshold are used to excite any electrons lying above the valence band maximum. The position of the Fermi level and the resolution error of the photoemission analyzer are found by overcoating the substrate with a metal (Au) and measuring its high energy edge at low temperatures to minimize thermal broadening. It will be interesting to compare the results from amorphous GeTe which may have both structural and compositional disorder with the previous photoemission results from elemental amorphous semiconductors (i.e. Si^2 and $\text{Ge}^{3,4}$).

This experiment acts additionally as a check on the reproducibility of our previous work, since we are using a different source boule and a different substrate material (Ta). With the cooling capability, we can also see if there is any temperature dependence in the EDCs and their high energy edges in the range from 100°K to 300°K .

We continue to take care that our samples are accurately described structurally. Recently, amorphous films of GeTe evaporated under experimental conditions onto NaCl substrates have been sent to Dr. P. Chaudari of IBM Research Center,

Yorktown Heights, N.Y. He may determine a radial distribution function for thin film GeTe and examine the films for local order using dark field electron microscopy.

To expand our study of the $\text{Ge}_x\text{Te}_{1-x}$ system beyond GeTe, we are setting up a photoemission experiment to obtain an amorphous sample near the GeTe_2 composition. Because of the stringent requirements that photoemission experiment places on surface cleanliness, any sample studied should be prepared in situ. An electron-gun evaporation is the only available method which could hope to preserve the relative amounts of Ge and Te from charge to thin film. In fact, experience⁵ suggests that the higher vapor pressure of Te relative to Ge gives samples about 10% higher in Te than the original charge. Thus, a $\text{Ge}_{.43}\text{Te}_{.57}$ boule has been prepared to be used in the e-gun. The actual composition of the sample will be determined after the experiment. The EDCs measured will be studied for changes in the valence band density of states from GeTe and for evidence of tailing of states into the gap.

GeTe_2 is potentially quite interesting because experiments near this composition may give information to choose between several simple models which explain the GeTe data. The GeTe_2 composition itself is intriguing because it occurs at the maximum in the glass transition temperature and at the largest known bandgap in the Ge-Te system.⁶ It has been proposed⁶ that the uniqueness of this composition in the amorphous form is because the Ge atoms are four-fold coordinated and additionally are saturated with two-fold coordinated Te atoms, forming a structure analogous to SiO_2 with only Ge-Te bonds present.

This model converges well with one explanation of the two-peaked structure in the EDCs of amorphous GeTe. One possibility which has occurred to us is that above $x = .33$, $\text{Ge}_x\text{Te}_{1-x}$ may consist of only Ge-Ge and Ge-Te bonds. In this case, the first peak in the amorphous GeTe EDCs (at -1.5 eV) which coincides with the single peak in the amorphous Ge EDCs may be associated with the Ge-Ge bond and the second peak may then associate with the Ge-Te bond. In this view the EDCs from the GeTe_2 composition with only Ge-Te bonds would show a strongly enhanced second peak with respect to the first peak.

Another possible interpretation of the peaks in the EDCs of amorphous GeTe is to associate the first peak with the four-fold coordinated Ge atom and the second with the two-fold coordinated Te atom. The Ge in amorphous GeTe is postulated to be four-fold coordinated because, as mentioned above, the peak in the EDCs of four-fold coordinated amorphous Ge coincides with the first peak in the EDCs of amorphous GeTe. This would leave the Te atoms two-fold coordinated. In this case,

the prediction for the result of the GeTe_2 measurement would be for a slight enhancement of the second peak over the first, corresponding to the increase in atomic percent of tellurium.

The above models both assume four-fold and two-fold coordination for the Ge and Te atoms, respectively. Another viable alternative which is equally in accordance with recent structural work⁷ is three-fold coordination of both Ge and Te atoms, possibly in a highly distorted form of the six-fold coordination of crystalline GeTe. For the GeTe composition ($x = .5$), this presumably implies that the first and second nearest neighbors of each Ge and Te atom are three each of the opposite atomic type. Thus, the two peaks could be associated with the two lengths of Ge-Te bonds or again with the atoms themselves. However, in going to a composition near GeTe_2 , one has to have some Te-Te bonding occurring, and presumably some bonding of a two-coordinated nature. It is not clear what one would expect in the EDCs of the GeTe_2 composition under this model but it seems one might see more peaks or at least some considerable peak shifts as compared with GeTe composition data.

All of these models are obviously oversimplified as befits the state of the theory in the field. However, these models and their prediction for our next experiment give us some directions from which to approach a greater understanding of the $\text{Ge}_x\text{Te}_{1-x}$ system.

References:

1. G. B. Fisher and W. E. Spicer, to be published in Proceedings of Fourth International Conference on Liquid and Amorphous Semiconductors, Journal of Non-Crystalline Solids.
2. D. T. Pierce and W. E. Spicer, in press.
3. T. M. Donovan and W. E. Spicer, Phys. Rev. Letters 22, 1058 (1969); T. M. Donovan, W. E. Spicer, J. M. Bennett, and E. J. Ashley, Phys. Rev. B2, 397 (1970); W. E. Spicer and T. M. Donovan, J. Non-Cryst. Solids 2, 66 (1970).
4. C. G. Ribbing and W. E. Spicer, Physics Letters 37A, 85 (1971)
5. P. Chaudari, private communication
6. J. deNeufuille, to be published
7. F. Betts, A. Bienenstock, D.T. Keating and J. deNeufuille, to be published.

C. Studies of As_2Se_3 (R. A. Powell and W. E. Spicer)

At present, photoemission studies of As_2Se_3 are being made over a large range of photon energies (threshold to 12 eV) in ultrahigh vacuum at pressures $\lesssim 5 \times 10^{-11}$ Torr. Samples are prepared by the evaporation of high purity (99.999%) As_2Se_3 powder onto a polished Pt substrate. Film thickness and rate of deposition are monitored during the evaporation. The substrate temperature can be adjusted to obtain thin films with various degrees of long-range order -- ranging from crystalline to totally amorphous. The effect of group II dopants (Cu in this case) is also being studied. Future work will involve similar studies of high purity Se and As_2S_3 .

Both the distribution of photoemitted electrons and quantum yield have been measured for the heat cleaned Pt substrate. This data is in good agreement with previous photoemission studies of high purity Pt. Our measurements have also enabled us to determine that the work function of the copper coated collector is 4.4 ± 0.2 eV.

Both the photoemission flange and high vacuum system we are using have been built specifically for these experiments. The flange has been designed so that the substrate can be heated as high as 1000°C or cooled to liquid nitrogen temperature (77°K). The hemispherical collector can was made of spun conetic alloy to keep magnetic fields out of the collector can, thereby increasing EDC resolution. (Provision has also been made for cesiation to lower the sample work function.) The high vacuum system includes a high speed orb-ion pump in series with a titanium sublimation pump. This combination effectively handles the large gas loads produced during sample preparation and achieves a base pressure of $\sim 3 \times 10^{-11}$ Torr. Residual gas analysis of this new system showed the usual traces of He, H_2 , and cracked hydrocarbons.

STRUCTURAL STUDIES

As in the section of Photoemission and Optical Work, the structural work is on elemental amorphous materials and the alloy amorphous semiconductors in the Ge-Te, Ge-S and As-Se-X systems, where X is a metal or oxygen.

I. Studies of Amorphous Si

F. Betts and A. Bienenstock

A calculation of the intercrystalline interference contribution to the scattering of x-rays by arrays of small crystallites has been completed and prepared for publication. The manuscript is presented in Appendix H.

II. Structural Studies in the Ge-Te System

C. Bates, F. Betts, A. Bienenstock, D.T. Keating, J. deNeufville and Y. Verhelle

Neutron and x-ray diffraction studies of $\text{Ge}_{.17}\text{Te}_{.83}$ have now been completed and prepared for publication. The paper forms Appendix I of this report.

Similarly, work on x-ray induced photoemission and x-ray absorption edge spectroscopy has been completed and prepared for publication. The paper forms Appendix J of this report.

Our more recent work has been concerned with phase separation in the Ge-Te system. In the annual report, it was indicated that we had searched for phase separation in sputtered $\text{Ge}_x\text{Te}_{1-x}$ films with compositions, $x = 0.2, 0.3$ and 0.5 , as well as evaporated films with $x = 0.5$, using transmission electron microscopy. In all cases, no phase separation was observed.

In the intervening period, we have received a preprint of a paper by A. Feltz and co-workers on the $\text{Ge}_x\text{Se}_{1-x}$ system. They find two glass-forming regions in the system. One extends from x equal 0 to approximately 0.25.

The other goes from x equal approximately 0.39 to 0.42. These results are quite similar to, but not identical to, the results for the $\text{Ge}_x\text{S}_{1-x}$ system described in Appendix K of this report. Of particular interest to the concerns of this section is the result obtained by Feltz et al. that no phase separation is observed in the region with x less than 0.25. In the second glass-forming region, however, phase separation can be observed after a sample has been annealed at 350° C for 200 hours. These results, when taken together with all the radial distribution studies which we have performed, suggest the following picture for the germanium chalcogenide glasses. With x less than 0.33, the metastable amorphous structure is one in which chains are crosslinked by germanium atoms. The limit of such a structure is $x = 0.33$. In the composition range with x between 0.33 and 0.5, it is possible that the random covalent model applies to the vapor-deposited films and the as-quenched glasses. This supposition is strongly supported by the extremely good agreements obtained between areas calculated on the basis of the random covalent model and the areas obtained by X-ray diffraction and neutron diffraction radial distribution techniques. In the other range, however, it is likely that the metastable equilibrium system consists of phase separated GeTe-rich and GeTe_2 -rich mixture. The GeTe is probably threefold coordinated, but covalently bound.

Using this model as a working hypothesis, it is apparent that the previous compositions chosen for study were inappropriate for observing phase separation. As a result, we have prepared sputtered films of $\text{Ge}_x\text{Te}_{1-x}$ with $x =$ approximately 0.4. Transmission electron microscopy studies on these films are just beginning.

At the same time, it seemed appropriate to perform radial distribution studies on as-quenched and annealed samples of $\text{Ge}_x\text{Se}_{1-x}$ with $x = 0.4$ to determine whether the phase separation leads to a different short-range order as observed by the radial distribution studies. Samples for this study have been prepared, and X-ray diffraction measurements are underway.

III. Structural Studies in the Ge-S System

A. Bienenstock, S. Narasimhan and S.C. Rowland

The Ge-S system contains two glass-forming regions. One extends from S to GeS_2 , while the other is a small region centered around the 40 at % Ge composition. That is, the second is near the eutectic between GeS_2 and GeS. Earlier work indicated that the second glass forming region contained both covalently bonded GeS_2 tetrahedra and ionic GeS octahedra. Since this picture did not match that which had been found by us for the Ge-Te system, radial distribution studies were undertaken. The results are described in the manuscript of Appendix K, which has been submitted for publication.

IV. Impurity Effects in As_2Se_3

A. Bienenstock and K. Liang

As indicated in the original proposal, it was our intention to assess the possibility of using local mode spectroscopy to understand the role of Be and Mg impurities in the conductivity of As_2Se_3 . These impurities were chosen for study because of their small modification of As_2Se_3 's conductivity. This small modification is similar to that resulting from the admixture of Ca and is quite different from the large modification obtained by admixing Cu.

In the first annual report on this contract, we reported some results which changed the direction of research somewhat. In particular, we reported some results on samples which had sat in air at room temperature for 18 months. These samples were "pure" As_2Se_3 , as well as some to which

5% Be, Mg and Ca had been added. The "pure" sample showed two infrared absorption peaks at 635 and 780 cm^{-1} which have been associated with the presence of oxygen impurities. The samples to which the metals had been added did not show these absorptions. Hence, adding Group II metals to chalcogenide glasses became a potential method of eliminating undesirable effects of oxygen on infrared transmitting glassy chalcogenides. Because of the potential importance of this result for infrared window technology, emphasis has switched to an examination of this phenomenon. This report presents preliminary results associated with that examination.

Initial efforts were concentrated on construction of a high vacuum glass preparation system so that the oxidation of the samples could be reduced and so that large numbers of samples could be prepared. That construction is now completed and a number of samples have been prepared.

As indicated earlier, any improvements in resistance to oxidation degradation achieved by such metallic additions might be counterbalanced by compensating decreases in the quality of other properties. For this reason, a study of the glass transition temperature, T_g , and gross crystallization behavior was undertaken using the DTA (Differential Thermal Analysis) technique. Measurements on glasses to which 5% Be, Mg and Ca have been added indicate that T_g shifts downwards by no more than 10° C. This should not be of too great technological importance. Nevertheless, the downward shift is undesirable and raises the question of how low a concentration of Group II metals can be used to eliminate the oxygen absorption peaks. This is now being investigated.

In the annual report, it was indicated that the addition of 5% Mg appeared to increase the crystallization rate markedly. That is, DTA studies performed at a 20° C/min. heating rate showed the beginning of a crystallization exotherm at 310° C and an exotherm peak at approximately 325° C. A similar DTA study of the "pure" As_2Se_3 shows no such exotherm. This result was discouraging, for it indicated that the metallic additions might in general, increase the probability of crystallization of these materials.

Fortunately from the technological point of view and unfortunately from the scientific point of view, we have not been able to reproduce these results in the newer samples. That is, the samples with 5% additions of Be, Mg and Ca show no greater tendency to crystallize, as defined in the above-described DTA experiment, than does "pure" As_2Se_3 . We have searched unsuccessfully for an explanation of why the 18-month-old sample showed the crystallization exotherm while the new samples do not. One possible explanation was that the older samples had time to develop crystalline nuclei which grew at elevated temperatures. This possibility was partially eliminated, however, when it was found that when the older samples were heated to well above the melting temperature of As_2Se_3 and then quenched to reform the glass, they would crystallize rapidly on the next heating cycle of the DTA. Hence, if the nuclei were small crystals of As_2Se_3 , they would be eliminated in the melting process and could not act as nucleation centers in the next heating cycle. On the other hand, it is possible that the nuclei are small crystals of some compound with a higher melting temperature than that of As_2Se_3 , like MgSe. In this case, the nuclei would not be melted in the initial heating to above the melting temperature of As_2Se_3 .

Alternatively, it is possible that the older samples have other impurities of which we are unaware. These possibilities are now being investigated.

At the same time, we have been continuing our efforts to understand the role of the impurities on the electrical and optical properties of As_2Se_3 . Newly prepared samples with additions of Mg and Ca have been used for infrared absorption studies in the range of 300^{-1} cm to $16,600^{-1}$ cm. The most interesting feature of these results is the fact that no absorption peak which cannot be associated with pure As_2Se_3 is found in this range. Indeed, our measurements indicate that almost all the decrease in transmission in this range can be associated with reflection losses.

Finally, we should note that the near infrared absorption measurements indicate that the addition of 5% Mg or Be leads to no appreciable shift in the optical band gap. These results are consistent with the conductivity measurements which indicated no appreciable shift in the thermal gap.

Photoconductivity in Amorphous Chalcogenides

(Semi-Annual Report on 2-KUA-703).

Faculty: Richard H. Bube

Student: Thomas C. Arnoldussen

Theory

A model for photoconductivity in amorphous chalcogenide alloys has been developed which is able to account for all the known experimental variations with excitation intensity and temperature, and which provides the basis for determining intrinsic parameters of the localized state structure and the transport process. The results of this theoretical work and its application to known photoconductivity data are summarized in the manuscript, "Analysis of Photoconductivity in Amorphous Chalcogenides", included as an Appendix to this report.

Experiment

The objectives of our experimental work are to obtain measured values for the parameters involved in our proposed theoretical model for photoconductivity, and to expand and improve the model if needed. We are concerned primarily with the measurement of dark conductivity, photoconductivity, thermoelectric power and optical absorption as a function of temperature. We may also attempt, however, Hall, drift-mobility, photoluminescence, and AC conductivity measurements as feasible.

We have chosen the system $\left[\text{Ge} (\text{Se}_{1-y}\text{Te}_y)_2 \right]_x \left[\text{As}_2 (\text{Se}_{1-y}\text{Te}_y)_3 \right]_{1-x}$ for primary investigation, and furthermore have chosen the two endpoints of the composition range corresponding to $y = 2/3$, i.e., As_2SeTe_2 and $\text{Ge}_3\text{Se}_2\text{Te}_4$, for initial investigation in bulk and film form.

To date we have prepared bulk As_2SeTe_2 , as well as a powder-hot-pressed sputtering cathode of the same material for thin film sputtered films. The bulk material was prepared by sealing the appropriate amounts of As (6-nines pure, stored in vacuo), Se (5-nines pure, in shot form), and Te (5-nines pure, in chunk form), in an evacuated quartz ampoule and placing it in a rocking

furnace at 500°C for 48 hr (with two 1-hr periods at 650°C). The melt was removed from the 500°C furnace and immediately quenched in 300°K water. Part of this bulk material was loaded into a ball-mill jar under an inert nitrogen ambient dry-box. The jar was sealed by rubber O-rings and removed from the dry-box with a nitrogen atmosphere presumably trapped inside the jar. The material was then ball-milled for a total of 30 min with rest periods to keep the jar from heating. Returning the jar to the dry-box, the powdered material was hot-pressed in a stainless-steel die at 150°C and about 15,000 psi for 2 hr in the nitrogen atmosphere. The compacted disc was removed and polished and its density measured. The compacted density was found to be 97.6 percent of the theoretical average density of $(\text{As}_2\text{Se}_3)_{1/3}(\text{As}_2\text{Te}_3)_{2/3}$, which is a suitable degree of compaction for use as a sputtering cathode. Electron-microprobe analysis is being done to check the uniformity of this cathode as to composition, grain size etc.

A sample of pure As_2Se_3 is also being prepared, which will be subjected to the same preparation procedure as outlined above. This sample, when analyzed in bulk, pressed cathode and thin film form by microprobe and infrared transmission spectroscopy, will give us an indication of the concentration of oxygen impurity introduced during fabrication.

Publications and Presentations

- "A Model for Photoconductivity in Amorphous Chalcogenide Alloys," T.C.Arnoldussen, R.H.Bube, E. A. Fagen, and S. Holmberg, 4th International Conference on Amorphous and Liquid Semiconductors, Ann Arbor, August 1971
- "Analysis of Photoconductivity in Amorphous Chalcogenides," T.C.Arnoldussen, R.H.Bube, E. A. Fagen and S.Holmberg, submitted to J. Appl. Phys.
- "Analysis of Photoconductivity in Amorphous Chalcogenides," T.C.Arnoldussen and R.H.Bube, Am.Phys.Soc. Meeting in San Francisco, February 1972.

THE DENSITY OF STATES OF CRYSTALLINE AND AMORPHOUS Ge AND Si

W. E. SPICER

*Stanford Electronics Laboratories *, Stanford University, Stanford, Calif. 94305, USA*

and

T. M. DONOVAN

Michelson Laboratory, China Lake, Calif., USA

Received 17 August 1971

A qualitative distinction is made between: 1) Bragg band gaps due primarily to long range order and the Bragg reflection condition and 2) chemical gaps which reflect only chemical bonding. The density of states of amorphous and crystalline Ge are discussed.

In considering the density of states of crystalline and amorphous Ge and Si (as well as other materials), it may be useful to make a simple distinction between two types of band gaps: 1) chemical gaps which are primarily the result of the chemical character of the material, for example the covalent band in the present case, and 2) Bragg gaps which result from the Bragg reflection condition, and thus, long range order.

The first type of gap should depend principally on near neighbor interactions and thus persist in the amorphous material, whereas, the latter should only occur in the crystalline case. It is recognized that, in the crystalline material, it is impossible to say that a given gap is entirely chemical or Bragg in nature. However, since the Bragg reflection condition is removed in the amorphous case, only chemical gaps should remain in these materials.

In fig. 1, we present the optical density of states for amorphous Ge [1] obtained by photoemission and optical measurements. For the sake of comparison, the density of states of crystalline Ge obtained from band calculations [2] is also presented. There is a striking difference between these two curves. The crystalline density of states has strong conduction band peaks at about 2.1, 3.9, and 5.5 eV and valence band peaks at about -2.6 and -3.9 eV. None of this structure appears in the curve for the amorphous material. The situation is similar for Si [3]. From these results, we suggest that the five

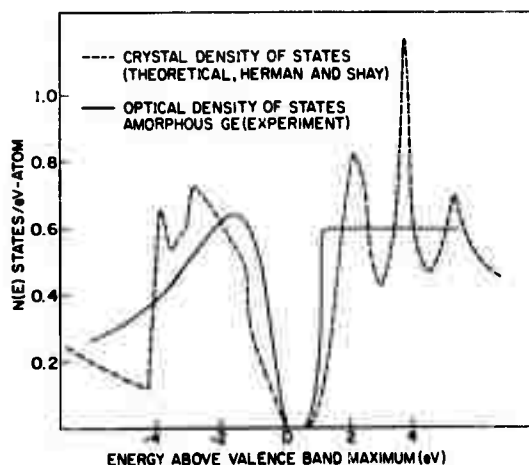


Fig. 1. A comparison of the density of states of crystalline Ge with the optical density of states of amorphous Ge.

strong peaks in the crystalline material are primarily the results of the Bragg reflection condition. As can be seen from an examination of the band structure the large peaks in the crystalline density of states are due principally to states near the zone face where the effects of Bragg reflection would be greatest.

One might argue that the density of states peaks are present in the amorphous material but that they are not detected because transitions from them are suppressed by weak matrix elements. This argument loses its strength if one remembers that: 1) if the matrix element is weak in one spectral range, and 2) the integrated

* Work at Stanford supported by ARPA through the Center for Materials Research and Army Office of Scientific Research, Durham.

transition probability for the valence is limited by the sum rule. In amorphous Ge, the sum rule is 85% exhausted [4] for $0 \leq h\nu \leq 11.8$ eV (11.8 is the upper limit of the photoemission measurement). Since the sum rule is almost exhausted within the range of measurement, it seems unlikely, that strong structure could exist and not have been detected in the photoemission and optical studies from which the optical density of states was derived.

Although the sharp peaks in the crystalline density of states do not appear in the amorphous material, there is still a band gap separating the conduction and valence bands. This is clearly a chemical gap due to the covalent bond. It appears that if care is taken to eliminate micro-voids and impurities, amorphous Ge and Si can be formed in which these band edges are quite sharp without appreciable tailing of states into the gap [5]. Drift mobilities greater than $1 \text{ cm}^2/\text{V-sec}$ have been measured in such material and the optical absorption and photoconductive thresholds coincide [6].

The retention of the sharp edges of the forbidden gap in the amorphous material is attributed to the fact that the covalent bond is retained almost undisturbed in the amorphous material. The sharpness of the gap in the amorphous material is probably a reflection of how well the covalent bond is defined; however, the gap energy is, of course, much less than the covalent bond energy. Note that the valence bond width is greater than the band gap.

With these thoughts in mind, one can reexamine the crystalline and amorphous density of states of fig. 1. In the amorphous material the principal constraint on the density of states is the covalent bond; thus, the density of states for the amorphous material can be thought of as the density of states imposed principally by the covalent bond. The single broad valence band max-

imum in the amorphous density of states coincides in energy with states along the bond direction in crystalline Ge.

For the crystalline material, a second major constraint is added, that of long range order; this produces Bragg reflection band structure and the reduced zone scheme. As a result of this added set of constraints, the sharp peaks shown in fig. 1 appear in the density of states of the crystalline material. Thus, it is suggested that the density of states of the amorphous material reflects principally the constraints set by the covalent bond; whereas, the density of states of the crystalline material results from the constraints set by long range crystalline order as well as the covalent bond.

Useful discussions with A. Bienenstock, J. Fischer, V. Heine, G. Lucovsky, D. Pierce, J. Stuke, D. Weaire and J. Tauc are gratefully acknowledged.

References

- [1] T. M. Donovan and W. E. Spicer, *Phys. Rev. Letters* 21 (1968) 1572;
W. E. Spicer and T. M. Donovan, *Journal Non-Crystalline Solids* 2 (1970) 66.
- [2] F. Herman, R. L. Kortum, C. D. Kuglin and J. L. Shay, in *Proc. Intern. Conf. on II-VI semiconducting compounds*, Providence, 1967 (W. A. Benjamin, Inc., New York, 1967), p. 271-289.
- [3] D. Pierce and W. E. Spicer, to be published.
- [4] T. M. Donovan, W. E. Spicer, J. M. Bennett and E. J. Ashlet, *Phys. Rev. B2* (1970) 397.
- [5] T. M. Donovan and W. E. Spicer, *Phys. Rev. Letters* 22 (1969) 1058;
K. L. Chapra and S. K. Bahl, *Phys. Rev.* 1 (1970) 2545;
T. M. Donovan, E. J. Ashley and W. E. Spicer, *Phys. Letters* 32A (1970) 85.
- [6] J. E. Fischer and T. M. Donovan, *Optics Communications* 3 (1971) 116 and to be published.

* * * * *

Photoemission Investigation of Amorphous Si and Ge*

D. T. Pierce, C. G. Albbing[†], and W. E. Spicer

Stanford Electronics Laboratories, Stanford University, Stanford, Calif. 94305

ABSTRACT: Photoelectron energy distribution curves (EDCs) from electron gun evaporated amorphous and annealed polycrystalline Si films are compared to the corresponding curves for Ge over a photon energy range from 6.5 to 11.7 eV. The EDCs of amorphous Si and Ge as well as the derived optical density of states show a sharp valence band edge but otherwise none of the characteristic peaked structures of the crystalline materials. In situ comparison to EDC's of Au accurately locates the Fermi level and monitor instrumental resolution allowing an upper limit of 3×10^{19} states/cm³-eV to be placed on the density of states in the energy gap of amorphous Si. EDCs typical of the crystal were obtained from Ge, which showed a rather abrupt amorphous to crystalline transition, by annealing to 300°C and from Si, which showed a more gradual transition, by annealing to 625°C. EDCs from amorphous and annealed Ge films reveal only minor dependence on evaporation rates of 2 and 26 Å/sec and on substrate temperature over the range -175° to 150°C.

*Work supported by ARPA through Army Office of Scientific Research, Durham and through the Center of Materials Research at Stanford University and by Army Office of Scientific Research.

[†]On leave from the Swedish Board for Technical Development.

In this paper we present a comparative study of amorphous Ge and Si based on recent photoemission measurements. Since in Ge and Si the complications of compositional disorder and phase separation are avoided, and the short range order is similar to that of the crystal, these systems are relatively simple and well suited to our search for an understanding of how the loss of long range order effects the electronic structure of the material.

We prepared amorphous films about 1000 Å thick by electron gun evaporation in the ultrahigh vacuum photoemission chamber where the source to substrate distance was 48 cm. The base pressure was 1×10^{-10} Torr or less, and during evaporation at a rate of 2 Å/sec it typically rose to 5×10^{-9} Torr. The detailed procedures for the separate Si¹ and Ge² experiments are reported elsewhere.

Photoelectron energy distribution curves (EDCs) from amorphous Ge and Si at several photon energies are compared in Fig 1. The curves are plotted with respect to initial state energy where the zero of energy is at the Fermi level. The characteristic feature of both sets of EDCs is the single broad peak. The Ge peak is narrower and located 1.25 eV below the valence band maximum while the broader Si peak is located 1.75 eV below the valence band maximum. The broad shoulder at about -6 eV, most apparent in Ge, may be due to inelastically scattered electrons.

As expected EDCs of amorphous Ge and Si show none of the variation due to the constraint of $\frac{1}{2}$ conservation which is found in the EDCs of Ge and Si crystals. There is also no evidence of any structure in the EDCs produced by structure in the final density of states to which the electrons are excited. Thus, since the transitions are nondirect, the

Reproduced from
best available copy.



EDCs reflect the valence band density of states, and we are justified in taking the high energy cutoff of the EDCs to represent the valence band maximum. The Fermi level was found to be 0.31 ± 0.05 and 0.28 ± 0.05 eV above the valence band maximum in amorphous Ge and Si respectively.

The optical density of states of amorphous Si calculated in terms of the nondirect transition model³ is compared in Fig. 2 to the optical density of states of amorphous Ge.⁴ As is expected from the EDCs in Fig. 1, the Si valence band has a peak that is broader and lower in energy than the Ge peak. The conduction band optical density of states illustrated in Fig. 2 must be taken as a rough model. The EDCs do not give any information about the density of states from the conduction band minimum to the vacuum level at 5.1 eV. The measured¹ variation of ϵ_2 suggests that there may be a peak near the conduction band edge and that the final density of states and/or the optical matrix elements decrease with energy. Because of the oscillator strength sum rule, the matrix elements must decrease for large $h\nu$.

The band densities of states of crystalline Ge and Si calculated by Herman et al.⁵ are shown as the dashed lines in Fig. 2. The striking difference between the crystalline and amorphous densities of states is that all of the sharp structure has disappeared in the amorphous case but the band gap and sharp band edges are retained.

Evidence for sharp band edges with no apparent tailing of the density of states into the energy gap of amorphous Ge has been previously reported by Sclar and Donovan.⁵ On the other hand, Potarson, Dinan, and Fischer⁶ (PDF) reported a rather large tailing of the density of states for amorphous

Si. Our photoemission investigation of amorphous Si, however, gives no evidence for such a large tailing of the density of states as previously reported.

In order to determine what part of the tail at the high energy edge of our Si EDC is real and what part is the result of experimental resolution, we compare our Si EDC in Fig. 3 to an EDC from Au where the true high energy edge is determined by the Fermi function. The insert of Fig. 3 shows a 5X vertical magnification of the Si and Au tail and of the Fermi tail which represents the Au EDC before it is affected by the imperfect experimental resolution. The measured Au tail extends well beyond the small Fermi tail calculated for the measurement temperature of 130°K. The similar shapes of the Si and Au tail suggest that the Si has no more tailing than the Au. The noise level determines the minimum difference which can be detected between the Si and Au tails and lets us put an upper limit on the number of states in the gap of 3×10^{18} states/cm³-eV. If the states were only in a 0.1 eV wide peak in the gap, for example, the number would be less than 3×10^{18} states/cm³.

In Fig. 3 we can also compare our EDC from amorphous Si to an EDC of PDF shown by the dotted curve. Their EDC is somewhat wider than ours indicating a lower threshold. Both the difference in the photoelectric threshold and the different position of the high energy edges are presumably caused by differences in sample preparation. PDF suggest that the cross-hatched area between -0.6 eV and the Fermi level is due to an exponential tail in the density of states. This cross hatched area is approximately 10X larger than the area corresponding to our upper bound of 3×10^{19}

Reproduced from
best available copy.



³ states/cm³-eV. The conclusion which we draw from this comparison is that while a tailing of the density of states may be caused by a given sample preparation, such a large tailing as previously reported is not an intrinsic property of amorphous Si. We believe that sample defects such as impurities or voids can produce an apparent tailing of the density of states. M. Brudak and T. E. Fischer⁷ report in this volume an observed tailing smaller than that of PDF which is also, in our opinion, possibly due to defects.

The annealing behavior of amorphous materials is an important parameter for determining the amount and nature of internal defects present in the re-deposited film.^{3,9} The effect of annealing is manifested in photoemission EDCs as seen in Fig. 4. The samples were successively annealed at each specified temperature typically for about 1/2 hr. In the case of Ge there is no apparent change with annealing up to 250°C, and then there is an abrupt change at 300°C and above to EDCs with crystalline structure. The EDCs from Si exhibit a gradual change at 400°C and show crystalline structure at 625°C. It is interesting to speculate whether this difference between the two materials indicates that the as-deposited Si has more defects sensitive to annealing, e.g. microvoids, than does Ge evaporated under similar circumstances. The EDCs from amorphous Ge and Si did not change when evaporated on substrates at room temperature or -170°C. In the case of Ge, further studies were made of film growth on a substrate at 150°C but no significant changes were observed. Evaporation of Ge onto a substrate at 260°C produced EDCs typical of the polycrystalline film. In the case of Ge, EDCs were also obtained from a film evaporated at a rate of 26 Å/sec instead of the usual 2 Å/sec. A hardly noticeable

broadening in the EDC resulted, but this we attribute to the increased evaporation pressure of 1×10^{-7} Torr.

In summary, our photoemission results have given a picture of the density of states of amorphous Ge and Si up to 5 eV below the top of the filled states. The loss of long range order causes a loss of the structure found in the crystal band density of states. However, as discussed in some detail for Si, no evidence of tailing of the density of states into the energy gap is observed. We suggest that sample imperfections such as impurities or microvoids can give rise to an apparent tailing of the density of states but that such effects should be distinguished from a tailing of the density of states produced by only the loss of long range order.

Reproduced from
best available copy.

Figure Captions

Fig. 1

EDCs at several photon energies from amorphous Ge and Si plotted with respect to initial state energy. The EDCs are well described by the nondirect transition model.

Fig. 2

The optical density of states (solid curves) of amorphous Ge and Si respectively compared to the corresponding band density of states of Ref. 3 (dashed curves). The lack of long range order in the amorphous case causes structure in the density of states to disappear but the short range order determined by the covalent bond is sufficient to produce the energy gap with sharp band edges.

Fig. 3

A measure of the tailing of the density of states of amorphous Si into the energy gap can be obtained by comparing a Si EDC to an Au EDC which has a known cutoff. The insert shows the high energy tails with a 5X magnification of the vertical scale; the dashed curve is the Si tail shifted 0.25 eV higher in energy to overlap the Au tail, and the broken curve is the true Fermi function cutoff of the Au. No extra tailing is apparent in the Si compared to the Au, but both are resolution broadened compared to the Fermi function cutoff. $V_2 = 0$ is the point of zero retarding voltage. The cross-hatched area shows the area attributed (Ref. 7) to an exponential tailing of the density of states. This area is about 10%

Fig. 4

larger than the area corresponding to the 3×10^{19} states/cm³ eV upper bound established in this work. Behavior of EDCs from Ge and Si at $h\nu = 8.6$ eV annealed at successively higher temperatures. Structure in the EDCs characteristic of the crystal is observed at 300°C in Ge and at 625°C in Si.

Reproduced from
best available copy.



References

1. D. T. Pierce and W. E. Spicer, to be published.
2. C. G. Ribbitt, D. T. Pierce and W. E. Spicer, *Physical Rev.*, to be published (1971).
3. C. W. Berglund and W. E. Spicer, *Phys. Rev.* 136, A 1030 (1964).
4. W. E. Spicer and T. M. Donovan, *J. Non-Cryst. Solids* 2, 88 (1970).
5. F. Horman and J. L. Shay, unpublished.
6. C. W. Peterson, J. H. Dinan, and T. E. Fischer, *Phys. Rev. Lett.* 25, 361 (1970).
7. M. Erbadak and T. E. Fischer, *J. Non-Cryst. Solids*, this volume.
8. H. L. Thiele, *Mat. Res. Bull.* 6, 103 (1971).
9. R. S. Baum and F. L. Gelsemer, *J. Non-Cryst. Solids*, this volume.

Fig. 1

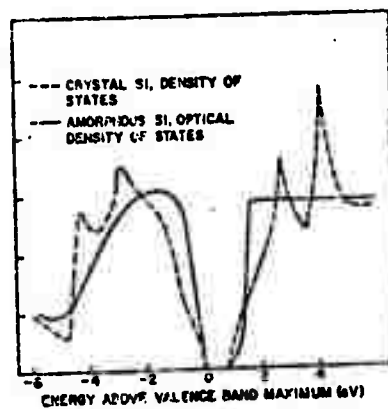
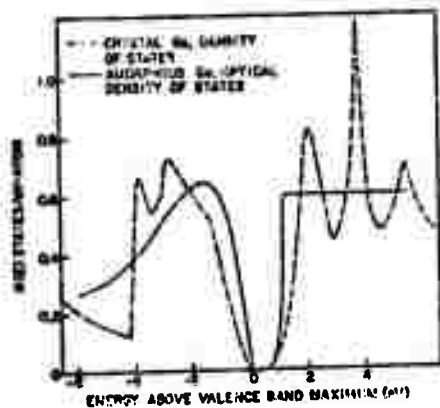
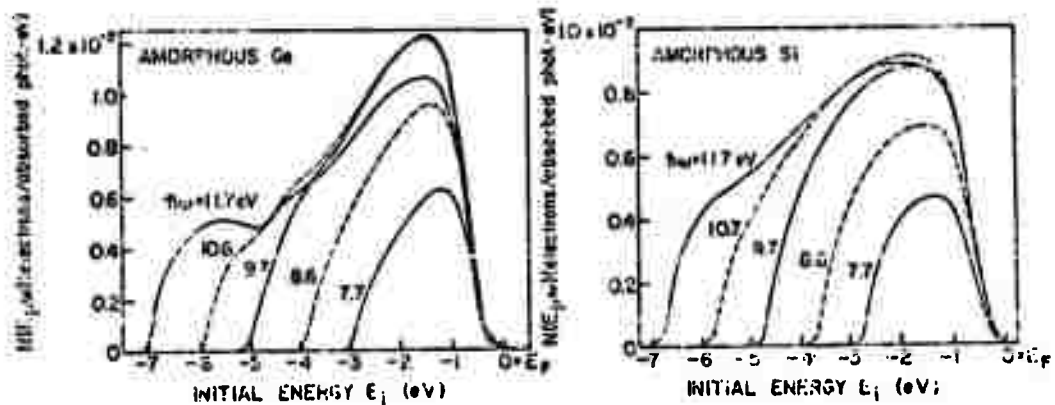
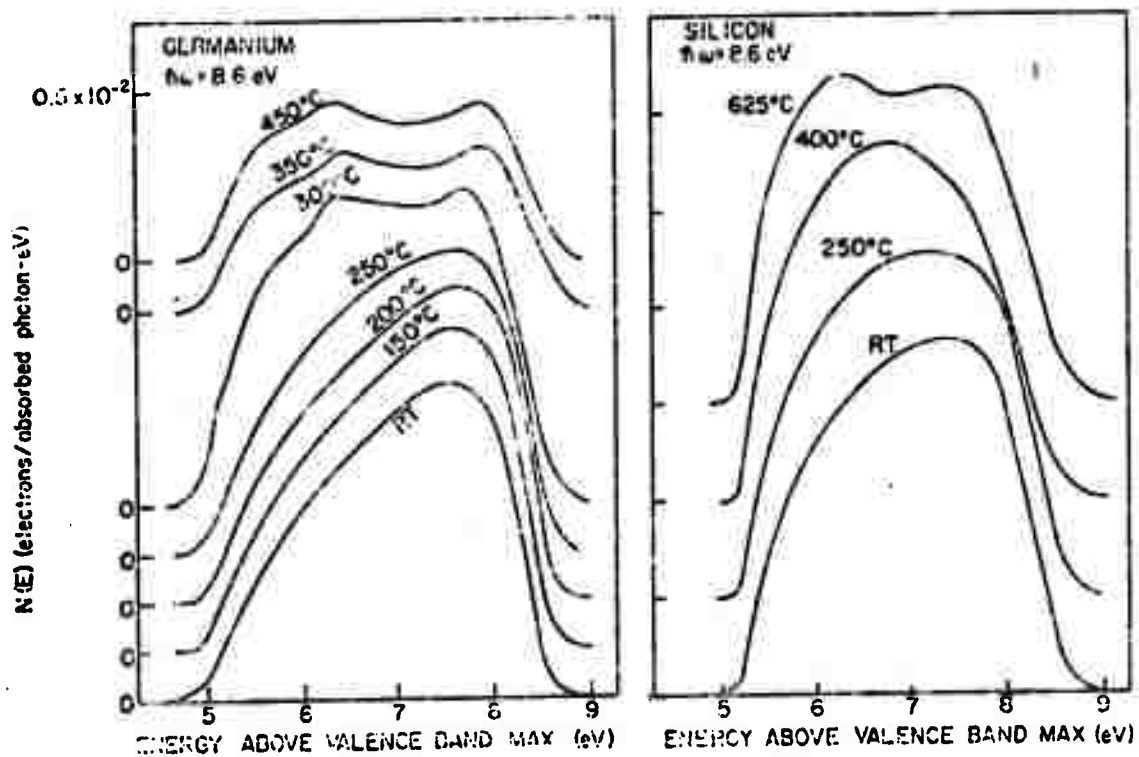
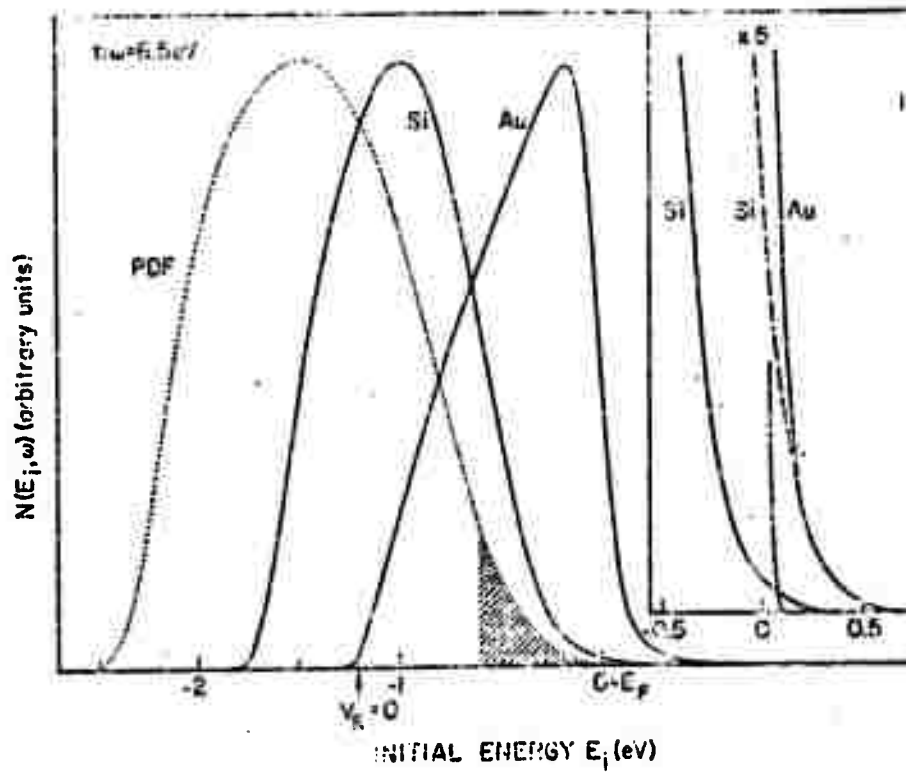


Fig. 2



INVESTIGATION OF THE BAND EDGES OF AMORPHOUS Ge AND Si

W. E. Spicer, Stanford University,
Stanford, Calif. and
T. M. Donovan and J. E. Fischer
Michelson Laboratory, China Lake, Calif.

In this paper, we are concerned with the occurrence of sharp band edges separating valence and conduction states in amorphous Ge and Si. By a sharp band edge we mean one in which the density of states drops at least a few orders of magnitude in a small energy range. This problem seems worth pursuing because it has long been assumed that the removal of long range order in a semiconductor would give rise to band edges which are much less sharp than those in the corresponding crystal.^{1,2}

Linear and exponential plots of two possible densities of states near the band edges are shown in Fig. 1. The density of states on the left of Fig. 1 is very close to that for a crystalline solid in that it drops several orders of magnitude at the band edges. For this case there is no difference between the mobility edges² and the band gap, i.e., the carriers in the conduction and valence bands are all in extended rather than localized states. Such densities of states might be expected for amorphous Ge and Si based on the calculations of Weaire, et al.³

In the right side of Fig. 1 is shown a more common model for the densities of states for amorphous semiconductors.^{4,5} This model differs in two significant ways from the "sharp edge" case discussed above. First, a mobility edge separating localized and extended states appears well up in the bands where the density of states is high. Second, there is a strong tailing of states into the band gap region, i.e., there is no sharp drop in the density of states at energies (E_v and E_c in Fig. 1)

where the character of the wavefunctions changes from extended to localized. To find which model is closest to "ideal" amorphous Ge and Si,⁴ we have carried out photoemission, optical, and photoconductivity measurements on amorphous Si and Ge.

Ge and Si were chosen for this study because: the bonding in both the parent crystal and in the amorphous phase is completely covalent, the amorphous structures have been studied in great detail,⁴ and the band structure of the crystals is well known.

The amorphous films studied at Stanford and the Michelson Laboratory were formed by evaporation under conditions found empirically to give sharp band edges. It appears that films prepared in this way^{5,6} may approach the "ideal" high density amorphous films predicted by the Polk model.⁴ The methods of preparing and characterizing these films have been described in detail previously.^{5,6,7} Suffice it here to mention what seem to be the conditions essential to obtaining a sharp edge in an as evaporated film:

- 1) reasonably good vacuum ($p < 5 \times 10^{-6}$ torr) during evaporation,
 - 2) slow evaporation rates (order $2-50 \text{ \AA}^2/\text{sec}$) and
 - 3) large evaporation to substrate distances (about 40 cm).
- Optical absorption measurements for Ge⁵ and Si⁸ are shown in Fig. 2.

The most important characteristic of these curves, for the purposes of this discussion, is the sharp drop in absorption starting at an absorption coefficient of about $10^3/\text{cm}$. We associate this with a sharp edge in the density of states. For Ge evaporated on a 300°C substrate, we measured a film density within 2% of the bulk density and the absorption edge is close to 0.7 eV.⁵ For a second Ge film formed under the same conditions

We believe this is due to sample preparation. Erbudak and Fischer used a very short (a few inches) evaporator to substrate distance in contrast to the large distance used by ourselves. Other preparation conditions were similar. The gap states observed by Erbudak and Fischer tended to anneal out indicating they are not intrinsic to the amorphous phase. It now appears clear that films with quite different properties can be produced depending on evaporation conditions.

Optical absorption data for amorphous Si is also shown in Fig. 2.

As in the case of Ge the edge is sharper than the corresponding indirect edge in the crystalline material. In comparison with our data on amorphous Si we show an absorption curve due to Brodsky, et al.¹⁵ for an unannealed sputtered film. These authors plotted their data as $\alpha^{1/2}$ vs $h\nu$ and defined a parameter E_g as the point at which the straight line portion of such a curve extrapolates to zero. This value is shown in Fig. 2. It seems unlikely that E_g corresponds to a fundamental band gap for several reasons: (1) E_g lies at a large value of α (about $10^4/\text{cm}$) and is 0.4 eV above the sharp drop in α . (2) There is no true α near E_g suggesting a band edge and (3) finally there is no real theoretical justification for the use of the $\alpha^{1/2}$ plot to obtain the band edge in a amorphous materials. If a true absorption edge did exist at E_g and the strong absorption below E_g was due to localized gap states, these would tend to anneal out leaving the fundamental edge unchanged. Such a situation should be readily detected using photoemission; however, it was not seen in the work of Pierce, et al.¹³ Therefore, at least for the films formed at Stanford and the Michelson Laboratory, it appears reasonable to associate the sharp absorption edge near 0.7 eV with the onset of intrinsic absorption.

4

on a room temperature substrate the density is about 10% less than crystalline and the absorption threshold is at lower energy but the sharp absorption edge remains.^{5,7} Sharp absorption edges for amorphous Ge have also been reported by Chopra and Bahi⁹ and more recently by Théye.¹⁰ It is interesting to note that when Théye duplicated our relatively slow evaporation rate (2A"/sec) a sharp absorption edge at $h\nu \lesssim 0.7$ eV similar to ours was obtained for all substrate temperatures from 25°C to 350°C. If, on the other hand, a fast evaporation rate (200 A"/sec) was used a broad, exponential type edge was obtained for films grown at room temperature. On annealing this sharpened and moved to photon energies above 1eV. Results similar to the last mentioned have been reported recently by Paul and coworkers for both Ge and Si prepared in several ways.¹¹ All of these results emphasize the importance of sample preparation, particularly if a sharp absorption edge is to be obtained on an as-grown film.

Whereas optical or photoconductivity measurements depend only on the energy differences between initial and final states, photoemission measurements can give information on the absolute energy of the initial and final states. Such information is very useful in determining if band tailing is present and whether an optical absorption edge is due to transitions from states in the gap or to valence band states. From photoemission investigation of our as-grown and annealed films of Ge^{6,7,12} and Si,¹³ no evidence for tailing states or states in the gap have been found. From this work the Fermi level at the surface was located at 0.31 eV and 0.28 eV above the top of the valence band for Ge and Si, respectively.

Quite different results both in the position of the Fermi energy and the existence of tailing states have been obtained by Erbudak and Fischer.¹⁴

3

From our photoconductivity measurements on Ge and Si, very good correspondence between the sharp optical absorption edge and the threshold for photoconductivity is obtained.⁸ Preliminary interpretation of this data suggests that the photocarriers drift in extended states and give no evidence for the existence of a mobility edge different from the density of states edge.

Conductivity versus temperature measurements have been made for some of our amorphous films.¹⁶ For a fully annealed (high density) Ge film, the data is well fit by a single exponential with an activation energy of 0.4 eV over the temperature range 90 to 350°K. If we accept the suggestion by Pritzsche¹⁷ that this gives the Fermi level to conduction band (extended states) energy, this sets the Fermi level 0.4 eV below the conduction band. If we assume that the bands are flat, the surface Fermi level as measured in photoemission will be identical with that in the bulk. This is probably a reasonable assumption because of the high resistivity and thinness of the samples and because any remaining dangling bonds in the interior may have energy levels similar to those on the surface. The photoemission experiments give a valence band to Fermi level energy 0.31 eV. A thermal gap of 0.71 eV is given by this value plus the Fermi level to conduction band energy of 0.4 eV. Considering the experimental uncertainties, this agrees well with the optical band gap value of 0.7 eV obtained from the sharp optical absorption edge (see Fig. 2) for high density samples.

For our films, the photoemission gives no evidence for states in the band gap region despite the fact that the Fermi level at the surface was about 0.3 eV above the top of the valence band. This makes it difficult

to believe that the sharp absorption edges shown in Fig. 2 are due to excitation from states in the gap. If one assumes, for example that the band gaps of 1.0 and 1.4 eV obtained by Paul and coworkers⁸ for their amorphous Ge and Si respectively applies to our films, then one would have to assign absorption coefficients up to $10^4/\text{cm}$ to defect levels in the amorphous material; such high levels extending about 0.5 eV into the gap would certainly have been detected in the photoemission and conductivity experiments.

It might be suggested that states were present in the gap but that matrix elements prevented optical transitions from them into the extended states. To evaluate this suggestion, one should look at the optical absorption in crystalline Ge and Si. Here one finds that, in general, there are strong matrix elements coupling deep states in the gap with extended states. The situation should be similar for amorphous Ge and Si. Only if the localization is small compared to lattice dimensions as in the case of f like atomic states or if the center has a net charge greater than unity¹⁸ should matrix element suppression be important. Neither situation should arise in amorphous Ge and Si because of the lack of long-range order; or because of a slight distortion of band angles and lengths locally. Of course, since the matrix element suppression arguments apply to transitions to final states near the band edges, they would not apply to the photoemission experiments where the final states are many eV above the bottom of the conduction band.

From the results discussed above, it appears that there are sharp edges in the density of states of our samples of amorphous Ge or Si and that density of states diagram such as that on the left hand side of

Fig. 1 are appropriate to amorphous Ge and Si. This does not mean that there are no states in the gap, but rather that the density of states drops sharply over, at least, several orders of magnitude at the band edges. More work must be done before it is established definitively that the mobility rises abruptly at the band edge as shown on the left of Fig. 1; however, the presently available data seems to support this model rather than a model such as that on the right of Fig. 1.

ACKNOWLEDGMENT

Fruitful discussions with J. Dow, N. Mott, D. Pierce, and C. Rihling are gratefully acknowledged.

Work supported by the Advanced Research Projects Agency through the Army Office of Scientific Research, Durham, and through the Center for Materials Science at Stanford University.

1. See the discussion in M. Cohen's recent article (Ref. 2)
2. Morral Cohen, *Phys. Today* **24**, 26 (1971).
3. D. Wesire, *Phys. Rev. Lett.*, **26**, 1541 (1971); D. Wesire, M. Thorpe, and V. Heine, paper 1313-3 of these Proceedings.
4. D. Turnbull and D. S. Polk, Paper AA2 of these Proceedings.
5. T. M. Donovan, E. J. Ashley, and W. E. Spicer, *Phys. Lett.* **32A**, 85 (1970).
6. T. M. Donovan, Ph.D. Thesis, Stanford University, 1970.
7. T. M. Donovan and W. E. Spicer, *Phys. Rev. Letters*, **22**, 1056 (1969); T. M. Donovan, W. E. Spicer, J. M. Bennett and E. J. Ashley, *Phys. Rev.* **B2**, 397 (1970); W. E. Spicer and T. M. Donovan, *Jour. Res. Cryst. Solids*, **2**, 66 (1970).
8. J. E. Fischer and T. M. Donovan, Paper CA5 of these Proceedings. *Optics Comm.* **3**, 116 (1971).
9. K. L. Chopra and S. K. Bahl, *Phys. Rev. B*, **1**, 2545 (1970).
10. M.-L. Théys, *Optics Comm.* **2**, 329 (1970); *Mat. Res. Bull.* **6**, 103 (1971).
11. G. A. N. Connell and W. Paul, Paper CA-7, these Proceedings; D. O. Camphausen, G. A. N. Connell, and W. Paul, Paper CA-6 these Proceedings.
12. C. G. Rihling and W. E. Spicer, *Phys. Rev.*, in Press.

Figure Captions

13. D. T. Pierce and W. E. Spicer, in press. D. T. Pierce, C. G. Ribbing, and W. E. Spicer, Paper JB-6, these Proceedings.
14. M. Erbudak and T. E. Fischer, Paper JB-7, these Proceedings.
15. M. E. Brodsky, R. S. Title, K. Weiser, and G. D. Pettit, Phys. Rev. B 1, 2632 (1970).
16. M. L. Knotek, to be published.
17. H. Fritzsche, J. Non. Cryst. Solids, 6, 49 (1971)
18. J. D. Dow and J. J. Hopfield, Paper GA9 of these Proceedings.

Fig. 1

Si near the band edges.

Fig. 2

Two models for the electron structure of amorphous Ge and Si near the band edges.

Optical Absorption near the band edge for various samples of Ge and Si. T_s is the temperature of the substrate on which the Ge is evaporated. For $T_s = 300^\circ\text{C}$ the sample density was within 2% of the crystalline density. For $T_s = 25^\circ\text{C}$, the density is about 10% less than the crystalline. It is suggested that the edge shift is due to strain produced by micro-voids in the low density sample. For Si, the dashed curve is an unannealed sputtered film (Ref. 15). The solid curve is for an evaporated film (Ref. 8).

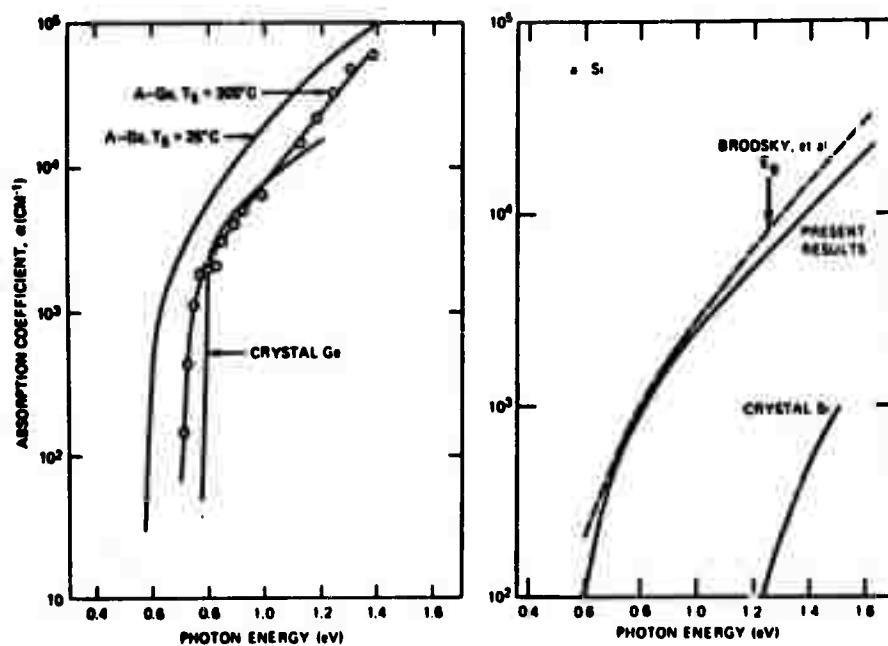
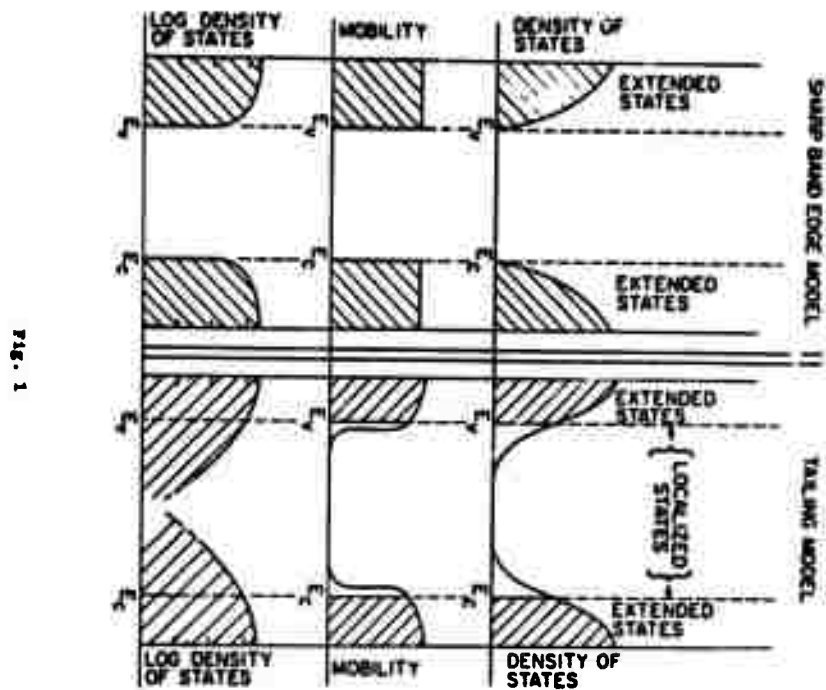


Fig. 2

IMPURITY ELECTRONS IN AMORPHOUS GERMANIUM A PHOTOEMISSION ARGUMENT FOR THE MOTT MODEL *

C. G. RIBBING** and W. E. SPICER

Stanford Electronics Laboratories, Stanford, California 94305, USA

Received 4 September 1971

Photoemission-measurements of amorphous and crystallized Ge alloyed with As are reported. The results show that while the effect of alloying on the electronic structure is strong in the crystalline case, it is relatively small for the amorphous material.

The addition of some impurity atoms (typical exceptions: Ag and Cu) to some semiconducting chalcogenide glasses has little effect upon the electric conductivity as shown in early works by Kolomiets and Nazarova [1]. To explain this absence of doping effects, Gubanov [2] suggested that the impurity electrons remained in the amorphous pseudogap occupying deep localized states that did not contribute to the conductivity. The only effect of doping would be to raise the Fermi level of the material. An alternative hypothesis was put forward by Mott [3]. Focussing on the structural flexibility of an amorphous solid, he assumed that all five valence electrons of e.g., a phosphor atom in amorphous germanium could be covalently bonded by a local change in coordination.

The present work is an attempt to prove experimentally which of the two theories is valid for the case of amorphous Ge doped with As. The experimental method used was UV photoemission and the conclusions rely heavily on comparisons with an earlier experiment on undoped Ge [4]. The equipment used was the same as detailed in ref. [4] and the procedures were virtually identical.

The source material was prepared from Eagle Picher Intrinsic grade polycrystalline Ge and 1% Electronic Space Products, Inc. (ESPI's) 5N As, which was melted in an evacuated quartz ampoule.

As was to be expected from the equilibrium phase-diagram for the Ge-As system [5], the result was a phase-separated mixture of Ge and GeAs. This source material was etched to remove surface oxides, placed in the ultra high vacuum chamber which was pumped down to roughing pressure within a few hours after the etching. After baking and final pump down, the source material was pre-melted for 30 sec in the e-gun crucible, with the main shutter closed. Thereby the pressure rose to $\sim 10^{-6}$ torr. The Ge single crystal substrate was heat cleaned at more than 450°C for about 25 minutes. After the usual deposition of a fresh gold layer on the collector, the sample film was e-gun evaporated at a source-to-substrate distance of 48 cm. The rate readings on the quartz crystal monitor were 1-4 Å/sec. During evaporation, the pressure rose to 3×10^{-7} torr from the base pressure of 2.5×10^{-10} torr. After the experiment the sample thickness was measured on a Varian Å scope giving 640 ± 50 Å and an average deposition rate of 2.3 Å/sec.

Judging from the vapor-pressures, there were reasons to believe that Ge and As might evaporate at different rates. Therefore the crystallized sample film, an amorphous test film and the remaining source-material were carefully micro-probed. The L lines of Ge and As were used to obtain a good analysis of the relatively thin film. An As content of $4.5 \pm 0.5\%$ was found in the films with no detectable phase separation and no apparent concentration gradient over the thickness of the film. The possibility of phase separation on a microscopic scale can however, not be ruled out since the resolution of the microprobe was only $\sim 1\mu$. The As content in the source material was $0.013 \pm 0.0003\%$ showing that the As indeed

* This work was supported by the Advanced Research Projects Agency through the Army Office of Scientific Research and through the Center for Materials Science at Stanford University.

** On a grant from the Swedish Board for Technical Development. Present address: Institute of Physics, Box 530, S-75121 Uppsala, Sweden.

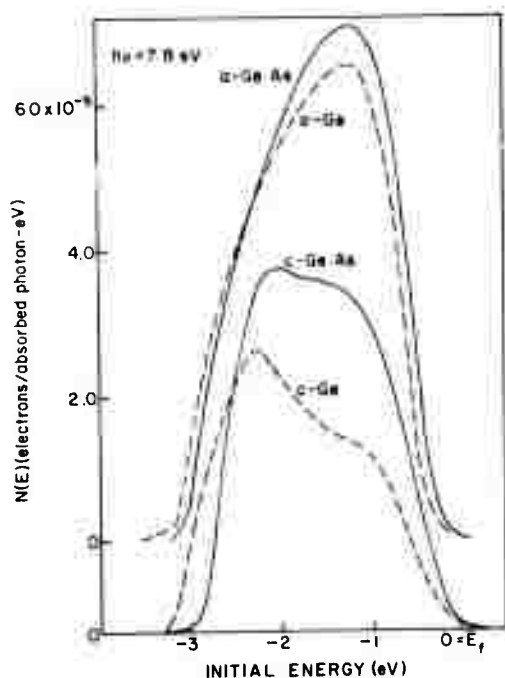


Fig. 1. Normalized EDCs for amorphous and polycrystalline Ge in undoped (dashed lines) and alloyed case (full lines).

had evaporated preferentially. This implies that even the few outermost atomic layers must have had a dopant content $5 \cdot 10^{18} \text{ cm}^{-3}$, while the upper limit is still 4.5%. Fig. 1 gives a comparison of normalized energy distribution curves (EDCs) for the doped case Ge-As in this experiment (full lines) and the case of undoped Ge reported earlier (dashed curve) [4]. The top curves are for the as deposited amorphous films and the bottom ones for the polycrystalline films obtained after annealing in situ for 30 minutes at 450°C. It is worth noting that annealing to only 300°C did not produce any crystalline structure in the EDCs as observed in the undoped case. This is in agreement with the observation that the presence of impurities tends to stabilize the amorphous state [6,7].

Before examining the experimental data in detail we recall that if Gubanov's model was applicable to this case we would expect to see emission from states in the forbidden gap, since a large number of impurity electrons would be present in these localized states. Furthermore the occupancy of these states would shift the Fermi level upwards. If Mott's model was applicable we would not expect any extra emission

from gap states, no change in Fermi level but possible a small shift in the valence band.

Now looking at fig. 1 the curves clearly show how much more the electronic structure of the crystalline material is affected by the impurity than is that of the amorphous. The difference in workfunction can only be responsible for a part of the discrepancy in the crystalline case. The similarity of the two amorphous curves is striking considering that they were recorded in two different experiments and originate from films deposited at different pressures. The difference in peak heights stems from the normalization to the photoelectric yield which was about 10% different for the two cases. All four curves have been lined up by their Fermi level for comparison. The fact that the positions of the peaks in the amorphous cases agree, therefore indicates that the Fermi level has not shifted more than the experimental uncertainty $\approx 50 \text{ meV}$, upon alloying. Our experimental results, thus seem to favor Mott's model of flexible coordination rather than the gradual occupation of localized gap states. It appears, however, as if the valence band edge has shifted upwards. From several curves in the 6.2 - 7.8 eV range, the interval from Fermi level to valence band maximum (VBM) were determined, using the deconvolution method of ref. [4], to be $0.21 \pm 0.03 \text{ eV}$ apart. This should be compared to $0.31 \pm 0.05 \text{ eV}$ for the case of pure amorphous Ge.

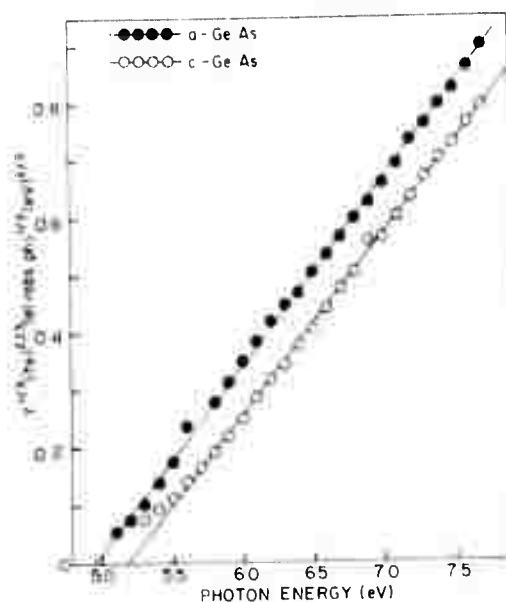


Fig. 2. Ballantyne plot of the photoelectric yield for alloyed Ge in the amorphous and polycrystalline case.

This barely significant shift is remarkably small considering the large amount of As present in the sample.

The E_f - VBM difference for the α - Ge: As case of 0.21 eV added to the work function of the sample 4.73 ± 0.04 as obtained from the EDCs, gives a threshold of 4.94 eV. This agrees well with the threshold 4.95 eV obtained from yield-measurements by extrapolation of the $Y^{1/3}(\hbar\nu)^{2/3}$ versus $\hbar\nu$ -relation plotted in fig. 2, which was recently derived by Ballantyne [8]. Fig. 2 also shows the curve for the yield of the crystallized film. We interpret the tailing off from the linear relation at photon energies close the threshold as yet another indication of the presence of impurity electrons. A similar tail in fig. 8 of ref. [4] most likely originates in stray electrons from the ion pump, since in that case the photoelectric yield was measured by collector-current. In this experiment, however, that small systematic error was eliminated by monitoring emitter-current.

In conclusion, we find that this experiment gives dramatic verification of the ability of amorphous Ge to accommodate impurity electrons, without gross effects on the electronic structure.

Our results furthermore appear to favor Mott's explanation that this is due to the ability of amorphous materials to allow local rearrangements of the coordination, in marked contrast to the corresponding crystalline material.

The authors gratefully acknowledge Yves Verhelle for preparing the source material and Chuck Taylor for extensive microprobe analysis.

References

- [1] R. T. Kolowitz and T. F. Nazarov, *Fiz. Tverd. Tela* 1, (1959) 22; 2 (1959) 174, *Transl. Soviet Phys. Solid St.* 2 (1959) 195.
- [2] A. I. Gubanov, *Quantum electron theory of amorphous conductors* (Consultants Bureau, New York 1965).
- [3] N. F. Mott, *Phil. Mag.* 19 (1968) 835 particularly fig. 6, p. 849.
- [4] C. G. Ribbing, D. T. Pierce and W. Spicer, *Phys. Rev.*, to be published.
- [5] Hansen, *Constitution of binary alloys*, Suppl. 2, (McGraw-Hill, 1958), p. 53.
- [6] R. F. Adamsky, *J. Appl. Phys.* 40 (1969) 4301.
- [7] A. S. Nowick, *Comments on solid state physics* V2 (1970) 155.
- [8] J. M. Ballantyne, to be published.

.....

APPENDIX E

UV DIELECTRIC CONSTANTS OF a-Ge AS A FUNCTION OF FILM DENSITY

by

R. S. Bauer and P. L. Galeener
Xerox Palo Alto Research Center
Palo Alto, California 94305

and

W. E. Spicer*
Stanford University
Stanford, California 94305

ABSTRACT

The reflectance of a-Ge has been measured in situ on thin films deposited at various substrate temperatures T_s . Kramers-Kronig analysis of this data yields the uv dielectric constants as a function of film density. Trends in the dielectric constants are consistent with the presence of submicroscopic voids whose volume fraction decreases as T_s increases. These voids are partially aligned and will therefore lead to anisotropy in several physical properties.

(To be Published in Proceedings of Fourth International Conference on Liquid and Amorphous Semiconductors, Ann Arbor, Mich.)

UV Dielectric Constants of a-Ge as a Function of Film Density

R. S. Bauer and P. L. Galeener

Xerox Palo Alto Research Center
Palo Alto, California 94305

and

W. E. Spicer*
Stanford University
Stanford, California 94305

Introduction

Submicroscopic voids have been discussed as possible elements in the structure of amorphous Ge and Si.¹ Recently, Galeener has shown that the presence of voids in an absorbing medium has two primary effects on the imaginary part of the dielectric constant:² (1) the reduction in strength (without change in position) of the principal absorption peak characteristic of the host material; (2) the introduction of a new void resonance (at higher photon energy) whose strength and position are governed by the volume fraction and shape of the voids. In this paper, we report an experimental investigation of the effect of variations in void concentration on the optical properties of evaporated a-Ge.

Experimental Variation of Void Density

The volume fraction of voids was experimentally controlled by depositing the Ge onto substrates of various temperatures. The work of Donovan, Ashley and Spicer has shown that the density of a-Ge films increases by nearly 15% (in the crystalline value) upon increasing the substrate temperature during deposition, T_s , from room temperature to just below the crystallization point.³ In addition, the nearest neighbor distance for room temperature deposited a-Ge is found by x-ray diffraction to be the same as the crystalline value.⁴ Combining these two observations, we conclude that the density of voids in as-deposited a-Ge is reduced as one increases the substrate deposition temperature.

The room temperature, near-normal incidence reflectance, R , was measured⁵ from 2.2 through 11.4 eV in 1000 Å thick films, a-Ge deposited at 2 to 4 K/cm at pressures of 1 to 3×10^{-8} torr during evaporation. This slow deposition rate was chosen to minimize the void concentration at each T_s , maintaining by the source, which was 40 cm from the substrate, was found to be less than 5°C as measured by a thermocouple attached to the substrate. The surface roughness

DSBA and Jungk were seeing effects due to the presence of voids in their samples.

The tentative explanations discussed by these authors included changes in the density of states of a-Ge with deposition temperature and surface roughness effects. The work of Magerle, Pierce, and Spicer¹¹ shows that the optical densities of states, measured by photoemission, do not change when a-Ge films are prepared under the same conditions which yielded the reflectance changes we observe (see Fig. 1). Therefore, the large effects we observe in the dielectric constant cannot be accounted for by changes in the density of states. Since we have shown that the high energy structure noted by DSBA is dramatically reduced by increasing T_s , it is clear that this structure is not a reflection of the substrate surface roughness. The observed bands in optical properties with T_s are consistent with both enclosed voids and voids that intersect the surface. Since the latter contribute to surface roughness, some fraction of the observed effects may be viewed as due to void-induced surface irregularities.

Our reflectance values for $T_s = 22^\circ\text{C}$ result in optical constants slightly different from those reported by DSBA. As seen in Fig. 4, the high energy structure of our data is weaker than that reported by DSBA, while the main peak is stronger. Both observations are consistent with the assumption that our $T_s = 22^\circ\text{C}$ sample contains somewhat fewer voids than the DSBA sample. In support of this conclusion, we note that the differences in sample preparation between the two studies¹² should result in higher void density in the DSBA film: viz., higher evaporation rate, higher deposition pressure, and shorter source-to-substrate distance.

As will be described elsewhere,¹³ the void theory can be applied to experimental data in order to extract the effect of the voids. This is done to obtain a theoretical estimate for the dielectric constant of void-free e-Ge and to deduce the characteristics of the voids themselves. The result for our room temperature deposition data is presented in Fig. 5. There is only a very restricted range of values for the volume-fraction of voids f_v (5%) and the depolarization factor L (≈ 0.8) which remove the high energy resonance. The large depolarization factor indicates that the voids are disc-shaped and have normals randomly distributed within the plane of the film. Because of this anisotropic arrangement of non-spherical voids, several physical properties should prove to be different when measured parallel and transverse to the plane of the film. Included are optical and electrical properties, as well as the low-angle x-ray and electron diffraction intensities expected from voids.

of all samples was minimized by using float glass substrates. In Fig. 1 the results for a-Ge films deposited at three substrate temperatures are shown. Below 2.2 eV the data is extrapolated to the low energy reflectance of evaporated a-Ge found by Donovan, Spicer, Bennett, and Ashley (DSNA)⁷ since the reflectance has been measured to be independent of T_s at low photon energies.⁸ From 22°C to 160°C , the peak in R increases by about 10% in absolute value and shifts position by almost 2 eV; these changes are quite large and reproducible.

The corresponding dielectric constants were obtained from a Kramers-Kronig analysis of the reflectance data. The experimental curves were extrapolated to higher energies using a scaling of the Norton and Toots data⁹ from 11.8 through 24.8 eV; this was continued with a power law tail whose free parameter was adjusted to make the reflectance phase zero at photon energies below the gap (0-0.4 eV). The use of scaled data⁹ in this extrapolation was found not to influence the conclusions drawn below. The resultant values for the imaginary part of the dielectric constant, ϵ_2 , are shown in Fig. 2 for the data of Fig. 1. The changes in ϵ_2 are precisely those predicted for the effect of voids.¹⁴ Firstly, the peak in ϵ_2 occurs at 2.8 eV within 0.1 eV for all three samples. Further, its strength increases (by 17%) as the density is experimentally decreased (i.e., as T_s increases). Simultaneously, the high energy resonance is decreased. This latter effect is seen more clearly in the optical transition strength, $\omega^2\epsilon_2$, shown in Fig. 3. The changes at high photon energies are seen to be quite significant. The broad void resonance hump at about 11 eV decreases in strength as void concentration is reduced (i.e., as T_s is increased). There are then two experimental changes occurring simultaneously as the substrate growth temperature is raised. Both of these are consistent with the theory for the effect of voids on optical properties.

Discussion and Conclusions

Portions of these changes have been observed in previous work. DSBA noted a shoulder in $\omega^2\epsilon_2$ at around 9 eV for room temperature deposited films.⁷ Jungk observed a 25% increase in the strength of his 2.6 eV ϵ_2 peak by increasing T_s from 20°C to 200°C .¹⁰ In neither case were the effects ascribed to the presence of voids. From our work, we find experimentally that the high energy structure decreases enormously as the film density is increased (Fig. 3). Further, we see experimentally for the first time that the increased strength of the main resonance (with increasing T_s) is correlated with this decrease in high energy absorption (Fig. 2). These observations, taken together, allow us to conclude that both

Acknowledgement

The authors are grateful to Dr. G. Lucovsky for helpful suggestions regarding application of our Kramers-Kronig analysis.

References

1. Standard work supported by AFPA through the Center for Materials at Stanford University.
See for Example:
M.H. Bradsky and M.E. Tittle, Phys. Rev. Letters 22, 381 (1963);
S.C. Moss and J.P. Czornyj, Phys. Rev. Letters 22, 1187 (1969);
M. Ehrenreich and D. Turek, Comments on Solid State Physics 3, 75 (1970).
2. F.L. Galeener, Bull. Am. Phys. Soc. 16, 302 (1971).
3. F.L. Galeener, Phys. Rev. Letters 27, 421 (1971).
4. T.M. Donovan, E.J. Ashley, and W.E. Spicer, Phys. Rev. Letters 32A, 85 (1970).
5. N.J. Shevchik and W. Paul, These Proceedings (Paper DB 5) and Cited References.
6. The Reflectometer Developed by Endriz was used. See J.G. Endriz, Ph.D. Thesis, Stanford University, 1970 (Unpublished).
7. See for Example: H. Reiss, J. Appl. Phys., 39, 5045 (1968).
8. T.M. Donovan, W.E. Spicer, J.M. Bennett, and E.J. Ashley, Phys. Rev. D2, 397 (1970).
9. T.M. Donovan, Thesis p. 118, Fig. V-2, Stanford University, 1970 (Unpublished).
10. L. Marton and J. Toots, Phys. Rev. 160, 602 (1967).
11. G. Jungk, Phys. Stat. Sol. (b) 44, 239 (1971).
12. C.G. Ribbing, D.T. Pierce, W.E. Spicer, Phys. Rev. B, to be published.
13. T.M. Donovan, private communication.
14. F.L. Galeener, to be published.

Figure Captions

- Fig. 1** The spectral dependence of the reflectance of a-Ce films deposited on substrates held at temperatures, T_g , from 22°C through 160°C and measured in air at room temperature.
- Fig. 2** The room temperature spectral dependence of ϵ_2 for a-Ce deposited on substrates at temperatures, T_g , from 22°C through 160°C.
- Fig. 3** The room temperature spectral dependence of the optical transition strength for a-Ce deposited on substrates at temperatures, T_g , from 22°C through 160°C.
- Fig. 4** Comparison of the room temperature spectral dependence of the optical transition strength of a-Ce deposited at 22°C determined in this work with that of Donovan, Spicer, Bennett, and Ashley (Ref. 7).
- Fig. 5** Theoretical estimate of the optical transition strength for void-free a-Ce, obtained from the $T_g = 22^\circ\text{C}$ results of Fig. 3 by extracting the effect of a 5% volume fraction of voids, δ , having depolarization factor $L = 0.8$.

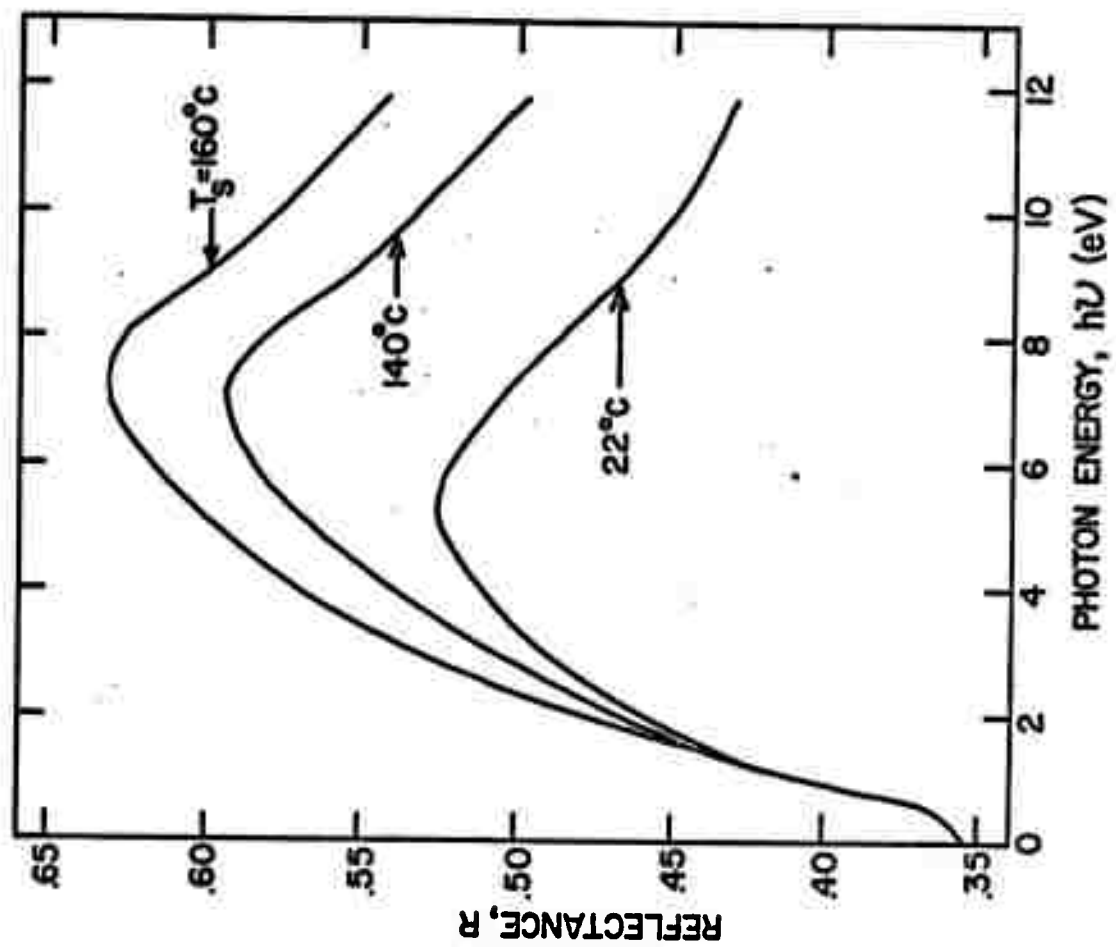


Fig.2

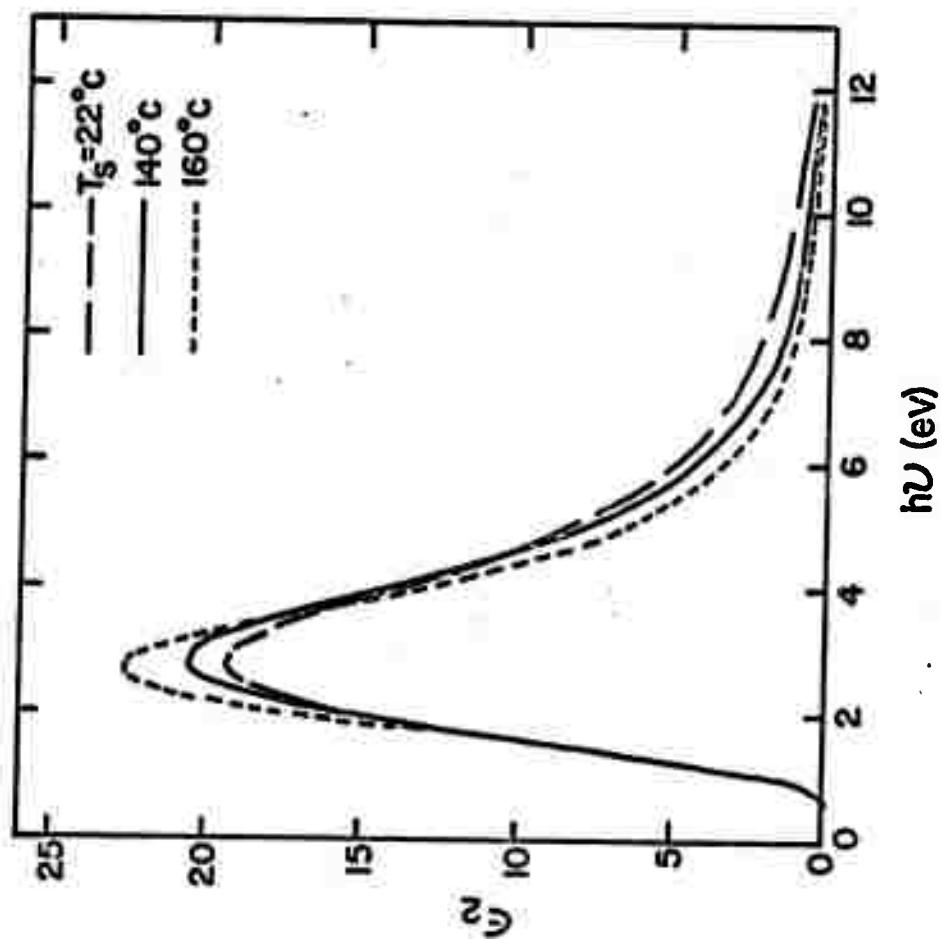


Fig.1

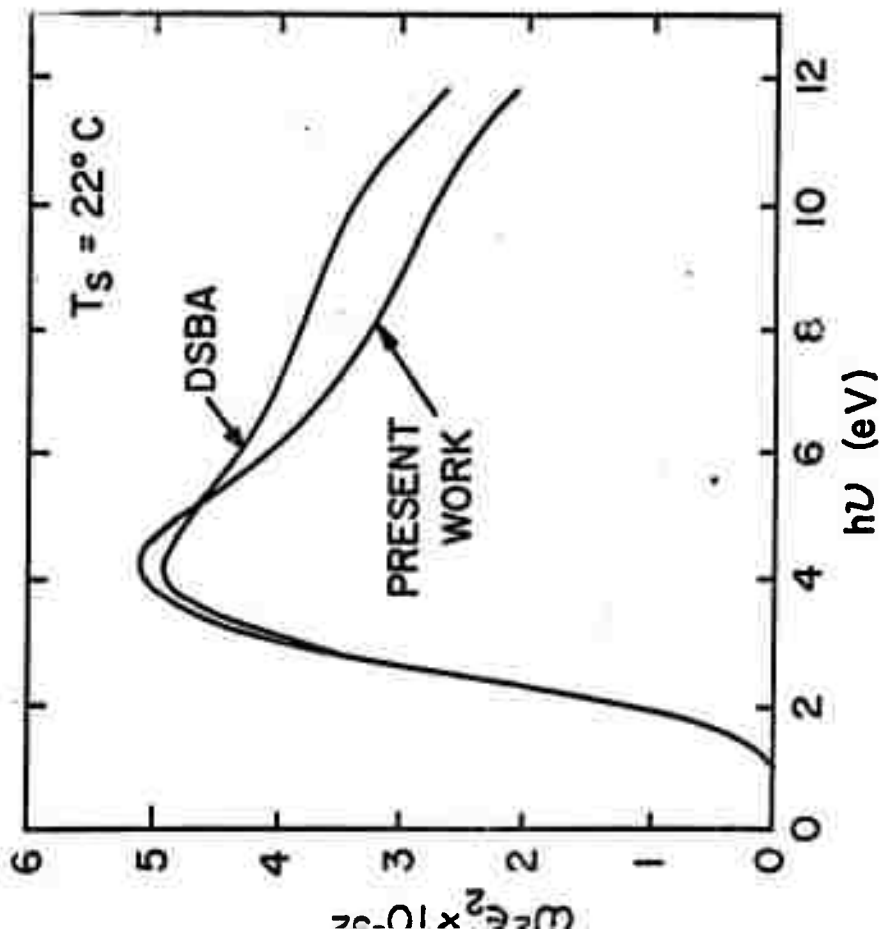


Fig 3

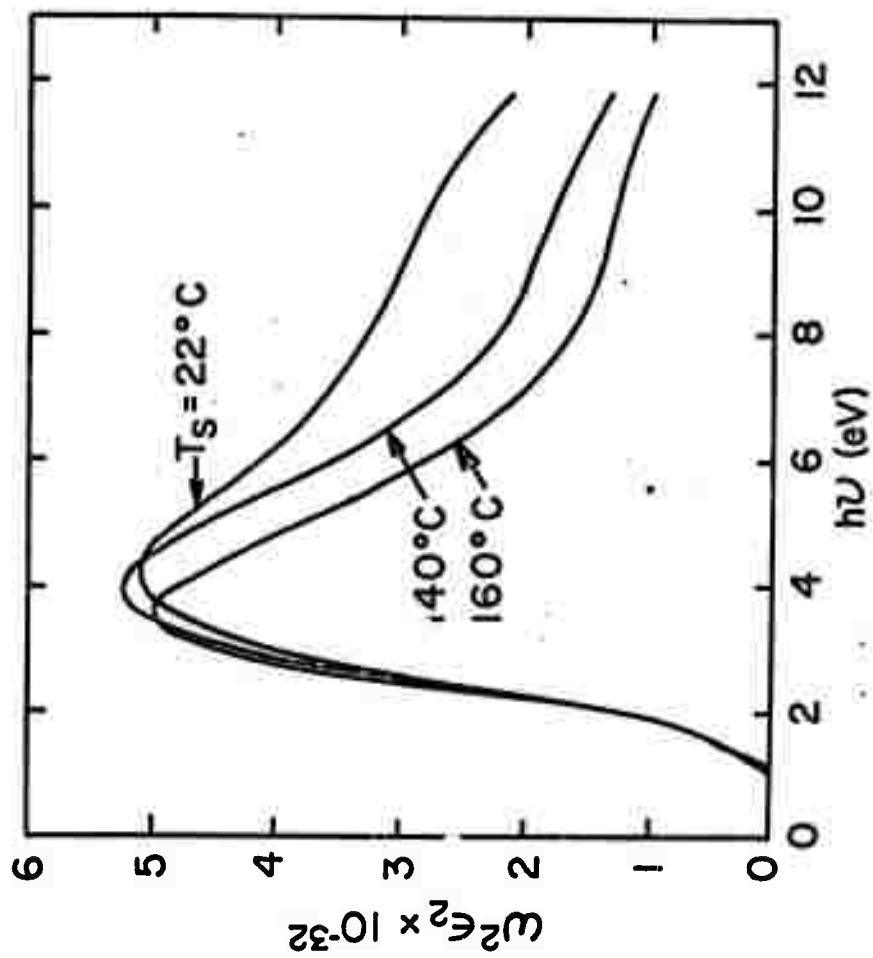


Fig 4

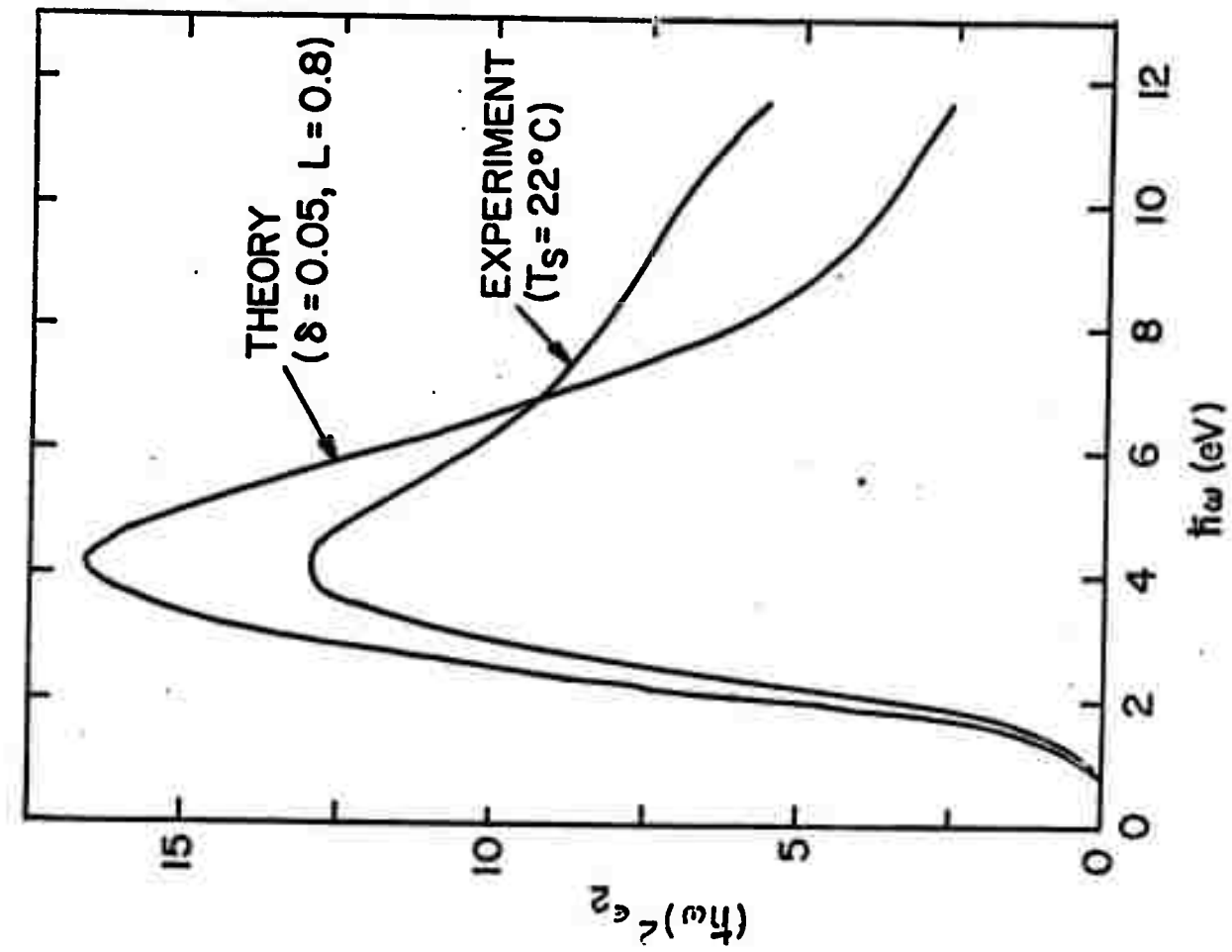


Fig. 5

Photoemission Investigation of Amorphous Germanium†

C. G. Ribbing,* D. T. Pierce, and W. E. Spicer

Stanford Electronics Laboratories, Stanford University, Stanford, California 94305

(Received 30 June 1971)

Photoemission measurements of amorphous germanium films have been made in the photon energy range 6.2–11.7 eV. A spectrum with one broad peak 1.25 eV below the high-energy cutoff is obtained, similar to earlier results of Spicer and Donovan. By comparison with gold spectra and using simple models for the resolution function and the high-energy edge in the electron distribution, the valence-band edge is placed 0.31 ± 0.05 eV below the Fermi energy, with no evidence for tailing of the density of states into the gap. Careful annealing measurements through several temperatures below the crystallization temperature showed no gradual changes until the rather abrupt appearance of crystalline structure after anneals to 300 and 350 °C. Deposition at rates of 2 and 26 Å/sec gave no significant change, nor did deposition onto substrates at –170–150 °C. The absolute photoelectric yield was measured, and its energy dependence found to be in very good agreement with recent theoretical results of Balian et al. During successive annealings the yield first increased and then decreased to a significantly smaller value than the amorphous yield. A tentative explanation of this behavior is given within a random-network description of amorphous germanium.

I. INTRODUCTION

The electronic structure of amorphous germanium films has been intensively studied during recent years. Important contributions have been the theoretical work of Mott,^{1,2} the optical and electrical measurements by Clark,³ the optical studies of Tauc *et al.*,^{4–6} the photoemission and optical measurements by Spicer and Donovan,^{7–9} and the very recent studies of optical properties and their dependence on annealing and deposition rate by Theye,^{10,11}

In the work reported here, which is an extension and refinement of the photoemission measurements of Spicer and Donovan, we particularly wanted to study how the annealing properties of amorphous Ge films varied with deposition conditions such as substrate temperature and evaporation rate. We also aimed to locate the Fermi level with respect to the valence-band edge. Since there has been considerable discussion⁶ about tailing of the density of states into the gap, we also considered it worthwhile to repeat Spicer and Donovan's⁹ comparison of photoelectron energy distribution curves (EDC's) for amorphous Ge with the EDC's of the same film annealed *in situ* until characteristic crystalline structure appeared.

II. EXPERIMENTAL

The measurements were performed with light monochromated to a full width at half-maximum of 0.10–0.20 eV over a photon energy range $6.2 \leq h\nu \leq 11.8$ eV. The upper limit was set by the transmission cutoff of the LiF window on the ultrahigh-vacuum chamber. The photoelectron energy was measured with the retarding-field energy analyzer containing a spherical screened emitter, described by

DeStefano and Pierce.^{12,13} The energy distribution curves were obtained using the ac modulation technique reported by Spicer and Berglund¹⁴ and by Eason.¹⁵ The substrate holder was essentially a block of annealed copper which could be pivoted out of the collector so that the substrate was in a horizontal position for evaporation. The substrate was a polished disk-shaped single crystal of Ge (*p* type, 11 Ω cm, from semimetal). The substrate holder contained a heater and a thermocouple used to monitor the sample temperature.

A special cooling device was constructed which allowed the sample to be cooled to near liquid-nitrogen temperature. It consisted principally of a 15-cm-long 5-mm-thick flexible bundle of hydrogen-fired 0.013-mm oxygen-free high-conductivity (OFHC) copper wires, the ends of which were brazed into blocks of annealed copper. One block was tightly screwed onto the tip of a cold finger that could be filled with liquid nitrogen from outside of the chamber. The other end was connected to the substrate holder via a polished sapphire disk 1 mm thick, providing good thermal conduction to the substrate, but also electrical insulation from the chamber. An extra Pyrex washer had the effect of increasing the mechanical pressure between disk and substrate when the metal parts thermally contracted. This way of cooling does not give quite as low a final temperature as cooling the substrate directly with liquid nitrogen, but the extra noise due to the vibrations from the boiling liquid is avoided. A test showed that with this set up we could change the sample temperature from –170 to +600 °C both in the emission and evaporation positions.

After roughing, bake out, and pump down to ultrahigh vacuum, the substrate was heat cleaned at

more than 450 °C for about 15 min, and the *e* gun and source material were outgassed by preevaporation with the shutter closed. The evaporations were made with an *e* gun 48 cm from the substrate. The material used was intrinsic grade polycrystalline Ge obtained from Eagle-Picher. The rate of deposition and the final film thickness were monitored with a quartz microbalance mounted next to the substrate. All films studied in this work were about 1000 Å thick. During the evaporations the chamber base pressure of 1×10^{-10} Torr rose to 7×10^{-9} Torr for a deposition rate of 2 Å/sec. The higher deposition rate of 26 Å/sec increased the pressure to 1×10^{-7} Torr.

III. RESULTS AND DISCUSSION

Comparison to Previous Experiment

An EDC from a film evaporated onto a room-temperature ($RT \approx 293$ °K) substrate at a rate of 2 Å/sec is compared in Fig. 1 to an EDC measured by Spicer and Donovan.⁹ While there is general overall agreement, the two noticeable differences in our EDC are the 0.25-eV shift of the main peak to higher energy and the extra, very weak structure 3 eV below the main peak. We attribute the shift of the main peak to the improved resolution obtained using the screened-energy analyzer.¹² We locate the position of the main peak 1.25 eV below the valence-band edge. The new structure is too weak for us to conclude whether or not it is due to a real increase in the initial density of states. It appears just as probable that it originates from a superposition of scattered electrons onto the bottom of the valence band. This weak shoulder is visible through several photon energies, 10.2–11.7 eV, at about the same position relative to the main peak. When the measurements on this film were repeated at a sample temperature of -170 °C, a sharpening

of the leading edge of about 0.08 eV was observed at lower photon energies. We attribute this shift to a reduced electron-phonon scattering.

Location of Valence-Band Edge

A difficult problem in photoemission studies of semiconductors is to place the high-energy cutoff properly, thereby locating the valence-band edge. The cutoff in the semiconductor is caused by the density of states and is not so steep as the metallic cutoff due to the Fermi function at RT. Also since the edge is broadened by the instrumental resolution function, it is necessary to somehow deconvolve the experimental curve to find the true cutoff in the density of states. (We shall use the concept of resolution function, meaning the experimental curve obtained from measuring an emitted δ -function distribution. Effectively, it is the same as the conventional "window" in ordinary spectroscopy, only with the opposite shift in nonsymmetric cases.)

In order to find the valence-band edge in amorphous Ge we have used the following procedure based on comparison with the cutoff for a metal. The EDC's of Au films were recorded in the same geometry and at the same low photon energies as the Ge films. Taking the metallic cutoff as the midpoint of the linear part of the high-energy edge gave a total width of the EDC which was in excellent agreement with the difference between the photon energy and work function of the collector as determined independently by a Fowler plot of the yield. Such a cutoff in the middle of the high-energy edge indicates that the resolution function is symmetric as can be seen from the idealized case in Figs. 2(a) and 2(b). A symmetric (case 1) and nonsymmetric (case 2) resolution function are shown in Fig. 2(a), where the arrows symbolize the emitted δ -function distribution of electrons. The nonsymmetric resolution of case 2 shifts the edge to lower energy and hence shifts the cutoff away from the middle of the linear region. Since imperfect analyzer geometry gives a nonsymmetric resolution function as in case 2, we suggest that this error is unimportant compared to random errors such as an unevenness in the analyzer work function and the spectral linewidth of the light. The principal reason for the insignificant geometrical error is probably the screened-emitter analyzer.

In order to get a quantitative description, the two simple models of a rectangular and triangular resolution function are treated in Figs. 2(c)–2(f). The true emitted density of states in the metal is assumed to be broadened only by the Fermi function which we approximate by a straight edge like the dotted distribution in Fig. 2(c). This model neglects the curvature of the Fermi function close to 0 and 1, but since we are only going to use the straight middle part of the edges in our analysis we

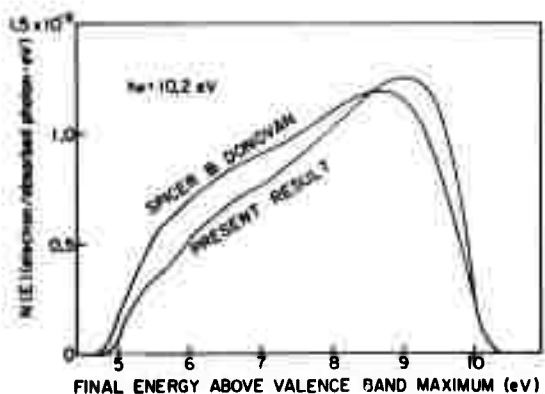


FIG. 1. A comparison of amorphous Ge EDC's of Spicer and Donovan (Ref. 9) and of the present work showing the 0.25-eV shift of the main peak and the extra low-energy structure 3 eV below the main peak.

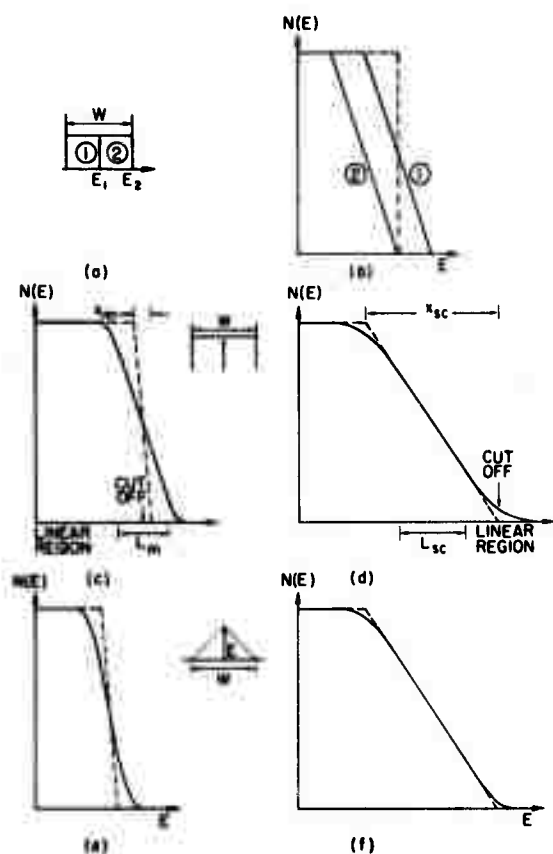


FIG. 2. Convolution of linear edges with model resolution functions: (a) symmetric and nonsymmetric rectangular resolution functions; (b) the effect of convolving a step-shaped edge with the resolution functions in (a) showing the shift of the edge in a nonsymmetric case; (c) "metallic" case, showing the convolution of a rectangular distribution function with a linear edge of smaller width; (d) "semiconductor" case, convolving a rectangular distribution function with a linear edge of larger width; (e) like (c) but with a triangular resolution function; (f) like (d) but with a triangular resolution function.

consider this to constitute a reasonable first approximation. By convolving¹⁶ the rectangular resolution function with the true distribution (dotted line) we obtain the measured distribution (full line). The measured EDC will have a linear region with a corresponding interval L_m on the E axis. The relation, $L_m = W - x_m$, where W is the width of the resolution function and x_m the width of the true distribution, is easily found. To determine the instrumental constant W it remains to decide what width x_m should be attributed to the metallike distribution. This is done either by merely plotting the room-temperature Fermi function or by using the first-order expansion $f(E) = \frac{1}{2} [1 - (E - E_f)/2kT]$ and extrapolating to $f(E) = 0$ and 1. In both cases, at 20 °C a value of $x_m = 0.10$ eV ($\approx 4kT$) is obtained. L_m is determined from the measured Au EDC's to be 0.15 eV with

good reproducibility through several low photon energies. We conclude from the Au measurements and from an analysis of these simple models that the resolution function is symmetric with a width $W = 0.25$ eV.

For comparison, the effect of a triangular window is shown in Fig. 2. The same over-all effect of this convolution is observed, i.e., rounding off corners and leaning the edge back. The rectangular resolution function was chosen for the analysis of the experimental results since it appears to give marginally better agreement with the experimental shape and is simpler to convolve.

A striking feature in the experimental EDC's from the amorphous Ge is that their leading edges also have a linear part. This indicates that the true distribution has a linear region of at least the same length. We take as the simple model for the semiconductor case a linear edge as represented by the dashed line in Fig. 2(d). The difference from the "metallic" edge is that the slope is considerably less steep and the true cutoff is at the end of the edge. Figure 2(d) shows the result of convolving this edge with the same resolution function as in Fig. 2(c). Two observations should be made. A large linear region is obtained in the middle of the edge and, as is to be expected when the resolution function has a smaller width than the measured structure, the slope of the edge is retained in that linear region. For the semiconductor, the relation between the linear edge and the width of the resolution function is $L_{sc} = x_{sc} - W$. The location of the true cutoff is $\frac{1}{2}W$ higher than the end of the linear region, which coincides with the extrapolation of the linear part to the E axis. It is not practical to relate anything to the cutoff of the instrumentally broadened EDC since the high-energy "foot" is disturbed by noise and zero line drift. Again for comparison, the effect of a triangular resolution function on the same edge is demonstrated in Fig. 2(f). This model appears to exaggerate the linearity of the experimental edge.

The application of the analysis above to recorded curves of Au and Ge is shown in Fig. 3. Average values of $L_{sc} = 0.29$ and $x_{sc} = 0.54$ eV are found. The valence-band edge is placed 0.31 ± 0.05 eV below the Fermi level by measurements from several EDC's at different low photon energies. The extrapolation of the linear part of the edge is in all cases in very close agreement to the cutoff obtained in this analysis, which shows the consistency of our simple models with the experimental results.

Results from Annealed Films

The amorphous films obtained by evaporation were all annealed in successive steps by raising the substrate temperature for about 1 h to a predetermined value and remaining at that temperature

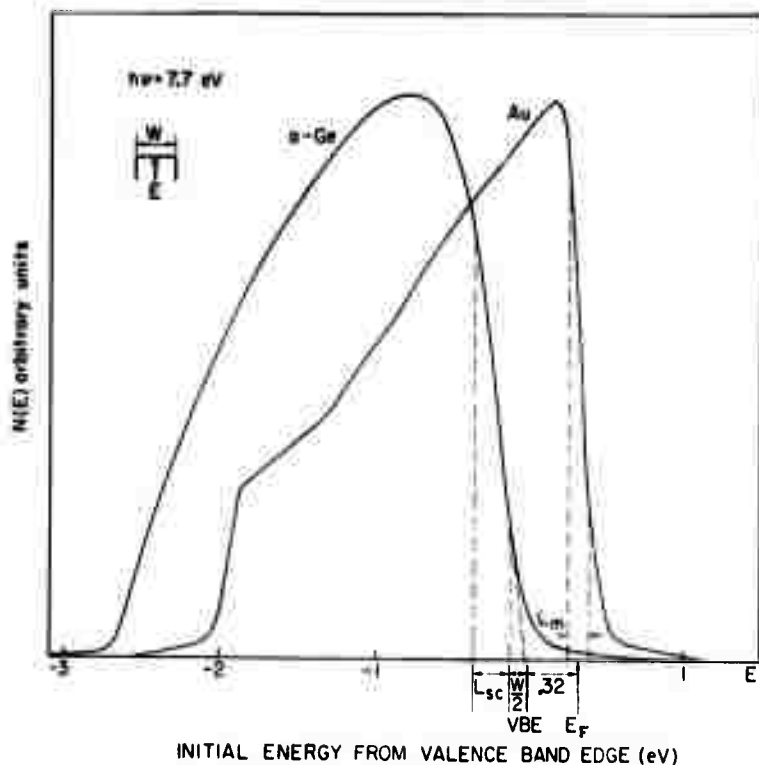


FIG. 3. Location of the valence-band edge of amorphous germanium using EDC's from Ge and Au recorded in the same geometry.

for half an hour. A precision of $\pm 5^\circ\text{C}$ was usual. The dramatic effect of heat treatment at 300°C and above is demonstrated in Fig. 4. The broad structureless EDC of the amorphous material is transformed into the rich structure typical for crystalline Ge. After the final photoemission experiment it was furthermore verified by x-ray diffraction that the film gave (220) diffraction peaks that were not present on the other side of the (111)-oriented substrate. From the width of the diffraction peaks the size of the crystallites was estimated to be 200–300 Å.

Again the qualitative agreement with the annealing experiment of Spicer and Donovan⁸ is satisfactory, but there is a shift in the crystallization temperature. Structure characteristic of crystalline film is apparent in our EDC's after annealing at 250 – 300°C and is fully developed after annealing at 300 – 350°C . The corresponding temperature intervals for the Ge films of Donovan and Spicer are 300 – 400 and 400 – 450°C , respectively, and the EDC's display a more gradual change. There still remains some uncertainty about the source of these differences. Adamski¹⁷ has shown experimentally that the amorphous to polycrystalline and polycrystalline to epitaxial transformation temperatures are very sensitive to oxygen partial pressures as low as 5×10^{-9} Torr during evaporation. Nowick¹⁸ also argues that the presence of any impurities that are insoluble in the crystalline phase stabilizes the amorphous phase. Crystallization would force

such impurities to separate out in a second phase which corresponds to a high activation energy. The 1×10^{-11} Torr base pressure quoted by Spicer and Donovan is better than ours, so the only apparent source of extra oxygen in their experiment is their higher pressure during evaporation, 1×10^{-7}

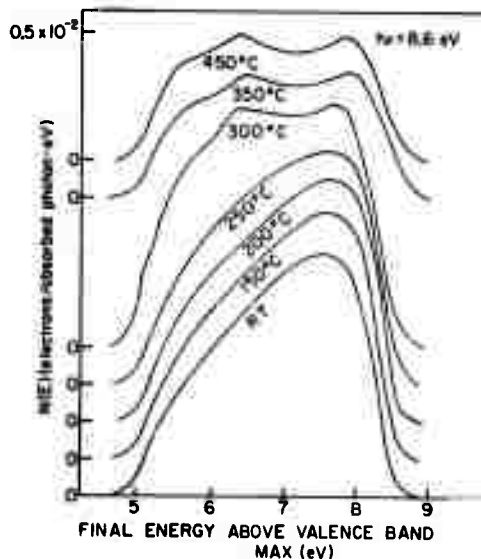


FIG. 4. The effect of annealing on the EDC's of amorphous Ge films. The curves are normalized to the absolute photoelectric yield.

Torr as compared to our 7×10^{-9} Torr. We note however that the poorer vacuum with the high evaporation rate discussed below did not effect the crystallization temperature. The preparation of the crystalline substrates, polishing and later heat cleaning in high vacuum, was virtually identical in both experiments so approximately the same amounts of substrate oxides were probably present initially.

As was originally noted by Spicer and Donovan the high-energy edge of the EDC's for amorphous Ge is at least as sharp as for polycrystalline Ge. In fact the crystalline edge is somewhat less steep, which can be understood as an effect of parabolic bands. It should be noted, however, that photoemission alone cannot rule out the possibility of a very small density of states in the gap $\sim 10^{17} \text{ cm}^{-3}$, as reported by Tauc, Menth, and Wood¹⁹ for amorphous As_2S_3 .

A striking feature of Fig. 4 is the similarity between the EDC's from films heated only up to 250 °C. This result is different from the recent results of Thèye¹⁰ who observes a gradual change in refractive index and absorption coefficient for annealing temperatures well below the crystallization temperature (400 °C). Thèye attributes this change to unsatisfied bonds which decrease in number when the film is annealed. We believe that these unsatisfied bonds are surface states on microvoids as demonstrated for amorphous Si by Moss and Graczyk.²⁰ Arguing against the presence of microvoids, Thèye claims that her films showed no decrease in density when annealed. A decrease, however, should only occur if the voids migrated to the surface, but not if they merely coalesced and thereby reduced the void surface and the number of "dangling bonds."

Independent of what the defects are that cause the gradual changes upon annealing in Thèye's films, it seems as if they are not present in our films. A shift in the absorption edge of about 0.4 eV (Fig. 4, Ref. 10) would show up in the EDC's unless all the shift was due to a change in the final density of states below the vacuum level, an assumption that appears rather artificial. The obvious reason for the absence of defects should then be the several-orders-of-magnitude-lower base pressure in our case. Thèye's high deposition rate almost makes up for the quoted 10^{-6} -Torr evaporation pressure from the point of view of contamination. The fact that the crystallization temperature, however, was 100 °C higher than ours seems to indicate the presence of more impurities^{17,18} as discussed above. The importance of Thèye's work therefore is that it demonstrates that it is possible by careful annealing to approach "the perfect amorphous state" obtainable directly in uhv. In view of these experiences it is tempting to speculate that the controversy^{3,8,7,21} about tailing in the density of states into the forbidden gap is caused by

different preparation techniques giving rise to more or less voids²² in the film. The number of voids is substantially reduced if the film is deposited under clean conditions in ultrahigh vacuum.

Recently it has been noted by Donovan²³ and Spicer that Ge typically evaporates in the forms Ge_1 , Ge_2 , Ge_3 , and Ge_4 and that the composition of the material striking the substrate could effect the characteristics of amorphous films so formed. One would expect the "perfect" amorphous film to be most closely approached when Ge arrives at the substrate as separated atoms. Low evaporation temperatures and long evaporation distances should maximize this since the fraction of atomic Ge is highest at low temperatures and since as the evaporation distance is increased, the probability of Ge_2 , Ge_3 , or Ge_4 breakup to produce more atomic Ge is increased. We did not check this hypothesis but we consider it to be a possible explanation for the discrepancies reported in the literature on the properties of amorphous germanium.

Effect of Substrate Temperatures

In subsequent evaporations the effect of different substrate temperatures was investigated. This is exemplified for the substrate temperatures -170, 20, 150, and 260 °C in Fig. 5. The slight broadening of the 150 °C curve is most likely due to the fact that it was recorded with a conventional diode analyzer rather than with the screened-emitter analyzer. We find it a rather remarkable verification of the well-defined properties of amorphous Ge that the EDC's varied so little over a range in substrate temperature as large as 320 °C.

Apparently, the 260 °C substrate temperature was just as effective to crystallize the material as a 300 °C anneal. This is easy to understand, as pointed out by Nowick,¹⁸ from the fact the mobility required for crystallization is easier to obtain on a free surface during an evaporation than in the already built-up film. The films evaporated at the three lower temperatures all crystallized in the same 250–350 °C range in contrast to the observation of Thèye¹¹ who reports a lower crystallization temperature the higher the substrate temperature. Tentatively, we suggest that this discrepancy is due to the larger amount of voids in Thèye's films. The voids in the imperfect amorphous film impede crystallization, but they are reduced in number when the substrate is heated due to the higher surface mobility of the impinging atoms.

The object of the 260 °C evaporation was to see if the high-density form of amorphous Ge, reported by Donovan *et al.*,²² had some characteristic feature in photoemission. Due to the lower crystallization temperature this question remains to be answered. In principle the high-density phase could have been formed on the 150 °C substrate,

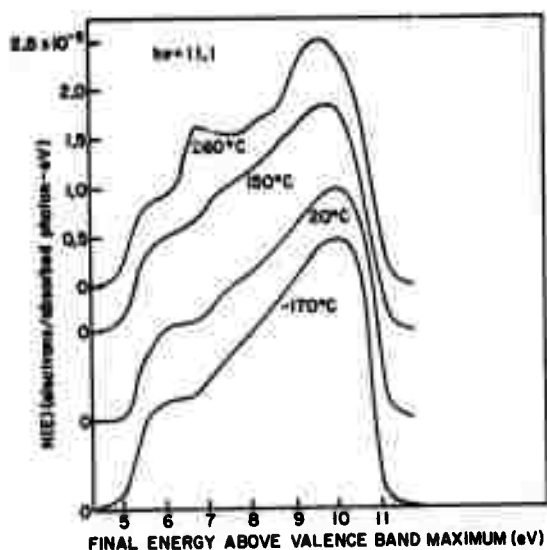


FIG. 5. The effect of different substrate temperature on the EDC's of Ge films. The 150°C curve was recorded with a conventional diode analyzer.

but in such a case the same EDC's were obtained as in the case of the normal-density amorphous film.

Effect of Rate of Deposition

To investigate what influence the evaporation rate could have on the EDC's of amorphous Ge, one evaporation was tried with as high a rate as was possible within the constraints of the long source-to-substrate distance and the desire to maintain a pressure $\leq 1 \times 10^{-7}$ Torr. A rate of 26 Å/sec was recorded. This is far from the 200 Å/sec reported by Th  ye,^{10,11} but it was hoped that any gross effect of deposition rate would be revealed by the increase from 2 to 26 Å/sec. A pressure of 1×10^{-7} Torr during an evaporation of more than 30 sec corresponds to a maximum contamination of 1 to 2 monolayers of gas molecules over the 1000 Å of the film. Therefore, it is not conclusively demonstrated that the shift to lower energy of the main peak and the broadening of the high-energy edge in Fig. 6 really stems from the high evaporation rate. The possibility of contamination cannot be ruled out.

Photoelectric Yield

The yield of photoemitted electrons per incident photon was measured over the entire energy range using a calibrated Cs₃Sb photocell²⁴ and a +45 V bias on the collector. The absolute yield was calculated using the formula $Y = y/(1 - R)T$, where y is the yield found from measurement, R is the reflectivity of the film, and T is the transmission of the LiF window. Since no reflectivity data for fine grain polycrystalline films were available we chose to

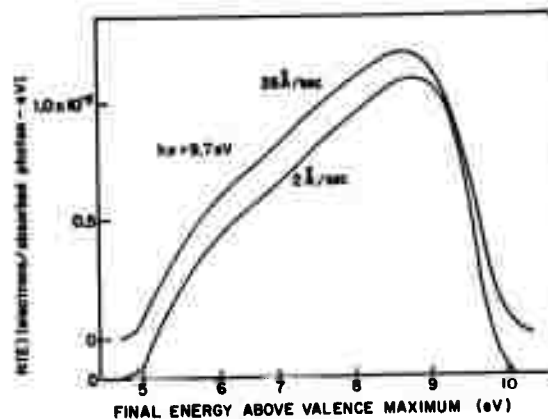


FIG. 6. Two normalized EDC's of Ge films deposited on RT substrate at different rates.

use reflectivity data for amorphous Ge.

The resulting yields for amorphous and annealed film are presented in Fig. 7. At high energies the yield of the amorphous film is between the yield of the film annealed at 300 and 450°C. We believe that this surprising result can be interpreted in the following way. Assuming that our amorphous Ge forms an ideal or almost ideal tetrahedral random network,²⁵ it is easily conceived that the thermal scattering is higher than in a single crystal with

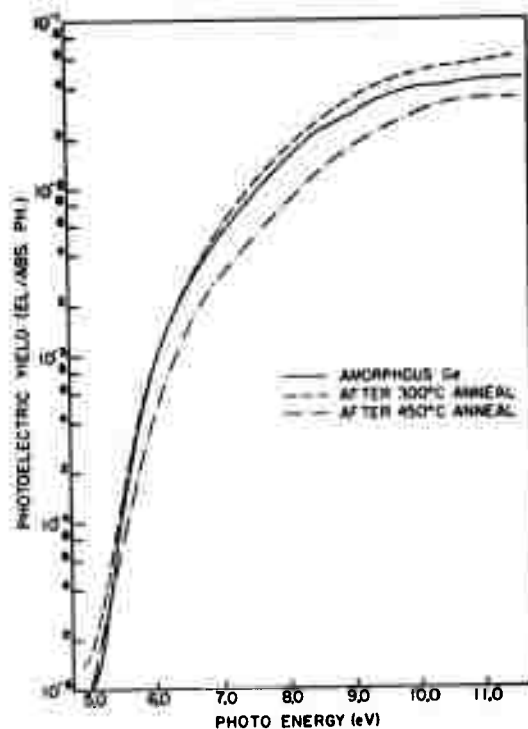


FIG. 7. The absolute photoelectric yield for an as deposited Ge film, after a 300°C anneal and after a 450°C anneal.

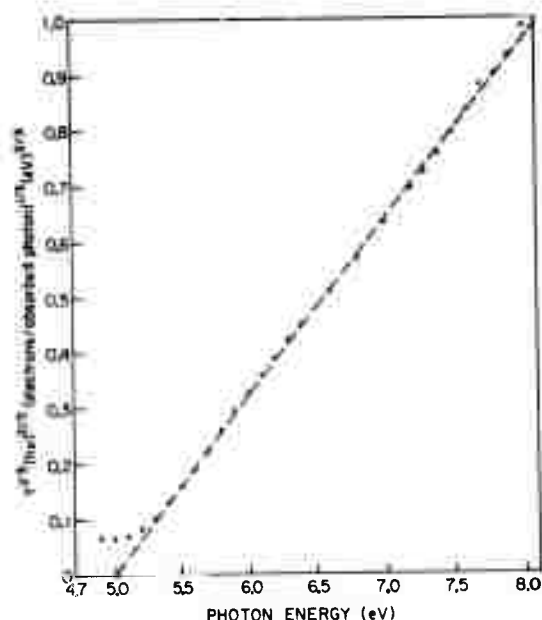


FIG. 8. The photoelectric yield of amorphous Ge fitted to the relation of Ref. 28.

long-range order. This will give the amorphous film a higher yield since increased probability of elastic or almost elastic scattering will increase the probability that an excited electron reaches the escape cone.²⁶ This argument is based on the assumption that the electron-electron scattering length is larger than the defect scattering length. The first annealing step to 300 °C can then be understood as breaking up the network and creating small crystallites ($\ll 200$ Å). The large amount of internal surface barriers will increase the total scattering giving rise to the higher yield obtained. Continued annealing to 350–450 °C increases the grain size which will reduce the scattering and thus the yield in complete qualitative agreement with the results in Fig. 7. The choice of amorphous reflec-

tivity data cannot be responsible for this effect, since reflectance values reported²⁷ for crystalline Ge would make the yield for the 450 °C annealed film even lower by as much as 25% at 11 eV. It could, however, make the difference between the amorphous and the 300 °C annealed film much smaller. It can be remarked that this behavior of the yield through annealing would be very difficult to reconcile with any kind of microcrystalline model where the annealing process has to be conceived as a successive growth of microcrystallites.

Attempts to fit the energy dependence of the yield for the amorphous film to any simple power law²⁸ failed, even for energy ranges close to threshold. Very recent results of Ballantyne,²⁹ however, gave a remarkably good fit over a range of almost 3 eV as seen in Fig. 8. The energy dependence of the yield derived by Ballantyne for the case of a rectangular energy distribution of excited electrons is $Y \propto (h\nu - \phi)^3 / (h\nu)^2$, where $h\nu$ is the photon energy and ϕ is the threshold. The derivation of this formula includes a smearing out of the rectangular distribution by a phenomenological scattering against phonons, defects, impurities, or surfaces. The extrapolated value for the threshold is found to be 4.98 ± 0.04 eV, in good agreement with the sum of the values for the work function 4.63 ± 0.04 eV and the difference in energy between Fermi level and valence-band maximum 0.31 ± 0.05 eV that were obtained from the EDC's.

ACKNOWLEDGMENTS

We would like to thank Professor J. M. Ballantyne for giving us access to his results prior to publication and for several valuable comments. We would like to thank Dr. T. Donovan for providing the reflectivity data for amorphous germanium as well as for several informative discussions. We also want to express our appreciation of the endurance and skill displayed by Phil McKernan in constructing the cooling device.

†Work supported by the Advanced Projects Agency through the Army Office of Scientific Research and through the Center for Material Science at Stanford University.

*On a grant from the Swedish Board for Technical Development.

¹N. F. Mott, *Advan. Phys.* **16**, 49 (1967).

²N. F. Mott, *Phil. Mag.* **19**, 835 (1968).

³A. H. Clark, *Phys. Rev.* **154**, 750 (1967).

⁴J. Tauc, R. Grigrovič, and A. Vancu, *Phys. Status Solidi* **15**, 627 (1966).

⁵J. Tauc, *Mater. Res. Bull.* **3**, 37 (1968).

⁶J. Tauc, A. Abraham, R. Zallen, and M. Slade, *J. Non-Cryst. Solids* **4**, 279 (1970).

⁷T. M. Donovan and W. E. Spicer, *Phys. Rev. Letters* **22**, 20 (1969); **22**, 1058 (1969).

⁸W. E. Spicer and T. M. Donovan, *Phys. Rev. Letters*

24, 11 (1970); **24**, 595 (1970).

⁹W. E. Spicer and T. M. Donovan, *J. Non-Cryst. Solids* **2**, 66 (1970).

¹⁰M. L. Thèye, *Mater. Res. Bull.* **6**, 2 (1971); **6**, 103 (1971).

¹¹M. L. Thèye, *Opt. Commun.* **2**, 329 (1970).

¹²T. DiStefano and D. Pierce, *Rev. Sci. Instr.* **41**, 180 (1970).

¹³D. Pierce and T. DiStefano, *Rev. Sci. Instr.* **41**, 1740 (1970).

¹⁴W. E. Spicer and C. N. Berglund, *Rev. Sci. Instr.* **35**, 1665 (1964).

¹⁵R. C. Eden, *Rev. Sci. Instr.* **41**, 252 (1970).

¹⁶E. A. Guillemin, *Theory of Linear Physical Systems* (Wiley, New York, 1963), Chap. 13.

¹⁷R. F. Adamsky, *J. Appl. Phys.* **40**, 4301 (1969).

¹⁸A. S. Nowick, *Comments Solid State Phys.* **V2**, 155

(1970).

¹⁹J. Tauc, A. Menth, and D. L. Wood, Phys. Rev. Letters 25, 749 (1970).

²⁰S. C. Moss and J. F. Graczyk, Phys. Rev. Letters 23, 1167 (1969).

²¹J. W. Osmun and H. Fritzsche, Appl. Phys. Letters 16, 87 (1970).

²³T. Donovan (private communication).

²²T. M. Donovan, E. J. Ashley, and W. Spicer, Phys. Letters 32A, 85 (1970).

²⁴R. Y. Koyama, thesis, Technical Report No. 5223-1, Appendix 1 (Stanford University, (1969) (unpublished)).

²⁵D. E. Polk, J. Non-Cryst. Solids 5, 365 (1971).

²⁶R. N. Stuart and F. Wooten, Phys. Rev. 156, 364 (1967).

²⁷H. R. Philipp and H. Ehrenreich, Phys. Rev. 129, 1550 (1963).

²⁸E. O. Kane, Phys. Rev. 127, 131 (1962).

²⁹J. Ballantyne, Phys. Rev. (to be published).

Electronic Structure of Amorphous and Polycrystalline GeTe*

G. B. Fisher and W. E. Spicer

Stanford Electronics Laboratories, Stanford University, Stanford, Calif. 94305

Photoemission and ultraviolet reflectance measurements have been made on amorphous and polycrystalline GeTe in order to compare their electronic structure. Since structural studies^{1,2} and ESCA measurements³ have shown the coordination of amorphous GeTe to be considerably lower than that of the crystal and the bonding of amorphous GeTe to be considerably more covalent, the GeTe system offers a unique opportunity to look at the effect of large changes in local order (as well as the loss of long range order) within the same composition.

Energy distribution curves (EDCs) of photoemitted electrons were measured in situ with a cylindrical analyzer from films sublimed onto a polished molybdenum substrate from a charge of GeTe fourteen centimeters away. The films, whose thicknesses varied from 1300 Å to 2500 Å, were deposited at a rate of about 15 Å/sec while the pressure never rose above the 10⁻⁷ torr scale in a system with a base pressure less than 5 x 10⁻¹¹ torr. The amorphous films were evaporated onto a room temperature substrate, while the polycrystalline films were obtained both by annealing an amorphous film at 160°C and by evaporating onto a substrate held at 170°C. The photoelectric threshold as determined from the yield measurements⁴ was higher for the amorphous material, 5.39 ± 0.05 eV compared to 5.00 ± 0.05 eV for the polycrystalline films.

*This research was supported by the Advanced Research Projects Agency of the Department of Defense and was monitored by U. S. Army Research Office-Durham under Contract No. DMR04-70-C-0044.

Some care was taken to insure that the films studied are indeed GeTe. Transmission electron microscopy with a resolution capability of at least 50 Å was done on samples (~600 Å thick) evaporated under precisely the same conditions as the films studied. There was no sign of phase separation and the very few crystallites present occupied less than 0.1% by volume. Beam heating of the sample caused crystallization which grew uniformly in all directions. With the films actually studied in photoemission, microprobe analysis shows a uniform composition of 50% atomic Ge and 50% atomic Te within 1%. The annealed film shows the characteristic peaks of crystalline GeTe in x-ray diffraction with no Ge or Te peaks present, while as-deposited films show no peaks at all. In addition, films from successive evaporations give identically shaped EDCs. Thus far, our work supports previous studies⁵ which indicates that GeTe evaporates as a molecular vapor and forms representative thin films of stoichiometric GeTe.

The measured EDCs of amorphous GeTe are seen in Figure 1. These curves are normalized to the quantum yield and the horizontal scale has been shifted through by an order to refer the energy to initial states. The important thing to note is that two peaks are seen, one is 1.5 eV below the high energy edge and the other is about 3.1 eV below the edge. Lowering the threshold on an amorphous film to 4.2 eV by exposure to Cs showed no further structure in the EDCs except that due to increased scattering. At higher photon energies, where the threshold function which determines the low energy cutoff affects less of the EDCs, the two-peaked structure increases in final state energy by the amount that $h\nu$ is increased, characteristic of photoemission from valence band states. As expected in an amorphous material, there is no evidence in the EDCs of k-vector conserving transitions. There is also no

note that there is no gradual change in the amorphous GeTe EDCs at temperatures to 125°C, possibly indicating a relatively defect-free sample.

For a further comparison between the amorphous and crystalline forms of GeTe, we report in Figure 4 the reflectance of each measured from near 1.0 eV to 11.9 eV with an apparatus designed by Endris¹¹). The in situ sample preparation conditions were nearly identical with those in the photoemission experiment, and the amorphous film was annealed in the same way to obtain the polycrystalline sample. The resolution is 0.1 eV with a relative error in reflectance of ± 0.02 . The amorphous reflectance and photoemission data are being used in a calculation of the density of states of amorphous GeTe. The agreement with the polycrystalline film data of Tan, et al.¹²) in the region of overlap is reasonable and within their limits of error. Although the reflectances of the two forms of GeTe show marked differences in reflectance below 7 eV, above that photon energy there is a distinct similarity. This coincidence could be misleading, since it is in this very energy region that the EDCs show such striking differences between amorphous and polycrystalline GeTe.

While hoping to better understand the EDCs of amorphous GeTe, it is intriguing to note (Figure 5) that both the EDCs of amorphous Ge^{13,14}) and the present data show a peak 1.5 eV below the high energy edge. As noted earlier, amorphous GeTe is covalently bonded³), as is tetrahedrally-bonded amorphous Ge. The exact short range order of amorphous GeTe is unclear, but one model²) which fits very well the measured radial distribution function is a random covalent network in which each Ge atom is four-fold coordinated and each Te atom is two-fold coordinated. Thus, we may tentatively associate the peak at 1.5 eV with electrons related to a four-fold coordinated Ge atom.

4

modulation which would indicate important structure in the density of final states. Thus, since the transitions fit the nondirect model⁶), the EDCs are representative of the valence band density of states, and the sharp high energy edge can be considered to be the valence s-p_{3/2} maximum. Further work should indicate to what degree states in the gap and/or instrumental broadening contribute to the high energy edge.

The measured EDCs of polycrystalline GeTe are markedly different from those of amorphous GeTe over a wide range of photon energies. The EDCs of polycrystalline GeTe will be discussed in detail at another time⁷). It will suffice to say here that the data give stronger evidence for direct (k-vector conserving) transitions. The clear differences in each material are seen in Figure 2 which shows an EDC for each form of GeTe at 10.2 eV. Instead of two peaks, polycrystalline GeTe has a shoulder below the high energy edge and a main peak which falls at the minimum between the two peaks in the EDC from amorphous GeTe. The size of these differences is not unexpected considering the great change in short range order and the loss of long range order between the two forms of GeTe. In some materials⁸) it seems clear that gross optical properties are defined by the local order. If this is the case in GeTe, the largest part of the difference we see would be due to the change in coordination and bonding and not the loss of long range order.

The annealing behavior of an amorphous film of GeTe is shown in Figure 3. The film crystallized at a temperature between 125°C and 160°C, where it exhibits the characteristic EDC of the polycrystalline film. Experiments on amorphous Ge^{9,10}) indicate that annealing effects in amorphous films may be a sign of defects or microvoids in as-deposited films. It is interesting to

3

The second peak in the amorphous GeTe EDCs could then be associated with the two-fold coordinated Te atoms. This is obviously an oversimplified picture, but clearly there is evidence⁷ that optical properties can be determined by very short range order. Thus, whether we associate optical excitations with the coordination of the atoms or alternatively with the bonds themselves, we have the local order as a starting point from which to guide and examine future research.

ACKNOWLEDGMENTS

The authors wish to thank A. Bienenstock, G. Lucovsky, D. T. Pierce, and H. R. Philipp for their probing and helpful comments.

REFERENCES

1. A. Bienenstock, F. Betts, and S. R. Ovshinsky, *J. Non-Cryst. Solids* **2**, 347 (1970).
2. F. Betts, A. Bienenstock, and S. R. Ovshinsky, *J. Non-Cryst. Solids* **4**, 554 (1970).
3. F. Betts, A. Bienenstock, and C. W. Bates, *J. Non-Cryst. Solids*, this volume.
4. J. M. Ballantyne, to be published.
5. W. E. Howard and R. Tsu, *Phys. Rev. B* **1**, 4709 (1970).
6. C. M. Berglund and W. E. Spicer, *Phys. Rev.* **136**, A1030 (1964).
7. G. B. Fisher and W. E. Spicer, to be published.
8. H. R. Philipp, *J. Non-Cryst. Solids*, this volume.
9. M. L. Thèye, *Mat. Res. Bull.* **6**, 103 (1971).
10. R. S. Bauer and F. L. Galeener, *J. Non-Cryst. Solids*, this volume.
11. J. G. Endriz, *Phys. Rev. B* **2**, 1466 (1970).
12. R. Tsu, W. E. Howard, and L. Esaki, *Phys. Rev.* **172**, 779 (1968).
13. T. M. Donovan and W. E. Spicer, *Phys. Rev. Letters* **21**, 1572 (1968).
14. W. E. Spicer and T. M. Donovan, *J. Non-Cryst. Solids* **2**, 66 (1970).

FIGURE CAPTIONS

Fig. 1. EDCs from amorphous GeTe normalized to the yield and plotted with respect to initial state energy.

Fig. 2. EDCs for amorphous and polycrystalline GeTe for $h\nu = 10.2$ eV.

The zero coincides with the highest lying filled valence state in each material. Note the marked differences between the electron energy distributions.

Fig. 3. EDCs for $h\nu = 10.2$ eV from an amorphous film of GeTe annealed at several temperatures compared to an EDC from a polycrystalline film of GeTe deposited on a substrate held at 170°C . Negligible change occurs in the EDCs until the amorphous film crystallizes above 125°C . The base lines of the EDCs are spaced vertically along the right ordinate according to the temperature of the heat treatment received.

Fig. 4. Visible and ultraviolet reflectance of amorphous and polycrystalline films of GeTe. Reasonable agreement is obtained with a previous measurement (Ref. 12) of a polycrystalline film of GeTe.

Fig. 5. EDCs from amorphous GeTe and amorphous Ge (Refs. 13,14) for $h\nu = 10.2$ eV. Note the coincidence in structure 1.5 eV below the valence states maximum, possibly indicating further similarities between the two materials.

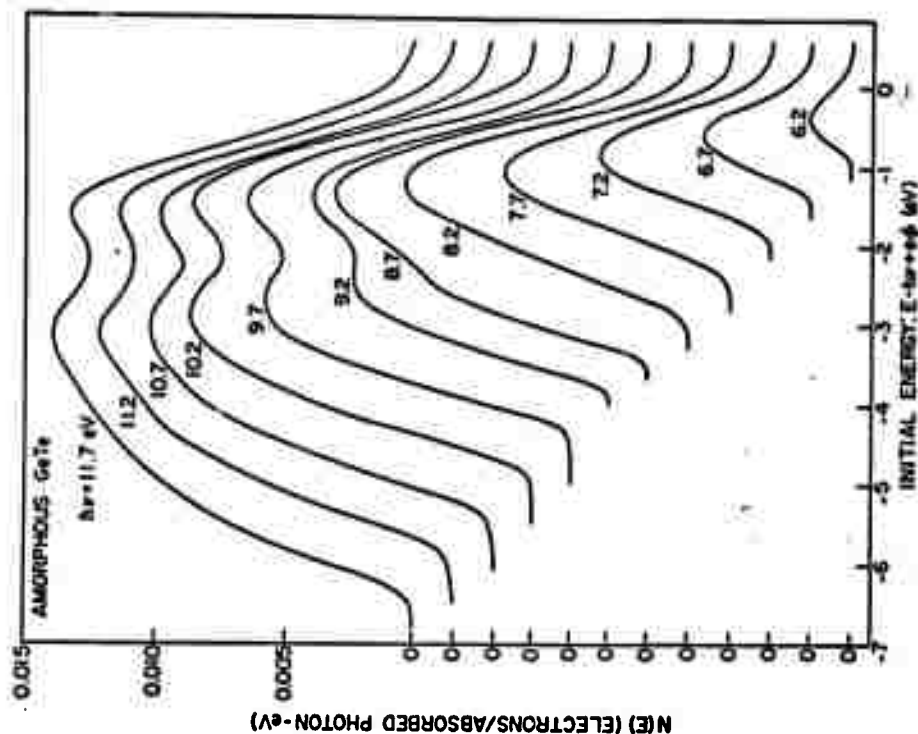


Fig. 1

Fig 3

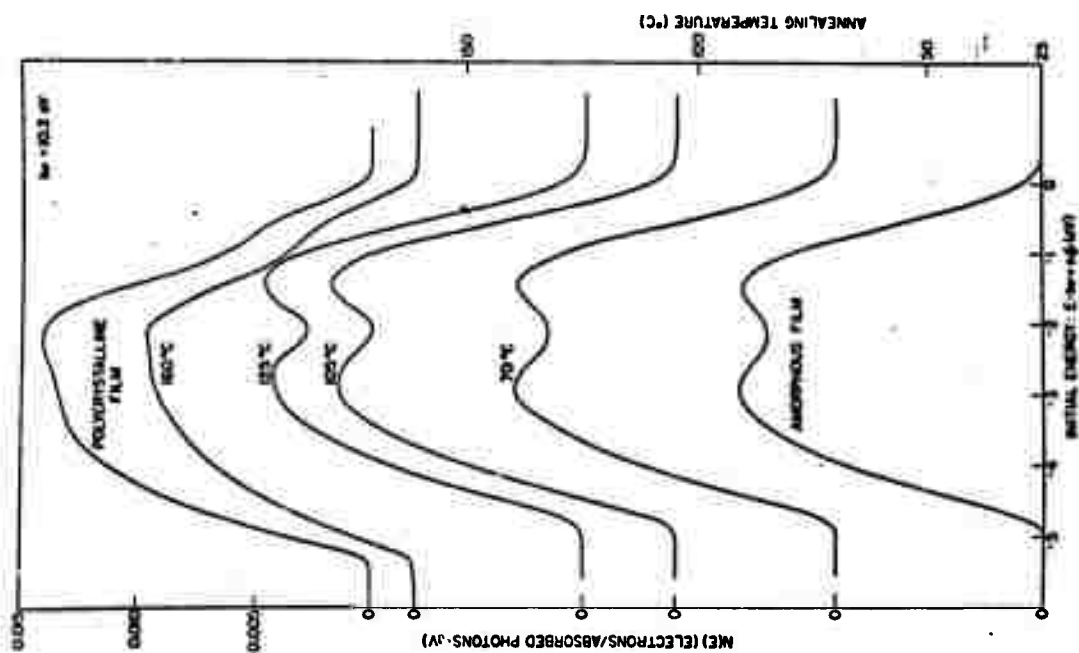


Fig 2

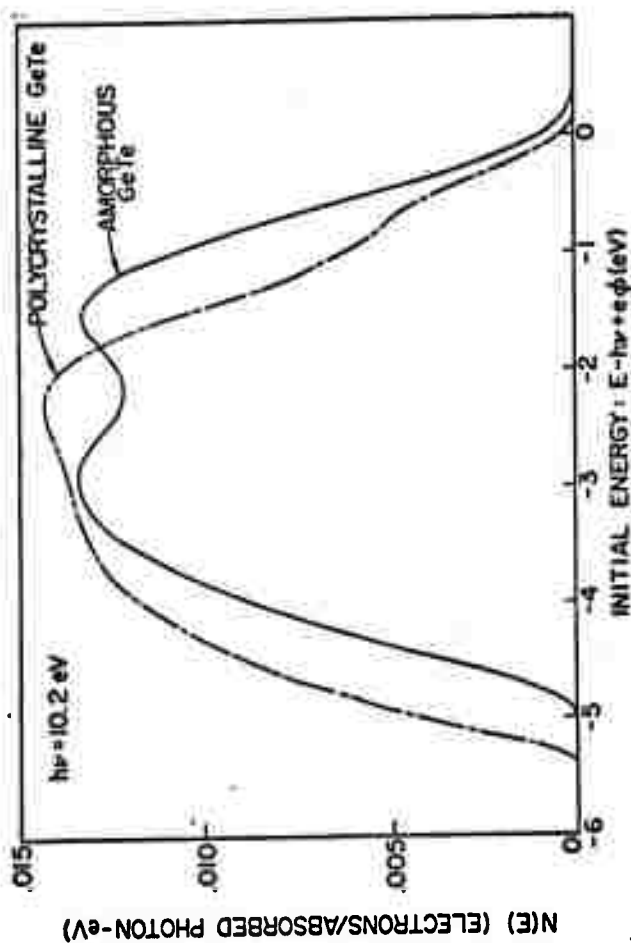


Fig. 4

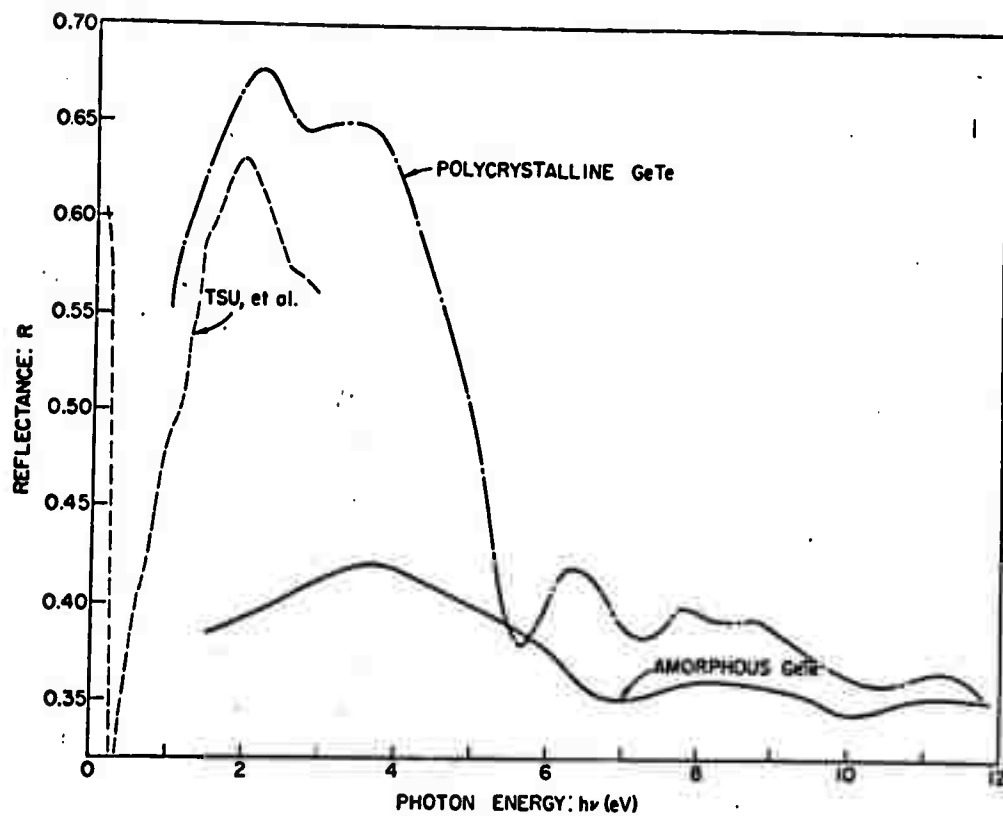
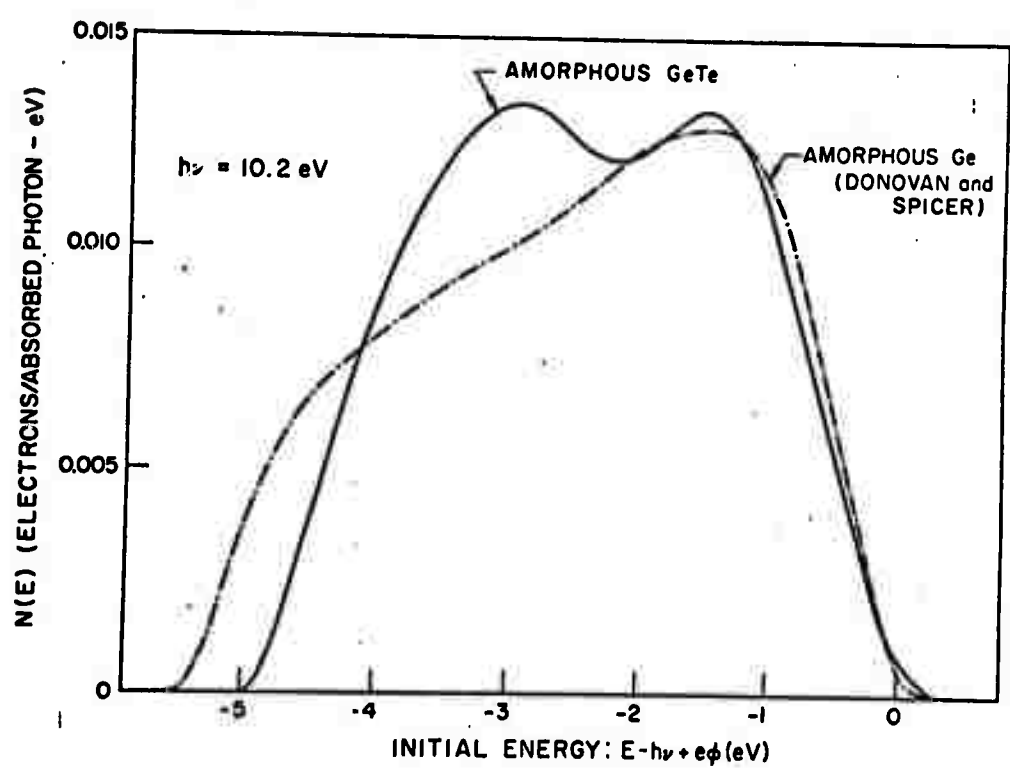


Fig. 5



I. INTRODUCTION

Recently, as a result of expanded interest in their electronic properties, the question of whether the microcrystalline model best describes certain amorphous materials has returned to the fore. Among the most significant contributions aimed at resolving this question is the work of Moss and Graczyk¹. These authors have presented the results of scanning electron diffraction studies of amorphous silicon. They compare their measured intensities with intensities calculated on the basis of various microcrystalline models and show that none of these models is capable of agreement with the measured intensity. Indeed, it seems likely, as a result of their work, that no microcrystalline model can be appropriate.

One potential shortcoming of their work, which has been suggested repeatedly at meetings, is their neglect of intercrystalline interference terms in the calculated intensities. That is, they assume that each crystallite scatters independently. With the small crystallites involved, though, these intercrystalline terms might be appreciable and might account for the discrepancies between the calculated and measured intensities. In this paper, we attempt to calculate such terms.

Before presenting the analysis, however, we first attempt to estimate the region in which interparticle interference effects might be appreciable. Let us consider the neutron scattering from liquid argon, as measured by Hanshaw². His Fig. 1 implies that interatomic interference effects constitute an appreciable portion of the total scattering only for $s(4\pi\sin\theta/\lambda) < 5$. For $s > 5$, the scattering is dominated completely by the independent scattering which is analogous to the intraparticle scattering considered by Moss and Graczyk. On the other hand, the average intercrystallite spacing in the models considered by these authors would be approximately twice the nearest neighbor distance in liquid argon. Hence, one might anticipate appreciable interparticle interference contributions only for $s < 2.5$. Yet, Moss and Graczyk find appreciable differences between the calculated and observed intensities out

CALCULATION OF THE INTERCRYSTALLINE INTERFERENCE CONTRIBUTION TO THE SCATTERING OF X-RAYS BY ARRAYS OF SMALL CRYSTALLITES^{1,2}

F. Betta¹ and A. Eilenstock²

¹Department of Materials Science and Engineering,
Stanford University, Stanford, California 94305

ABSTRACT

A general equation for the calculation of the intercrystalline interference contribution to the scattering of x-rays by arrays of small crystallites has been derived under the assumption that there is no correlation between the orientations of neighboring crystallites. Numerical calculations for the case of silicon are presented. It is shown that these intercrystalline interference terms are significantly smaller than the intracrystalline terms in all but the small angle regions. Hence, conclusions reached by Moss and Graczyk about the inability to describe the diffraction pattern of vitreous silicon in terms of microcrystalline silicon are supported. Unfortunately, the assumption of "no correlation" limits the general validity of conclusions drawn from the calculation.

to significantly larger s values. For this reason, in itself, we doubt that interparticle interference can play an important role in explaining the differences between their data and the calculations. In the region around $s = 2$, however, there are striking differences between these two which might be thus explained.

For this reason, we proceed with a calculation which indicates that the interparticle interference effects are small here, as well. We show, however, that this smallness is partly due to the model chosen for the calculation.

II. FORMULATION

Apart from multiplicative constants and slowly varying geometric factors, the intensity, $I(\underline{s})$, of scattering of x-rays by an assemblage of atoms is given by

$$I(\underline{s}) = \left| \sum_j \underline{f}_j \exp(i\underline{s} \cdot \underline{r}_j) \right|^2. \quad (1)$$

where \underline{s} is the scattering vector of magnitude $4\pi \sin \theta / \lambda$, θ is the scattering angle, λ is the x-ray wavelength, while \underline{f}_j and \underline{r}_j are the scattering factor and position vector of atom j .

We consider the sample to consist of N small crystallites, the q -th one having N_q atoms. To the atoms in this crystallite are assigned the set of numerical labels $\{n_q\}$, $n_q = 1, 2, \dots, N_q$. Then Eq. (1) can be written as

$$I(\underline{s}) = \sum_p \sum_q \sum_n \underline{f}_p \underline{f}_q^* \exp[i\underline{s} \cdot (\underline{r}_{n_q} - \underline{r}_{n_p})]. \quad (2)$$

Eq. (2) can be broken up into two terms, one of which involves the cases where $p = q$ and the other of which contains those for which $p \neq q$ so that Eq. (2) becomes

$$\begin{aligned} I(\underline{s}) &= \sum_q \sum_n \underline{f}_q \underline{f}_q^* \exp[i\underline{s} \cdot (\underline{r}_{n_q} - \underline{r}_{n_q})] \\ &\quad + \sum_p \sum_q \sum_n \underline{f}_p \underline{f}_q^* \exp[i\underline{s} \cdot (\underline{r}_{n_q} - \underline{r}_{n_p})] \\ &\equiv I_1(\underline{s}) + I_2(\underline{s}). \end{aligned} \quad (3)$$

The prime on the sum over q indicates that only those terms for which $q \neq p$ are included.

It is $I_1(\underline{s})$, representing the intracrystallite contribution to the scattering, which has been included in the Moss and Graczyk calculation as well as other similar analyses and which also forms the basis of most line broadening procedures for determining crystallite sizes. Our intention here is to estimate the importance of the intercrystallite scattering, $I_2(\underline{s})$, relative to $I_1(\underline{s})$, in situations where the crystallites are very small.

III. SIMPLIFICATION OF THE PROBLEM

In order to simplify the problem, we assume that all crystallites have the same number of atoms and the same shape. Since the amorphous materials are isotropic, the crystallites are assumed to take on all orientations with equal probability. Under these circumstances, it is easily demonstrated that $I_1(\underline{s})$ takes the form used by Moss and Graczyk,

$$I_1(\underline{s}) = N \sum_q \underline{f}_q \underline{f}_q^* \sin^2(\pi \underline{s} \cdot \underline{r}_{n_q}) / (\pi \underline{s} \cdot \underline{r}_{n_q}). \quad (4)$$

Here, the summations run over the atoms in one crystallite and \underline{r}_{n_q} is the magnitude of the vector between atoms n and n .

It is $I_2(\underline{s})$ which offers the fundamental difficulty. Let the scattering amplitude for the q -th crystallite, $\underline{F}_q(\underline{s})$, be defined by the relation

$$\underline{F}_q(\underline{s}) = \sum_n \underline{f}_{n_q} \exp[i\underline{s} \cdot (\underline{r}_{n_q} - \underline{r}_Q)] \quad (5)$$

where \underline{r}_Q is the vector to some conveniently chosen origin which is the same in each crystallite. In this work, \underline{r}_Q is the vector to the center atom in each crystallite. Then the expression for $I_2(\underline{s})$ becomes

$$I_2(\mathbf{e}) = \sum_{\mathbf{q}} \sum_{\mathbf{q}'} \bar{V}_{\mathbf{q}}(\mathbf{e}) \bar{V}_{\mathbf{q}'}(\mathbf{e}) \exp [i(\mathbf{e} \cdot (\mathbf{r}_{\mathbf{q}} - \mathbf{r}_{\mathbf{q}'}))]. \quad (6)$$

To obtain a simply calculable expression from Eq. (6), we have made one more simplifying assumption. We assume that there is, on the average, no correlation between the orientations of different crystallites, even if they are adjacent. This, we believe, is the weakest assumption in the paper. Its consequences are discussed below. With this assumption, $I_2(\mathbf{e})$ reduces to

$$I_2(\mathbf{e}) = N |\bar{V}(\mathbf{e})|^2 \int_0^\infty 4\pi r^2 \rho(r) \sin(\mathbf{e}r) / (\mathbf{e}r) dr. \quad (7)$$

Here, $\bar{V}(\mathbf{e})$ is the spherically averaged $V_{\mathbf{q}}(\mathbf{e})$ given by the relation

$$\bar{V}(\mathbf{e}) = \sum_{\mathbf{q}} \frac{V_{\mathbf{q}}(\mathbf{e})}{N} \sin(\mathbf{e}|\mathbf{r}_{\mathbf{q}} - \mathbf{r}_{\mathbf{q}'}|) / (|\mathbf{r}_{\mathbf{q}} - \mathbf{r}_{\mathbf{q}'}|). \quad (8)$$

$4\pi r^2 \rho(r)$ is the relative probability of finding two crystallite centers separated by a distance r . It is normalized such that

$$\int_0^\infty \rho(r) dr = N, \quad (9)$$

where N indicates the sample volume.

IV. NUMERICAL EVALUATION FOR SPECIFIC MODELS

In this section, Eqs. (4) and (7) are evaluated numerically for models close to those chosen by Moss and Graczyk for amorphous Si. Two types of crystallites are chosen for study. The first consists of a central atom plus the first two coordination shells in the diamond lattice, so that each crystallite contains 17 atoms. In the second type, the third coordination shell is added, increasing the number of atoms per crystallite to 29.

Since Nf^2 appears implicitly or explicitly as a factor in Eqs. (4) and (7), it is more convenient to calculate $I_2^f(\mathbf{e}) = I_2(\mathbf{e})/Nf^2$.

Eqs. (4) and (8) are readily evaluated numerically using well-known lattice parameters for Si. All the difficulty in the calculation arises from the unknown $\rho(r)$.

As a first approximation to $\rho(r)$, we have used the "liquid" hard sphere radial distribution function of Finney³. Even with this distribution, however, two difficulties arise.

The first is the Finney's data is given as $\rho(r/r_g)/\rho_g$ where r_g is the average number density and r_g is the sphere radius. The packing fraction, i.e., the fraction of space filled by spheres, was found by Finney to be about 0.43. Since amorphous solids have densities which are typically 90 to 100% of the associated crystalline phase, some adjustment must be made or the magnitude of $I_2(\mathbf{e})$ will be underestimated. This is a further shortcoming of assuming roughly spherical crystallites.

In this calculation the higher densities have been accounted for by calculating the crystallite number density ρ_g from the actual crystallite volume, neglecting the fact that dense packing of spheres is not possible. The choice of r_g is thus also somewhat arbitrary. It can be seen that the Fourier transform of the radial distribution term in Eq. (7) scales in a inversely as r_g^3 causing the location of its maxima to depend on r_g . The effects of this are discussed below.

Another difficulty faced was associated with the finite upper limit on r in which Finney calculated $\rho(r)$. At large r , for an amorphous material, $\rho(r) \sim \rho_g$, the average particle density, while at small r , $\rho(r)$ oscillates about ρ_g . At the largest r at which Finney calculated $\rho(r)$, it is still oscillating, so that an accurate choice of ρ_g is difficult. Difficulties associated with this problem are also discussed below.

V. RESULTS AND CONCLUSIONS

Calculated values of $I_2^f(\mathbf{e})$ for the two and three shell crystallites are shown in Figs. 1 and 2, respectively. In accordance with their normalization, they approach 288 and 841, the square number of atoms per crystallite, respectively, as \mathbf{e} goes to zero. In the region of importance, $\mathbf{e} > 1.5$, where strong peaks appear for the crystalline materials, the $I_2^f(\mathbf{e})$ oscillates between 5 and 30 atomic units.

Figs. 3 and 4 show $I_2(s)$. This function is negative at small s , but rises to an almost constant, completely negligible value for $s \geq 1$. Hence, the model used here indicates that, in the region of experimental interest to Moss and Graczyk¹¹, the intercrystalline interference contribution to the total intensity is negligible.

In light of the discussion about liquid argon contained in the third paragraph of the Introduction, this result seems surprising. Except for one factor, this calculation is almost completely equivalent to the liquid argon case. The radial distribution for hard spheres could cause only minor changes in the magnitude of the scattering, as would the alterations used to achieve the correct density. Hence, if the crystallites had a spherically symmetric electron density we would expect appreciable interference terms out to $s \approx 2.5$. The difference between the two cases arises from the fact that the crystallites do not have a spherically symmetric electron density. This is shown most vividly through an examination of Eqs. (4) and (7) for $I_1(s)$ and $I_2(s)$. Eq. (4) is just the N times the spherical average of the scattered intensity from a single crystallite. For the liquid argon case, it would be N times the square of the liquid argon scattering factor. In Eq. (7), on the other hand, the factor which replaces the square of the atomic scattering factor which normally appears in a radial distribution analysis of the scattered intensity, is $|\bar{F}|^2$, is the square of the spherically averaged scattering factor per crystallite. That is, we are dealing with a situation where the independent scattering deals with the average of a square, whereas in the interference term, it is the square of the average. Since the crystallite atomic arrangement is far from spherically symmetric, the crystallite scattering factor will show, at fixed $|s|$, both positive and negative values with differing orientations of the scattering vector with respect to some crystallite axis, leading to a small spherical average $|\bar{F}|^2$. This effect is illustrated in Figs. 5 and 6, which show $|\bar{F}|^2$ for the two and three shell crystallite models, respectively. Comparing Figs. 2 and 6, we see that $I_1(s)$ oscillates between 6 and 40 near $s = 2$, whereas $|\bar{F}|^2$ has a maximum value of 7 and is usually far below this value throughout the same region. Throughout the region, $|\bar{F}|^2$ is less than 15% of $I_1(s)$. Similar results are obtained for the two shell crystallite.

In the $I_2(s)$ expression there is also the Fourier transform of the radial distribution function appearing as a factor. Our calculation of this factor is presented in Fig. 7 for the three crystallite model. Corresponding to the large crystallite size, the first maximum appears at $e \approx 0.85$ and is not of interest. For the two shell crystallite, it is at $e = 1.0$, and also not of interest. More interesting is the fact that it never rises above 0.1 in magnitude at the e value of interest. It is apparent, therefore, that in $I_2(s)$, there are multiplicative factors of 15% and 10%, leading to a product effect of less than 2%. Thus, small variations in the location of the maxima as determined by the choice of I_0 are not important. Even if the radial distribution used and the other above mentioned problems could cause a factor of 2 error in this estimate, the interparticle interference term cannot be appreciable in the region near $s = 2$.

We return now to the basic assumption of this paper, that there is no correlation in the orientations of the crystallites. It is this absence of correlation which leads to the appearance of $|\bar{F}|^2$ in Eq. (7), and the first 15% effect mentioned just above. It is, therefore, very much responsible for the small values of $I_2(s)$ presented here. The importance of this effect suggests that if just the opposite, that is strong orientational correlations were assumed, the results might be quite different. This role of strong correlations remains a conjecture, however. With the numerical results presented above, we believe that the burden of proof that interparticle interference terms are appreciable rests with those who suggest their importance.

FOOTNOTES

- * This research was supported by the Advanced Research Project Agency of the Department of Defense and was monitored by U.S. Army Research Office-Durham under Contract number DAKC04-70-0044.
- +Portions of this work constitute part of a Ph.D. thesis submitted to Stanford University by Foster Bette.
- ** Present address: The Hospital for Special Surgery, New York, New York 10021.
- ¹S.C. Moss and J. F. Graczyk, *Phys. Rev. Letters*, **23**, 1167 (1969).
- ²D. G. Henshaw, *Phys. Rev.* **105**, 976 (1957).
- ³J. L. Finney, *Proc. Roy. Soc.*, **319A**, 479, 495 (1970). The detailed radial distribution function was supplied by private communication.

FIGURE CAPTIONS

- Fig. 1. $I_1(s)$ versus s for the model silicon crystallite containing two coordination shells.
- Fig. 2. $I_1(s)$ versus s for the model silicon crystallite containing three coordination shells.
- Fig. 3. $I_2(s)$ versus s for the model silicon crystallite containing two coordination shells.
- Fig. 4. $I_2(s)$ versus s for the model silicon crystallite containing three coordination shells.
- Fig. 5. $|\bar{F}|^2$ versus s for the model silicon crystallite containing two coordination shells.
- Fig. 6. $|\bar{F}|^2$ versus s for the model silicon crystallite containing three coordination shells.
- Fig. 7. Radial transform of the Finney pair distribution function appropriate to model silicon crystallite containing three coordination shells.

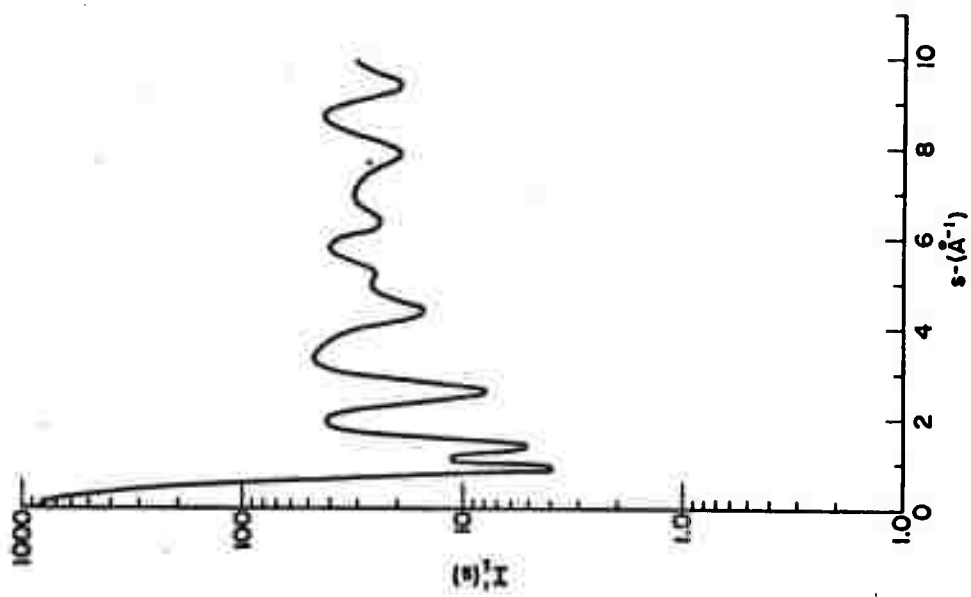


Fig. 1

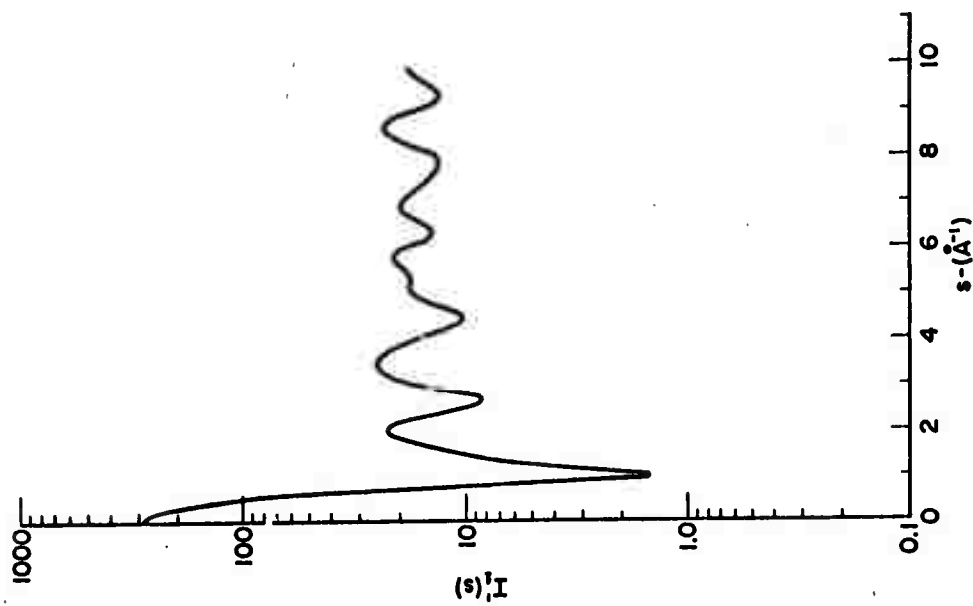


Fig. 2

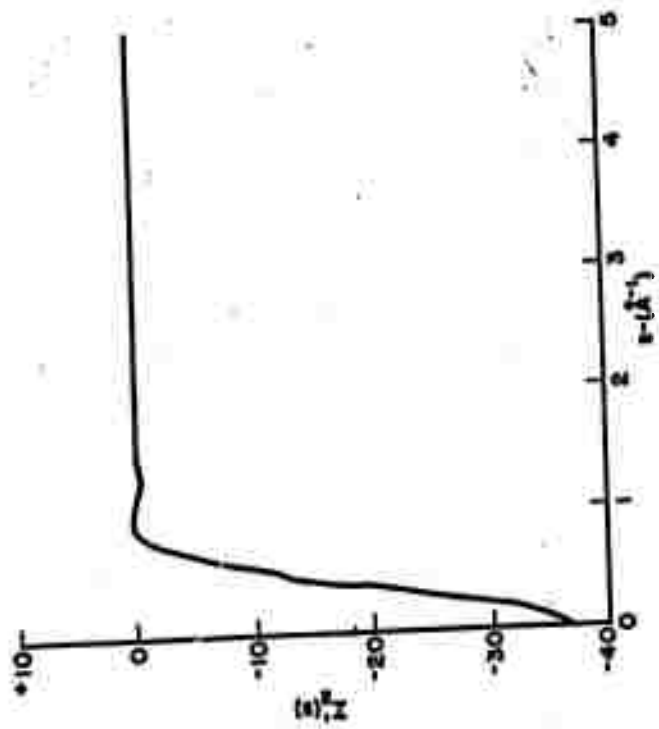
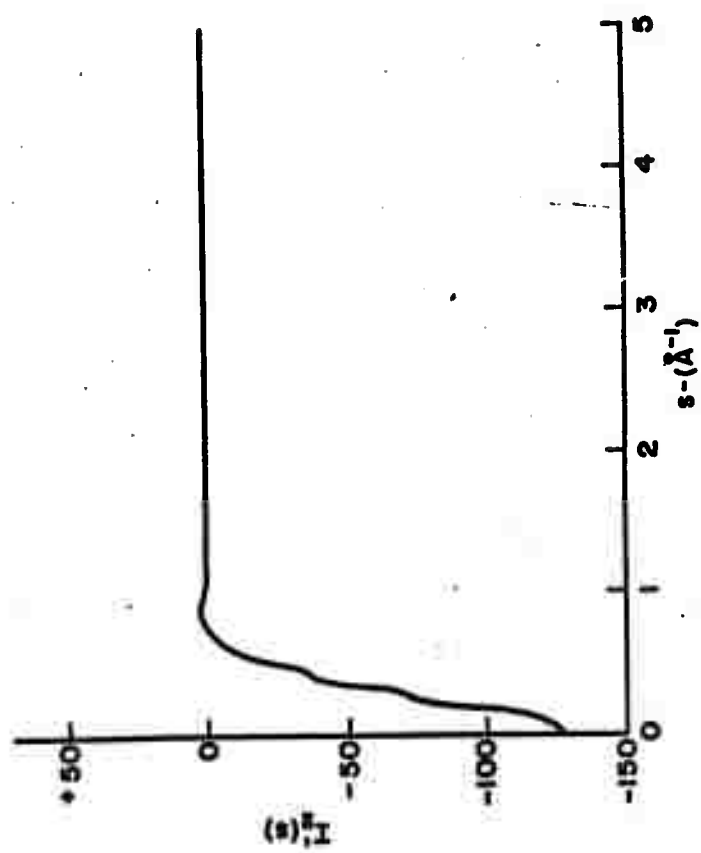


Fig. 3

Fig. 4

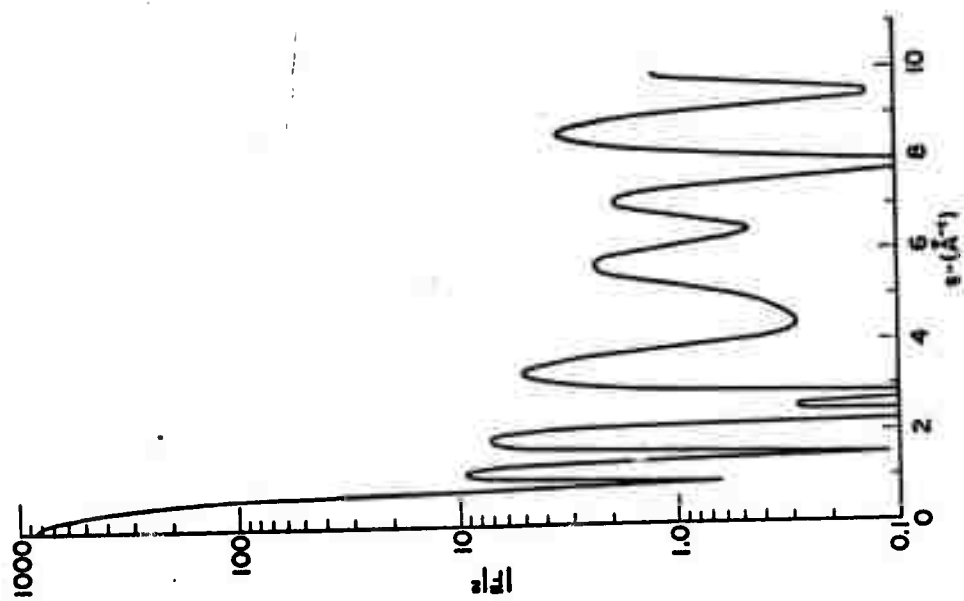


Fig. 5

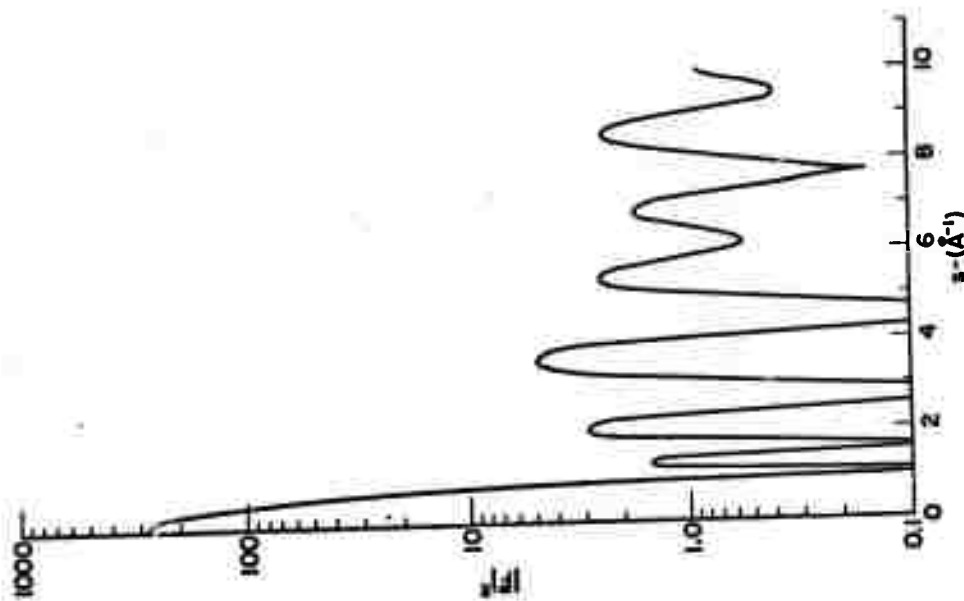


Fig. 6

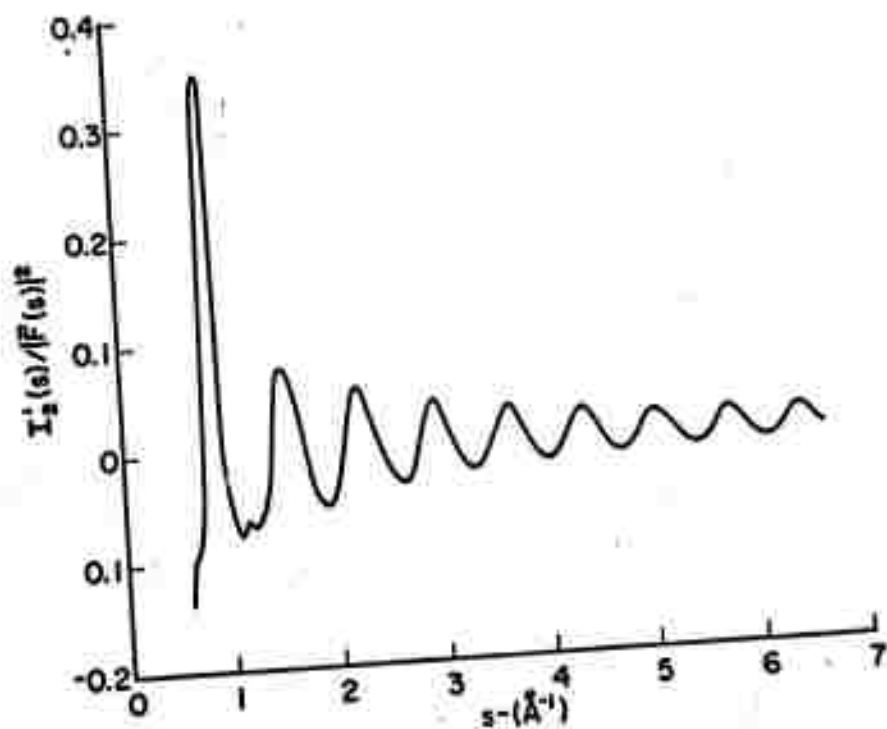


Fig. 1

NEUTRON AND X-RAY DIFFRACTION RADIAL DISTRIBUTION

STUDIES OF AMORPHOUS Ge₁₇Te₈₃^{**}

F. BETTS^{**} and A. BIENENSTOCK

Department of Materials Science and Engineering, Stanford University

Stanford, California 94305

and

D. I. KEATING

Brookhaven National Laboratory, Upton, New York 11973

and

J. deNEUFVILLE

Energy Conversion Devices, Inc., Troy, Michigan 48064

SU-DMS-72-T-4

I. Introduction

Recently, Betts, Bienenstock and Ovshinsky¹ (BBO) presented the results of x-ray diffraction radial distribution studies of $\text{Ge}_x\text{Te}_{1-x}$ alloys with $x=0.11$ and 0.54 . This system is of particular interest because of the memory switching associated with samples of composition near $x=0.15$ and because the amorphous material with composition near $x=0.54$ has a structure which is quite different from that of crystalline GeTe.

As discussed by Keating², it is impossible to determine the coordinations of binary alloys uniquely from a single radial distribution. It is possible, however, to test models on the basis of the areas under the various peaks. It is this procedure which was followed by BBO. The area of the first peak in the $x=0.11$ radial distribution is quite consistent, within experimental error, with a model, denoted the "Dilute x Model" in which the Te chain structure is preserved, but with four-fold coordinated Ge atoms acting as chain crossing points.

The area of the first peak in the $x=0.54$ sample is consistent, within experimental error, with two models. One, based on the idea that each Ge(Te) is surrounded only by Te(Ge) atoms yields a coordination number of 3. On the other hand, the Dilute x Model can be extended to higher x values through the elimination of the above-mentioned restriction, via a model denoted the "Random Covalent Model". In this model, every Ge is fourfold and every Te twofold coordinated. The number of Ge-Ge, Ge-Te and Te-Te pairs is then determined only by these coordination numbers and the composition. This model also gives very good agreement with the areas of the first peaks in the radial distributions for the $x=0.11$ and 0.54 samples.

Abstract

Bulk amorphous samples of amorphous $\text{Ge}_{0.17}\text{Te}_{0.83}$ have been prepared by quenching of small molten droplets. Radial distribution functions have been constructed from both x-ray and neutron diffraction intensity data. These indicate first neighbor peaks at 2.75\AA and 2.65\AA , respectively, indicating the greater sensitivity of the neutron RDF to atoms pairs containing the smaller Ge atom. The first peak area in both RDF's is not consistent with twofold coordination of the Ge. It can be fit by two types of models. In the first, the Ge is fourfold and the Te twofold coordinated. In the second, the Ge is threefold coordinated, while some Te are threefold and others twofold coordinated. It is shown that both types of models are consistent with RDF's performed on other compositions.

In both the "Dilute x" and "Random Covalent" models, the essential feature is that the Ge and Te are fourfold and twofold coordinated, respectively. For alloys dilute in Ge, they differ only in the amount of short-range chemical ordering assumed. It is extremely difficult to distinguish between them in the Ge-Te system through neutron and x-ray RDF studies, since the first neighbor peak areas are quite insensitive to this ordering.

Both models are, however, quite different from that proposed by Hilton et al.³ for the coordination of Ge in various Ge-Te-X glasses. Here, X is a group V element. These authors suggest that both the Ga and Te coordinations are twofold in these systems, on the basis of calculations performed to interpret their infrared absorption studies. Since their method of coordination determination is rather indirect, it was viewed by BBO, in an earlier paper⁴, as ambiguous.

In reality, however, the BBO x-ray diffraction radial distribution determination of the Ge coordination in the x=0.11 sample is also ambiguous for reasons not discussed above. The first is that there may be phase separation, with the radial distribution averaging over the coordinations in the two phases. This problem is discussed below. In addition, however, there is the problem that the Ge x-ray scattering factor is only 60% of that for Te. When this low scattering factor is coupled with the small x value, it is found that the area of the first neighbor peak has only a small contribution from atom-pairs which include Ge. As a result, models based on other Ge coordinations also yield peak areas consistent with experiment. It is this problem which is dealt with in the experiments described here.

In this paper, radial distribution functions (RDF's) obtained by both x-ray and neutron diffraction from a sample with x=0.17 are presented. The larger x, relative to the previously studied sample with x=0.11, leads to an increase in the proportion of atom pairs which include Ge in the first peak area. In addition, the neutron scattering length, b, for Ge is about 50% larger than that for Te. As a result, the contribution of Ge to the first peak area is considerably enhanced, relative to the x-ray case. Thus, the neutron diffraction RDF provides a considerably more sensitive check of any model of Ge coordination than does the x-ray RDF. This sensitivity, it is shown, is sufficient to eliminate the possibility that the Ge coordination is twofold. On the other hand, models based on threefold Ge coordination are introduced. These models are as capable as the fourfold Ge coordination models of predicting the first neighbor peak areas in all the x-ray and neutron RDF's obtained thus far. Hence, the interpretation of the RDF's is ambiguous. Attempts to resolve this ambiguity on the basis of other data are presented.

Finally, it should be pointed out that it became possible to perform neutron diffraction studies on these materials only when a technique was developed for making sufficiently large quantities of the amorphous material. This technique is described immediately below.

II Experimental

A. Sample Preparation

To prepare a homogeneous 200g sample of glassy $\text{Ge}_{.17}\text{Te}_{.23}$, the splat cooling technique which had been successfully used by Luo and Duwez⁵ to prepare milligram-sized glassy samples was clearly inadequate. We therefore utilized a somewhat analogous technique termed "spray cooling" which had been previously developed at Energy Conversion Devices for preparation of glassy chalcogenide balls. This technique is suitable for preparing glassy samples of certain chalcogenide compositions which cannot be quenched to the glassy state by conventional quenching of sealed ampoules in water or brine. In essence the liquid is held under an argon atmosphere at a temperature (650°C in this case) which is sufficient to thoroughly homogenize, but insufficient to substantially vaporize, the sample. Following homogenization, the liquid is subjected to a slight differential pressure which forces it to flow through a ~100 μm orifice in the bottom of its fused silica container. The fine stream of liquid thus produced is directed through argon gas into a swirling silicone oil bath held between 25 - 100°C (50°C in this case). The temperature of the bath controls the oil viscosity, so that variation of the pressure differential, the stirring velocity, and the oil bath temperature result in variations in the diameters of the glassy spheroids obtained. In the present study the spheres obtained ranged between 150 - 300 μm in diameter.

The standard spray cooling apparatus was easily modified to fabricate the large glass sample required in this study. A larger heating coil and fused quartz container were substituted for the standard sample holder and the sample was prepared by batch feeding crystalline chunks of the

alloy into the sample holder, melting, homogenizing, spraying and refilling until the desired quantity of glassy material was obtained.

A typical sampling of these balls revealed no crystallites when viewed with high resolution reflection optical microscopy. A few larger (up to 1 mm) balls did contain a very small volume fraction of crystallites, whose presence was clearly observable due to a large increase in reflectivity upon crystallization. Feinleib and Ovshinsky⁶ have measured a ~50% increase in reflectivity accompanying the crystallization of similar materials. We felt that optical verification of the absence of crystallization in our sample is substantially more sensitive than the usual direct diffraction measurements; a 0.1% volume fraction of crystallites would be readily apparent by our techniques.

Prior to the performance of the diffraction experiments, the surface layer of silicone oil was removed by washing in trichloroethylene. The density of the material was determined as $5.53 \pm 0.03 \text{ gm/cm}^3$ by the Archimedian method, using tetrabromoethane as the buoyant medium.

II B. Neutron Diffraction

As indicated above, the samples for neutron diffraction was made in the form of spheres with diameters of the order of a few tenths of a millimeter. The smallest of these were selected to fill a rectangular parallelepiped vanadium container whose interior depth was 0.833 cm, and symmetrical transmission geometry was used in the experiment.

The diffraction experiment was performed at the Brookhaven National Laboratory High Flux Beam Reactor. The incident beam was monochromatized and had a wavelength of 1.0285 Å. No diffracted beam monochromator was employed. Hence, in the analysis which follows, all scattering has been treated as quasielastic where, at each scattering angle, all energies are accepted. This would be identical to the x-ray case if momentum transfer could be ignored. The scattered intensity data, collected in transmission, were obtained by step scanning in angular increments of 0.5° ($2-\theta$) from 2.0° to 93.0° , using fixed times. A minimum of 4900 counts were collected at each point. The complete measurement was performed twice to determine reproducibility, which was that anticipated from statistical fluctuations.

The measured intensities were corrected for background, absorption, air scattering and scattering from the container. In addition, a multiple scattering correction was performed using the Vincyard⁷ approximation appropriate for the geometry employed. Finally, the data were put on an absolute scale through comparison with the scattering from a vanadium slab. The scaled intensities, including multiple scattering, are presented in Fig. 1.

Transformation of the data to obtain the radial distribution was performed in the normal fashion, as described in(SBO)for the x-ray case,

with a value of 0.014 for 'a' in the arbitrary temperature factor, $\exp(-as^2)$. This 'a' value was chosen to make the value of $4\pi R^2 p(r)$ equal to zero at the minimum at 3.15 Å.

III The Radial Distributions

The neutron and x-ray diffraction radial distribution functions

(RDF's) so obtained are shown in Figs. 3 and 4, respectively. The general features of these RDF's are similar to those presented by BBO on similar materials. That is, both show peaks near 2.7 and 4.1 Å. It is interesting, though, to note the differences in the nearest neighbor distances for the two types of RDF's. The neutron diffraction distribution shows the first neighbor peak at 2.65 Å while in the x-ray diffraction case it is at 2.75 Å. We interpret this as being due to the heavier contribution of pairs which include Ge atoms in the neutron case. Such pairs would have shorter interatomic distances than pairs dominated by the Te atoms.

The most interesting new result of the experiments is the area under the first neighbor peak of the neutron diffraction radial distribution. Because of the factors mentioned above, this peak is almost perfectly resolved and should, therefore, yield an extremely accurate area. That area is 0.912 ± 0.05 barns. The x-ray peak is less well resolved and yields an area of 5020 ± 500 electrons².

The greater resolution of the neutron diffraction RDF is somewhat unexpected since the x-ray intensity data extend to higher s values than do the neutron data. In addition, a slightly larger temperature factor is used in transforming the neutron data than is used with the x-ray data. Both effects would tend to make the resolution in the x-ray RDF greater than that in the neutron RDF.

It is possible that this increased resolution comes through a judicious choice of the arbitrary temperature factor in the transformation

11

II C. X-ray Diffraction

X-ray diffraction patterns from this sample were obtained using Zirconium filtered MoK_α radiation on a Picker diffractometer using a NEC Solid-state detector with a pulse-height analyzer window from 15 to 19 KeV. Although the potential resolution of the system is less than 1 KeV, the wide window was chosen so that Compton scattering, as well as the K_α radiation, was accepted. This was done because the pulse-height analyzer could not eliminate the small-energy-loss Compton scattering. It appeared best to accept all of the Compton scattering and correct for it in the data analysis, rather than accepting only the small-angle portion and then attempting to estimate the contribution in the angular region where this scattering is only partially accepted by the analyzer. The intensity data were obtained by scanning continuously at $1/8^\circ$ ($2-\theta$) per second and recording the integrated counts for every 100 second interval. The minimum number of counts per interval recorded was about 10^4 . Measurements were made over the angular range 4° to 145° ($2-\theta$), corresponding to a range in $s(4\pi \sin\theta/\lambda)$ of 0.62 to 16.85. At the lower angles of observation, the intensity had reached a constant value. This constant value was extrapolated to zero angle in the calculation of the Fourier transformation used to determine the radial distribution function. The resulting intensities are presented in Fig. 2.

Transformation of the data was performed exactly as described in BBO, with a value of 0.01 for 'a' in the arbitrary temperature factor, $\exp(-as^2)$.

10

of the neutron data. If these errors were important, however, one would anticipate appreciable ripples at small r values. These are not observed in either RDF, indicating that series termination errors are small.

Another possibility is that these RDF's are showing an inherently greater resolution of neutron RDF's in polyatomic systems. Since the neutrons are scattered by the nuclei, there is essentially point scattering and the scattering amplitudes do not vary with angle. To make the x-ray scattering simulate that from point scatterers, the coherent portion of the scattered intensity is divided by the square of an effective mean scattering factor per electron. In a monoatomic amorphous sample this procedure should make the x-ray and neutron resolutions identical if the x-ray atomic scattering factor is correctly determined. In polyatomic systems, however, the individual atomic scattering factors have different shapes. The effective mean x-ray scattering factors do not, therefore, exactly represent the shapes of the individual atomic scattering factors. Consequently, the resulting simulated 'point' scattering electron densities have, in general, both finite widths and ripples around their main peaks. These widths and ripples lead to limitations on the ultimate resolution and quality of the x-ray RDF's.

IV Coordination Models

As mentioned in the Introduction, it is impossible to determine the coordination of amorphous binary alloys uniquely from a single radial distribution. In fact, Keating² has shown that three independent distributions are required. Since we do not have three such distributions, this section is concerned with the development of possible models for the coordination and the first neighbor peaks areas to be expected from them. Attention is focussed on the first neighbor peaks because of the complexity of the models and the lack of guidance from the crystalline phases.

We begin with models based on the coordination scheme proposed by Hilton et al.³

IV A. Models Based on Twofold Coordination of Ge

In this and the sections which follow, physical models for possible coordinations and equations for the area under the first neighbor RDF peak are presented. The derivations of these equations are presented in the Appendix.

Dilute x Chain Model

In the Dilute x Chain model, it is assumed that all atoms are twofold coordinated and that every Ge is surrounded by two Te atoms. The resulting area is

$$A_{2d} = 2N[2xz_{Ge}z_{Te} + (1-2x)z_{Te}^2] \quad (1)$$

Here, N is the total number of atoms in the sample while Z is the atomic number for the x-ray RDF and the scattering length, b, for the neutron RDF.

Random Covalent Chain Model

In the Random Covalent Chain model, it is assumed that each atom is twofold coordinated, but that there is no chemical ordering. The resulting area is

$$A_{2r} = 2N[x^2z_{Ge}^2 + 2x(1-x)z_{Ge}z_{Te} + (1-x)^2z_{Te}^2] \quad (2)$$

IV B. Models Based on Threefold Coordination of Ge

Dilute x Threefold Coordinated Model

In this model, it is assumed that every Ge is surrounded by 3 Te atoms. For every Ge, there is also a Te coordinated by one Ge and two Te atoms. In addition, for every Ge, there are two Te's bonded to one Ge and one Te. Each of the remaining Te's are bonded to two Te's. This system has an upper limit of $x=0.17$. The resulting area is

$$A_{3d} = 2N[3xz_{Ge}^2z_{Te} + (1-2x)z_{Te}^2] \quad (3)$$

Phase Separated Threefold Coordinated Model

In this model, it is assumed that these alloys are phase separated into regions of threefold coordinated amorphous GeTe and regions of amorphous Te. The amorphous Te is assumed to have twofold coordination. The resulting area is

$$A_{3p} = 2N[3xz_{Ge}^2z_{Te} + (1-2x)z_{Te}^2] \quad (4)$$

It should be noted that $A_{3p} = A_{3d}$.

IV C. Models Based on Fourfold Coordination of Ge

Dilute x Fourfold Coordinated Model

In this model, presented previously by BBO, every Ge is surrounded by 4 Te's, so that there are no Ge-Ge nearest neighbors. The upper Ge concentration limit for such a model is $x=1/3$. The equation of BBO for this model is incorrect. It should read

$$A_{4d} = 2N[4xZ_{Ge}^2Z_{Te} + (1-3x)Z_{Te}^2]. \quad (5)$$

Random Covalent Fourfold Coordinated Model

Here, it is assumed by BBO that every Ge is fourfold and every Te is twofold coordinated. No chemical ordering is assumed, however, so that the number of Ge-Ge, Ge-Te and Te-Te pairs is determined only by the coordination numbers and the sample composition. The resulting area is

$$A_{4r} = 2N[2x^2Z_{Ge}^2 + (1-x)^2Z_{Te}^2 + 3x(1-x)Z_{Ge}Z_{Te}]. \quad (6)$$

Phase Separated Fourfold Coordinated Model

In this model, it is assumed that the system is phase separated into a GeTe_2 glass, with coordination like that in vitreous SiO_2 , plus amorphous Te. The area is

$$A_{4p} = 2N[4xZ_{Ge}^2Z_{Te} + (1-3x)Z_{Te}^2]. \quad (7)$$

It should be noted that $A_{4p} = A_{4d}$. It should also be noted that this model is applicable up to $x=0.33$.

V Conclusions

The major success of this work is to eliminate the possibility of Ge twofold coordination from consideration. That the neutron diffraction studies were necessary for this elimination is shown in Figs. 5 and 6 which present calculations of the first neighbor peak areas as a function of composition for the x-ray and neutron cases, respectively, in the region $0 < x < 0.5$. Also shown on these curves are various experimental determinations of the peak areas. For the $x=0.17$ sample, in the neutron diffraction case, the measured area of 0.91 agrees exactly with that predicted by the Random Covalent Fourfold Coordinated model, and deviates by less than 3% from the predictions of the Dilute x Fourfold Coordinated and Dilute x Threefold Coordinated models. On the other hand, it differs by over 20% with both of the twofold coordinated models. The calculated areas for all the models are, however, in agreement with the measured x-ray RDF area.

The x-ray studies on samples with $x=0.38^8$ and $x=0.5^1$ also disagree with the twofold coordinated models. Here, the increase in Ge concentration allows for a clear differentiation between twofold and other coordination forms.

The calculations presented in Sec. IV and on Figs. 5 and 6 show the insufficiencies of such studies, taken in isolation, for more detailed analysis of the nearest neighbor coordination. The equalities $A_{3p} = A_{3d}$ and $A_{4p} = A_{4d}$ demonstrate that the first neighbor peak areas are quite insufficient for determining whether the system is phase separated. This is an essential ambiguity associated with the radial distributions and implies that the question of the existence of phase separation must be answered by

other techniques. One might argue that more detailed analysis of the higher-order neighbor peaks might resolve the difficulties. We have found, however, that ambiguities associated with possible second neighbor coordinations, resulting partially from the absence of appropriate guiding crystalline structures, remove this possibility as well.

In spite of the ambiguous RDF's, we do not believe that the samples are phase separated in the region $0.1 < x < 0.33$. DeNeufville⁹ has found that the glass transition temperature rises sharply with increasing x in this region. This is in contrast to the normal plateau in T_g versus composition found in phase separated composition regions. In addition, Chaudhari and Hurd¹⁰ have not found such separation in samples of $\text{Ge}_{0.15}\text{Te}_{0.85}$ on any scale greater than 20\AA in their transmission electron microscopy studies on both as-deposited and heat treated samples.

The insensitivity of RDF's to phase separation is not an unknown phenomenon. Less apparent to us at the initiation of this research was the insensitivity of the first neighbor peak areas to the basic Ge coordination. This is demonstrated most convincingly in Fig. 5, which shows that the deviation between A_{3d} and A_{4r} is so small over the entire composition range that it could not be detected with any x-ray experiment. The maximum difference is 2.5%, which is well within the uncertainties in areas determined from the best x-ray RDF work. In the neutron case, as shown in Fig. 6, the difference is less than 3% at $x=0.17$, but rises to 10.8% at $x=0.5$. Thus, for samples which might now be prepared in the bulk form necessary for the neutron studies, $0.15 \leq x \leq 0.25$, the peak area is not sufficient for distinguishing between the two models. Sufficient accuracy for distinguishing could be obtained at $x=0.5$, but it is not apparent that sufficiently thick samples could be prepared. Thus, we are forced to

conclude that the RDF studies performed thus far on the $\text{Ge}_x\text{Te}_{1-x}$ system, as well as those which might be performed readily, are unlikely to distinguish between threefold and fourfold Ge coordination.

Here, again, the thermal studies of DeNeufville⁹ offer some guidance. He finds that T_g for a sample with $x=0.38$ is considerably lower than that for $x=0.33$. This result implies that the amorphous GeTe_2 is the most stable structure in this composition region. We conclude, tentatively, from this result that amorphous GeTe_2 has a structure related to amorphous SiO_2 , with fourfold coordination of the Ge and twofold of the Te. This result, coupled with the thermal results described just above, leads us to conclude that the Ge is fourfold coordinated for $x < 0.33$ and that the Dilute x Fourfold Coordinated model is more appropriate than the Random Covalent Fourfold Coordinated model, since the ideality of GeTe_2 implies a preference for Ge-Te bonds over Ge-Ge and Te-Te bonds.

For $x > 0.33$, it is difficult to say anything definitive. The calculations presented here show that any mixture of three and fourfold coordinated Ge could fit the radial distribution. Each of these coordinations has features which are attractive. The fourfold coordination model allows for a simple satisfaction of the 8-N rule and, therefore, a simple covalent bonding picture. The threefold coordination, on the other hand, is consistent with the fact that crystalline GeTe is very similar in its structure and bonding to crystalline As and Sb, which appear to have threefold coordination in their amorphous forms.

Finally, we draw attention to the maximum at $s=1.065\text{\AA}^{-1}$ which shows up so clearly in the neutron diffraction intensity data. This corresponds to a d-spacing of approximately 5.9\AA . The close relationship between this

Acknowledgements

The authors are pleased to acknowledge many helpful discussions with and critical readings of manuscript drafts by Simon Moss, aid in the performance of the neutron diffraction experiments by many members of the Brookhaven High Flux Beam Reactor staff, aid in the x-ray diffraction experiment from George Martin and Marta de Rojas, aid in the sample preparation by Donald Sarrach, and aid in the computations by Patricia Moll.

number and the spacing of the forbidden (001) reflection of Te might lead one to suspect that the maximum is due to the maintenance of chain ordering in the amorphous material. We doubt this for two reasons. First, it is not apparent why a forbidden reflection should become strong in the amorphous case, since the basic chain ordering which makes the reflection forbidden in the crystalline case would also lead to a weak intensity in the amorphous case. Second, the peak is stronger in the neutron than in the x-ray scattering curves. This would suggest that it is due to the presence of the Ge.

Footnotes

- * This research was supported in part by the Advanced Research Projects Agency of the Department of Defense and was monitored by U. S. Army Research Office-Durham under Contract number DAHCO4-70-C-0044 and by the Advanced Research Projects Agency through the Center for Materials Research at Stanford University and through Contract DAHCO4-70-C-0187 with Energy Conversion Devices, Inc., as well as by the U. S. Atomic Energy Commission.
- + Portions of this work constitute part of a Ph.D. thesis submitted to Stanford University by FB.
- ** Present Address: The Hospital for Special Surgery, New York, New York 10021.
- 1) F. Betts, A. Bienenstock and S. R. Ovshinsky, J. Non-Crystalline Solids 4, 554 (1970).
 - 2) D. T. Keating, J. Appl. Phys. 34, 923 (1963).
 - 3) A. R. Hilton, C. E. Jones, R. D. Dobrott, H. M. Klein, A. M. Bryant and T. D. George, Phys. Chem. Classes 4, 116 (1966).
 - 4) A. Bienenstock, F. Betts and S. R. Ovshinsky, J. Non-Crystalline Solids 2, 347 (1970).
 - 5) H. L. Luo and P. Duwez, Appl. Phys. Letters 2, 21 (1963).
 - 6) J. Feinlieb and S. R. Ovshinsky, J. Non-Crystalline Solids 4, 564 (1970).
 - 7) C. H. Vineyard, Phys. Rev. 96, 93 (1954).
 - 8) F. Betts, Ph.D. thesis, Stanford University, 1971.
 - 9) J. deNeufville, talk presented at the Fourth International Conference On Amorphous and Liquid Semiconductors, Ann Arbor, 1971.
 - 10) P. Chaudhari and S. R. Herd, *ibid.*

Appendix

In this appendix, Eqs. (1) through (7) are derived. Here, N is the total number of atoms in the sample, N_x is the number of Ce atoms and $N(1-x)$ is the number of Te atoms. In each case, the area contains a factor of 2 which comes from the fact that each pair of atoms, denoted A-B, contributes $2Z_{AB}$ to the area.

Dilute x Chain Model

Since a chain is considered, there are N pairs. Since each Ce is surrounded by 2 Te atoms, there are $2xN$ Ce-Te pairs. All other pairs are Te-Te, so that the number of such pairs is $N(1-x)$. Hence, Eq. (1) is obtained.

Random Covalent Chain Model

Again, it is assumed that each atom is twofold coordinated, but that there is no chemical ordering. Hence, the number of Ce-Ce pairs is Nx^2 and the number of Te-Te pairs is $N(1-x)^2$. This leaves $2x(1-x)$ Ce-Te pairs. Hence, Eq. (2) is obtained.

Dilute x Threefold Coordinated Model

In this model, it is assumed that every Ce is surrounded by 3 Te atoms. In order to keep track of the Te coordination, we have found it useful to consider a charge transfer mechanism which rationalizes the Ce coordination. We consider the covalent bonding starting with an ionized Ce which has gone from a, say, s^2p^2 to an s^2p^3 configuration. This means that one of its Te neighbors, denoted Te^+ , has gone from an s^4p^4 to an s^3p^3 configuration. In this case, the Ce and the Te^+ ions would be expected to have three nearest neighbors in keeping with the 8-N rule.

Since the system is dilute in Ce, it is assumed that each Te^+ is surrounded

by one Ge and two Te atoms. This sets an upper limit of $x=0.17$ on the model. From the picture presented thus far, it is apparent that there must be Nx Ge atoms and $Nx \text{ Te}^+$ atoms. To maintain charge neutrality and the coordination in these alloys, there must also be $2Nx$ atoms denoted Te^* which are coordinated by one Ge and one Te. Finally, there are $(1-4x)N$ Te atoms which are coordinated by 2 Te's. These numbers lead to Eq. (3).

Phase Separated Threefold Coordinated Model

Here, the system is assumed to be separated into threefold coordinated GeTe plus twofold coordinated Te. Writing $\text{Ge}_x\text{Te}_{1-x}$ as $(\text{GeTe})_x\text{Te}_{1-2x}$, we see that there are $3Nx$ Ge-Te pairs and $(1-2x)N$ Te-Te pairs, leading to Eq. (4).

Dilute x Fourfold Coordinated Model

In this model, it is assumed that every Ge is surrounded by 4 Te atoms, and every Te is surrounded by 2 atoms. The total number of nearest neighbor pairs, N_p , can be evaluated by summing the number of pairs contributed by the Ge atoms, $4Nx$, and the number of pairs contributed by the Te atoms, $2N(1-x)$, and then dividing by 2 because each pair has been counted twice in the sum. Hence, we find

$$N_p = N[4x + 2(1-x)]/2 = N(1+x). \quad (\text{A.1})$$

The number of Ge-Te nearest neighbor pairs is $4Nx$ since, in this model, every Ge is surrounded by 4 Te's. The number of Te-Te pairs is then given by $N_p - 4Nx = N(1-3x)$, since there are no Ge-Ge pairs. This leads to Eq. (5).

Random Covalent Fourfold Coordinated Model

The numbers of pairs for this model have been listed by BBO.

Phase Separated Fourfold Coordinated Model

In this model, it is assumed that the system is phase separated into a GeTe_2 glass, with coordination like that in vitreous SiO_2 , plus amorphous Te. In that case, $\text{Ge}_x\text{Te}_{1-x}$ becomes $(\text{GeTe}_2)_x\text{Te}_{1-3x}$. To find the total number of Ge-Te pairs, we double count and then divide by 2. First, each Ge is surrounded by 4 Te's. This leads to $4xN$ pairs. Then, each of the $2xN$ Te atoms in the GeTe_2 is surrounded by 2 Ge atoms, leading to $4xN$ pairs, so that the total number of Ge-Te pairs is $4xN$. Each of the Te atoms in the pure Te region contributes one Te-Te pairs leading to $(1-3x)$ such pairs. These numbers lead to Eq. (7).

Figure Captions

- Fig. 1. Scaled neutron diffraction intensity, as a function of $s(-4\pi\sin\theta/\lambda)$, from $\text{Ge}_{.17}\text{Te}_{.83}$ after corrections for background, absorption and air scattering. The lower horizontal line shows the calculated multiple scattering correction while the upper horizontal line shows the total independent scattering, including the multiple scattering correction.
- Fig. 2. Scaled x-ray diffraction intensity, as a function of $s(-4\pi\sin\theta/\lambda)$, from $\text{Ge}_{.17}\text{Te}_{.83}$. The dashed curve shows the total independent scattering.
- Fig. 3. Neutron diffraction radial distribution function for $\text{Ge}_{.17}\text{Te}_{.83}$.
- Fig. 4. X-ray diffraction radial distribution function for $\text{Ge}_{.17}\text{Te}_{.83}$.
- Fig. 5. Calculated and observed areas of the first neighbor x-ray diffraction radial distribution peaks for the $\text{Ge}_x\text{Te}_{1-x}$ composition range $0 \leq x \leq 0.5$. Curves represent calculated values, while the points and vertical lines represent measured areas with estimated uncertainties.
- Fig. 6. Calculated and observed areas of the first neighbor neutron diffraction radial distribution peaks for the $\text{Ge}_x\text{Te}_{1-x}$ composition range $0 \leq x \leq 0.5$.

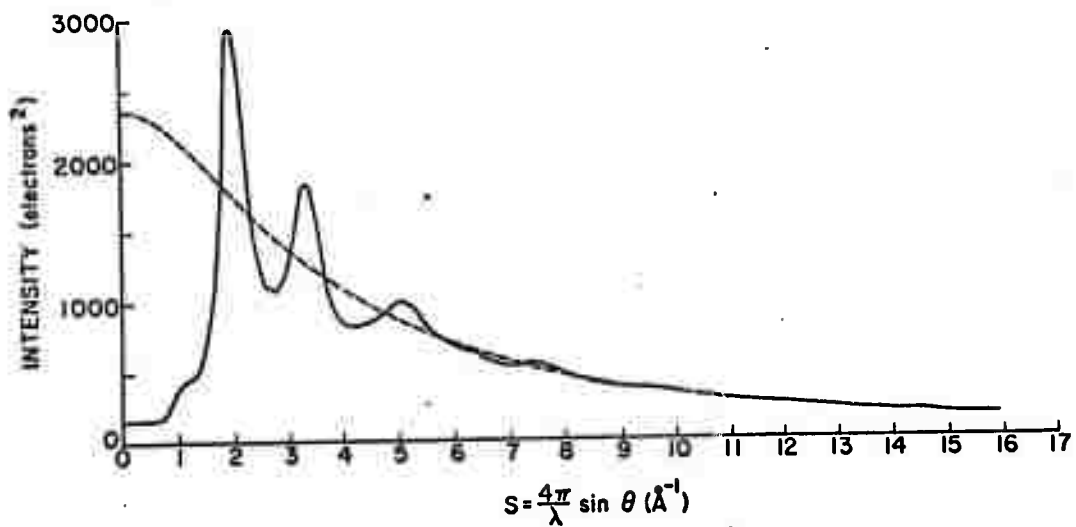


Fig 2

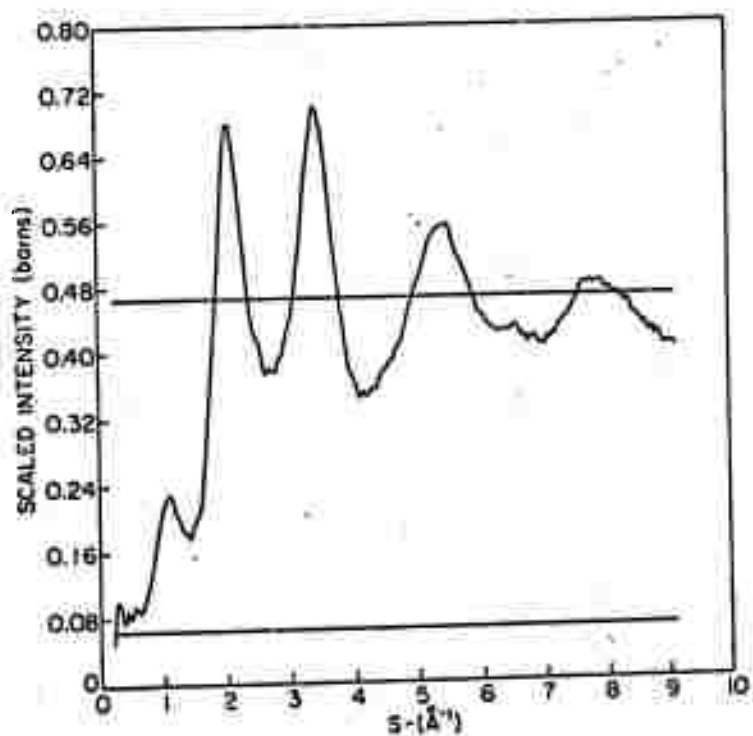


Fig 1

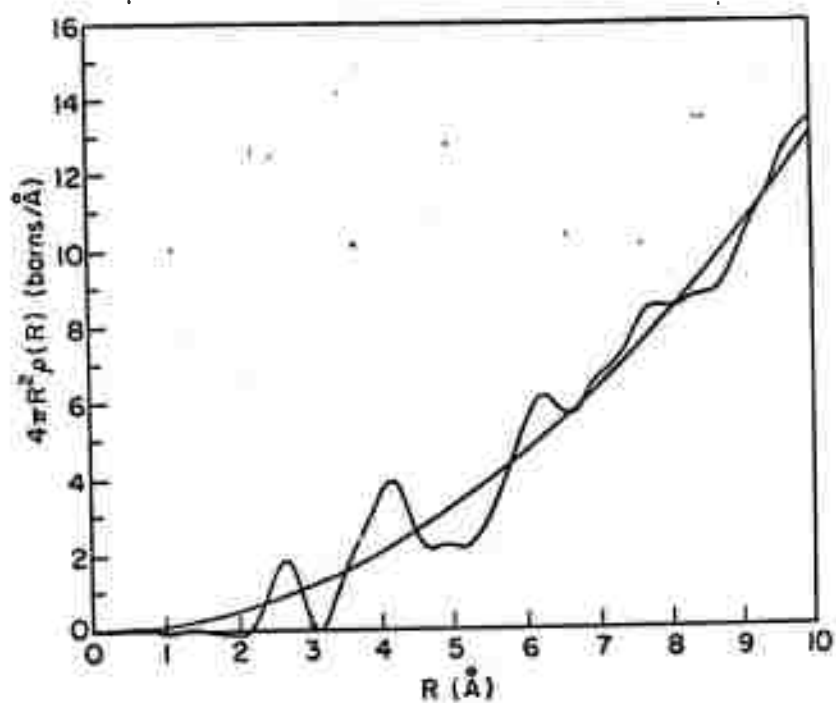


Fig 3

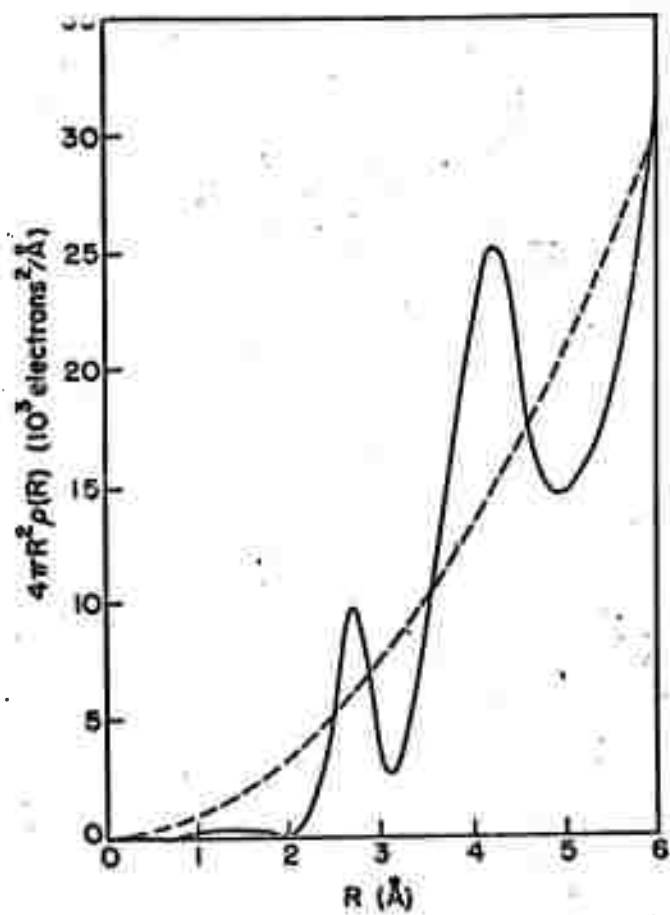


Fig 4

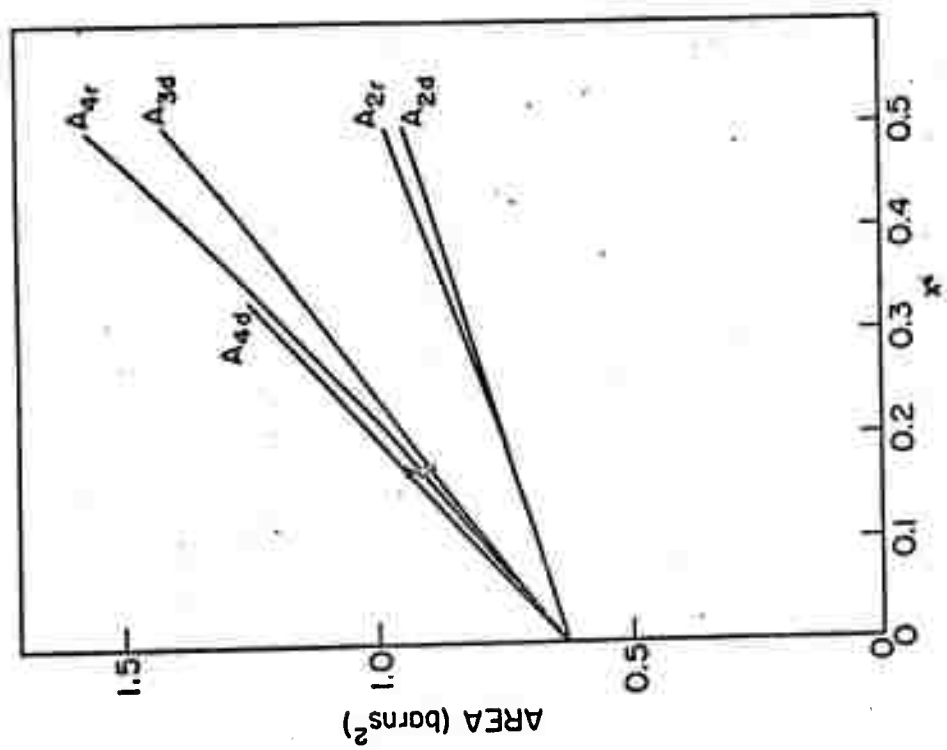


Fig 5

STRUCTURE AND BONDING IN AMORPHOUS $\text{Ge}_x\text{Te}_{1-x}$ ALLOYS^{1,2}

P. BETTS^{1,2} and A. FLEENSTOCK

Department of Materials Science, Stanford University, Stanford, California
94305, U.S.A.

and

C. W. BATES, JR.

Varian Associates, Inc., Palo Alto, California 94303, U.S.A.

X-ray radial distribution studies of the system $\text{Ge}_x\text{Te}_{1-x}$ have been interpreted in terms of a "random covalent" structural model. To further elucidate the structure and bonding type, x-ray absorption edge and x-ray photoemission studies were undertaken. Measured edge and photoemitted electron energies are consistent with covalent bonding. For $x = .15$ to $.57$, the Ge K_{α} edge and the Ge $3d^{5/2}$ photoemitted electron energies of the amorphous materials are close to those of crystalline Ge. For crystalline GeTe, GeSe and GeS, there are 2 to 3 eV shifts indicative of more ionic bonding. These results imply that the amorphous materials are considerably more covalent than any of the crystalline Ge-chalcogenide phases and suggest that none of the crystalline structures can form the basis for a microcrystalline picture of amorphous GeTe.

1. Introduction

Recent radial distribution (RDF) studies¹⁻³ have shown that nearest neighbor distances in amorphous $\text{Ge}_x\text{Te}_{1-x}$ alloys are considerably shorter than in crystalline GeTe, even with $x=0.5$. These distances have been interpreted as indicating covalent bonding, in keeping with the Rott⁴ - Cohen, Fritzsche and Ovshinsky⁵ structural model and, for $x=0.5$, the failure of a microcrystalline model. The first conclusion is, however, reached by inference from the interatomic distances while the second is ambiguous² because of the possibility of the RDF being interpreted as indicating a strained microcrystalline GeS type structure.

In this work, the covalent bonding is demonstrated more directly and the possibility of a microcrystalline model is virtually eliminated. The techniques employed for this demonstration are x-ray induced photoemission (ESCA) and x-ray absorption edge spectroscopy. In both of these techniques, one observes the shifts in energy of core states. In general, these shifts increase with increasing net charge of the ion whose core is studied. Hence, they offer a clue to relative states of ionization.

2. Experimental

The polycrystalline samples of GeS, GeSe and GeTe were prepared by maintaining stoichiometric mixtures of the elemental materials well above the compound melting temperatures in a rocking furnace for an extended period and then cooling slowly. The completeness of the reaction was checked by x-ray diffraction.

The amorphous $\text{Ge}_x\text{Te}_{1-x}$ alloys were sputtered thin films supplied by Energy Conversion Devices, Inc. Their compositions were determined by

$$E_b = E_{x\text{-ray}} - E_{\text{kin}} - \phi_{\text{sp}} - \phi$$

where ϕ_{sp} and ϕ are the work function of the spectrometer and the potential of the sample due to charging, respectively. These authors also show that uncertainties in the comparison of core level energies in different samples due to the existence of ϕ can be eliminated by measuring energy shifts relative to such shifts for carbon in equilibrium with the sample. It is this procedure which has been followed here. Hence, in Table 1 are presented the shifts from the elemental values of core level binding energies in the samples studied. In this table, a positive shift indicates an increase in E_b .

Of most significance in the table are the shifts of the $\text{Ce } 3d^{5/2}$ level, which can be summarized as follows:

- 1) The binding energy shifts approximately 1 eV deeper in all the amorphous samples. The shift does not vary significantly with composition of the samples.
- 2) The shifts in the crystalline materials are significantly larger, ranging from 1.9 eV in GeS to 3.6 eV in crystalline GeTe .
- 3) The change in shift upon crystallization of the $\text{Ge}_{.15}\text{Te}_{.81}\text{As}_{.02}\text{S}_{.02}$ sample is approximately 2 eV.

We interpret these differences in shifts as indicating that the amorphous materials are significantly more covalent than the crystalline, in keeping with the changes in interatomic distances. That is, the greater net positive charge of the Ge in the crystalline materials leads to larger core binding energies. Hence, these results provide striking further justification for the idea that, in the amorphous Ge-Te system, the bonding is quite covalent in spite of the fact that crystalline GeTe

- 3 -

microprobe analysis. In addition, bulk glasses with compositions

$\text{Ge}_{.15}\text{Te}_{.81}\text{Sb}_{.02}\text{S}_{.02}$ and $\text{Ge}_{.15}\text{Te}_{.81}\text{As}_{.02}\text{S}_{.02}$ were prepared by quenching from the melt. These compositions are memory type materials. Of these, one sample was studied before and after being heated to 275°C to achieve crystallization of the GeTe and Te .

ESCA experiments were performed on a Varian V-IEE15 (Induced Electron Emission) Spectrometer located at Varian Associates, Inc., in its standard form, using $\text{Mg } K_\alpha$ radiation. In this work, all shifts were measured relative to a carbon 1s reference line, to eliminate effects of sample charging, as discussed below.

The x-ray absorption edge measurements were performed at Stanford University on a Picker x-ray diffractometer with the normal powder sample replaced by a LiF single crystal, and a pulse height analyzer set so that $\lambda/2$ components of the x-ray beam were eliminated. Near the $\text{Ge } K_\alpha$ absorption edge, the dispersion of the instrument was 346 eV/degree (2- θ), which was just sufficient for the absorption edge shift measurements presented here. The analyzing crystal was not appropriate for measurements of the Te edge.

3. Experimental Results and Conclusions

The principles of operation of the IEE spectrometer have been summarized carefully and succinctly by Vesely and Langer⁶. Hence, we offer here just sufficient description to make the paper coherent. In this experiment $\text{Mg } K_\alpha$ x-rays incident upon the sample excite photoelectrons, whose kinetic energy, E_{kin} , is measured. Except for work function and sample charging effects, E_{kin} is just the difference between the x-ray photon energy, $E_{x\text{-ray}}$ and the core level binding energy, E_b . Following Vesely and Langer⁶ we write

- 2 -

cannot be described in that simple fashion.

The big difference between the shift in amorphous GeTe and those for crystalline GeS and GeSe also indicates that there is little similarity in the bonding schemes. Hence, a microcrystalline model for amorphous GeTe based on the GeS or GeSe structures also appears to have little justification.

It should be noted, however, that we have also considered the possibility of explaining these differences in shifts by assuming that the effective charge in amorphous GeTe is the same as that in the crystalline phase and that the differences are the result of changes in Madelung potential due to changes in interatomic distances. While we cannot rule this possibility out because the Madelung sums cannot be performed for the amorphous materials, we can say that if amorphous GeTe is assumed to have three nearest neighbors at 2.6\AA and another three at 4.1\AA , consistent with the radial distribution studies, then the nearest neighbor contribution to the Madelung energy would contribute in the opposite direction as the observed shift. Hence, a remarkably large contribution would have to be made by more distant neighbors. The constant charge model appears, therefore, to have little justification.

The conclusions presented thus far are reinforced by the x-ray absorption edge results presented in Table 2. Here, a negative shift indicates a decrease in the photon energy associated with the edge. We have interpreted these results from the previous work of White and McKinstry,⁷ rather than depending upon incomplete theoretical analyses. These authors show that in the covalent, four-fold coordinated quartz structure of GeO_2 , there is essentially no shift from the measured edge in crystalline Ge.

whereas in the ionic, six-fold coordinated rutile structure, the shift is ~ 6.1 eV. Similar types of results for the Ge-chalcogens are obtained in these studies. That is, in crystalline GeSe and GeTe, the shift is approximately -2.4 eV, whereas in the amorphous materials the shift ranges from -1.1 to -1.3 eV. The bonding thus appears to be significantly more covalent in the amorphous materials than in the crystalline.

Finally, it should be noted that both studies indicate that the core shifts in the amorphous materials are essentially independent of the sample compositions. This result indicates that the bonding form remains essentially the same throughout the composition range studied, in keeping with the general covalent picture.

Table I

X-RAY PHOTOELECTRON SPECTROSCOPY
FERMI-LEVEL REFERENCED SHIFTS OF BINDING ENERGY FOR CRYSTALLINE AND
AMORPHOUS COMPOUNDS

Sample	Ge Shift (eV)	Te Shift (eV)
GeTe (crystalline)	3.6	
GeSe (crystalline)	2.9	-2.7 (Se $3d^{5/2}$)
GeS (crystalline)	1.9	02.5 (S $2p^{3/2}$)
Ge _{.20} Te _{.80} (amorph.)	1.1	+0.4
Ge _{.33} Te _{.67} (amorph.)	1.0	+0.4
Ge _{.50} Te _{.50} (amorph.)	0.8	+0.4
Ge _{.57} Te _{.43} (amorph.)	1.1	
Ge _{.15} Te _{.81} Sb _{.02} (amorph.)	1.1	
Ge _{.15} Te _{.81} As _{.02} (amorph.)	1.1	+0.4
Ge _{.15} Te _{.81} As _{.02} (crystallized)	3.1	

FOOTNOTES

* This research was supported by the Advanced Research Projects Agency of the Department of Defense and was monitored by U. S. Army Research Office-Durham under Contract number DAI004-70-C-0044 and by the Advanced Research Projects Agency through the Center for Materials Research at Stanford University.

† This work will constitute part of a Ph.D. thesis to be submitted to Stanford University by FB.

** Present Address: The Hospital for Special Surgery, New York, New York 10021, U. S. A.

- 1) A. Bienenstock, F. Betts and S. R. Ovshinsky, J. Non-Crystalline Solids **2** (1970) 98.
- 2) F. Betts, A. Bienenstock and S. R. Ovshinsky, *ibid.* **4** (1970) 554.
- 3) D. B. Dove, M. B. Heritage, K. L. Chopra and S. K. Bahl, Appl. Phys. Letters **16** (1970) 138.
- 4) N. F. Mott, Advan. Phys. **16** (1967) 49.
- 5) M. H. Cohen, H. Fritzsche and S. R. Ovshinsky, Phys. Rev. Letters **22** (1969) 1065.
- 6) C. J. Vesely and D. W. Langer, Phys. Rev. B **4** (1971) 451.
- 7) E. W. White and H. A. McKinstry, in C. R. Mallett, M. J. Fay and W. M. Mueller, Editors, Advances in X-ray Analysis, Vol. 9, Plenum Press, New York, 1966, p. 376.

Table 2

Shifts of the Ge K_α Absorption Edge Relative to Crystalline Ge.

Sample	Shift (eV)
⁷⁰ GeTe	-2.48 ± 0.1
GeSe	-2.35 ± 0.1
*Ge ₃₄ Te ₆₆ (amorphous)	-1.16 ± 0.1
*Ge ₃₈ Te ₆₂ (amorphous)	-1.13 ± 0.1
*Ge ₅₇ Te ₄₃ (amorphous)	-1.11 ± 0.1
*Ge ₁₅ Te ₈₅ Sb ₀₂ S ₀₂ .02 (amorphous)	-1.31 ± 0.2
GeO ₂ (quartz structure) [†]	0.0 ± 1.0
GeO ₂ (rutile structure) [†]	-6.0 ± 1.0

[†]Data from reference 7.

S.C. ROWLAND

Department of Physics, Andrews University, Berrien Springs, Michigan 49104
and

SUBHA NARASIMHAN and A. BIENENSTOCK

Department of Materials Science and Engineering, Stanford University,
Stanford, California 94305

X-ray diffraction radial distribution studies of glassy $\text{Ge}_x\text{S}_{1-x}$ alloys, with $x=0.33$ and 0.42 have been performed. The interatomic distances in the $x=0.33$ sample, 2.2 and 3.55\AA , are consistent with those in the covalently bonded crystalline GeS_2 . The distances in the $x=0.42$ sample, 2.3 and 3.65\AA , are also consistent with covalent bonding, and show no relationship to those found in crystalline GeS . No evidence of a previously proposed octahedral coordination of Ge can be found. A tentative explanation for the existence of two separated glass-forming regions in this system is put forth.

I. INTRODUCTION

Recently, Kawamoto and Tsuchihashi have examined the glass-forming regions¹ and various physical properties² of glasses in the system $\text{Ge}_x\text{S}_{1-x}$. In KT1 they find two glass forming regions. The first, denoted (1) spans the compositions $0.0 < x < 0.33$ while the second region, denoted (2), is $0.40 < x < 0.432$. In KT2, these authors conclude the following about the glass structures. "The structure of glasses in region (1) can be described as follows: when S is added in small amounts to GeS_2 glass, the S forms $(-\text{S}-)_n$ chains between Ge atoms initially; then when the S content is GeS_{4-5} , the structure of the glasses becomes very open with many interstices which S_8 ring molecules can enter. Accordingly, S forms not only $(-\text{S}-)_n$ chains but also S_8 molecules. As the S content increases, the structure of the glass progressively approaches that of plastic S . However, in glass-forming region (2) the glasses are made up of GeS_2 and GeS components, i.e. of GeS_4 tetrahedra and GeS_6 octahedra." The authors associate the GeS_6 octahedra of the GeS components with the distorted rock-salt structure of the crystalline species and also assume that the GeS is of the form Ge^{+2} in this component.

This structural picture is quite different from that formed by Bienenstock et al.³ and Betts et al.^{4,5,6} of amorphous sputtered films and a bulk glass in the $\text{Ge}_x\text{Te}_{1-x}$ system. These authors find that the x-ray diffraction radial distributions of alloys with $x = 0.11, 0.17, 0.38, 0.54$ and 0.66 are quite similar in their basic features. In particular, covalent bonding always predominates. They find no indication of the existence of the octahedral coordination of Ge in the amorphous materials in spite of the fact that crystalline GeTe also has a distorted rock-salt structure. Hence, their structural proposals are quite different from those presented in KT2 for region (2). These authors also assume that the Te is always in the chain form in the Te -rich portion of region (1), but some difference between Te and S is to be anticipated from the structures of the elements.

suggested in KT1 and KT2, glassy GeS_2 appears quite similar in its basic coordination to glassy SiO_2 . On the other hand, it should be noted that the calculated area using the random covalent model of Betts et al.⁴ is 1355 electrons². Hence, it is possible that this model is more appropriate. As has been discussed previously⁵, it is extremely difficult to distinguish between such models on the basis of radial distribution studies.

The radial distribution of the $x = 0.42$ sample shows first and second neighbor peaks at 2.3 and 3.65Å, implying covalent bonding of almost all the atoms in the system. These distances are markedly different from those in the distorted rock-salt structure of crystalline GeS_2 , which has each Ge surrounded by 6 S atoms at distances 2.47Å (one S atom), 2.64Å (2 atoms), 2.91Å (1 atom) and 3.00Å (2 atoms).

The average separation of the three nearer neighbors, 2.58Å, in the crystalline material is significantly larger than the average separation in the amorphous $x = 0.42$ sample. Indeed, the radial distribution function is approaching a minimum at 2.6Å, indicating that very few atoms have such a separation in the amorphous material. Hence, it appears that almost all the nearest neighbor bonds in this sample are significantly shorter and, hence, more covalent, in this sample than in crystalline GeS_2 . Another indication of the significant difference between the bonding patterns in the amorphous $x = 0.42$ sample and crystalline GeS_2 is the minimum in the radial distribution function at 2.9Å, which is close to the average of the three further nearest neighbors in crystalline GeS_2 .

A possible explanation of this difference, however, is that the GeS_2 component described in KT2 is dominating the radial distribution. To determine if this is the case, we assumed that the glass could be described as a mixture of glassy GeS_2 and glassy GeS . Having the radial distribution for glassy GeS_2 , it was possible to subtract a constant multiple of it from the radial distribution for the $x = 0.42$ sample and obtain a radial distribution for the hypothetical GeS (actually $\text{Ge}_{0.55}\text{S}_{0.5}$ with our normalization scheme). The result is shown in Fig. 5. It is evident that the first neighbor peak shift is only to approximately 2.35Å, which is still significantly shorter than the average or shortest crystalline distance. Hence, it does appear as if the structure of this glass shows little resemblance to that of crystalline

Since the marked difference between the crystalline and amorphous coordinations near the composition $x = 0.5$ is a relatively unusual feature of the Ge-Te system, and because of the large differences between the structural pictures for the Ge-Te and Ge-S systems, we decided to perform the radial distribution studies presented below on two glassy $\text{Ge}_x\text{S}_{1-x}$ alloys to see if the structural picture presented in KT2 is correct, or if, alternatively, the structural pattern in region (2) is similar to that in the $\text{Ge}_x\text{Te}_{1-x}$ system.

II. EXPERIMENTAL

Bulk glasses of compositions $x = 0.33$ and 0.42 were formed by heating the high purity elements in evacuated (10^{-4} torr.) silica ampules slowly to approximately 1100°C, rocking them for several hours and then quenching in water. The x-ray diffraction data were collected as is described in reference 5 and were analyzed to obtain radial distribution functions as is described in reference 4. The atomic scattering factors of Benesch⁷ were used in the computations, and the appropriate densities were taken from KT2. The observed intensity data are presented in Figs. 1 and 2 while the radial distributions are shown in Figs. 3 and 4.

III. RESULTS AND CONCLUSIONS

The radial distribution for the $x = 0.33$ sample shows first and second neighbor peaks at 2.2 and 3.55Å, respectively. These distances are quite similar to those found⁸ in crystalline GeS_2 . The crystal shows relatively simple covalent bonding, with each Ge surrounded by 4 S atoms, the Ge-S distance varying from 2.07 to 2.26Å and with S-S second neighbor distances from 3.35Å upwards. Since the distances are quite similar in the amorphous material, it seems plausible to assume that a similar bonding pattern appears there as well. The area under the first neighbor peak of approximately 1200 electrons² agrees well with the area of 1356 electrons² calculated on the basis of tetrahedral coordination of the Ge by S. Hence, as is

GeS. Indeed, it appears as if the situation is quite similar to that in the Ge-Te system.

In KT2, however, no mention of phase separation is made. These authors assume that the GeS components act as network modifiers, with the Ge and S in their doubly ionized states and octahedrally coordinated. Hence, it is reasonable to ask what interatomic distance is to be anticipated from the sum of the ionic radii. That distance is approximately 2.6Å, which is close to the average separation in the crystalline compound and bears no relation to that found in the amorphous materials. Hence, we conclude that it is extremely unlikely that the GeS_6 octahedra are formed. Further evidence for this is obtained from the area under the first peak of the radial distribution in Fig. 5. It is approximately 2000 electrons², which yields an average coordination number of 4. While that number is highly suspect, since it is the result of the subtraction of two curves with their own uncertainties, it seems quite inconsistent with octahedral coordination in the GeS component, if it exists, of the glass.

Obtaining a reliable detailed structural picture for this system is more difficult⁵. The random covalent model of Betts et al.⁴ predicts a first neighbor peak area of 1643 electrons² which is in remarkably good agreement with the measured area of 1647 electrons². As discussed by Betts et al.⁵ however, other structural models yield agreement within experimental uncertainties. Hence, we must conclude that our detailed knowledge of the structures in the Ge-S system is as ambiguous as it is for the $\text{Ge}_x\text{Te}_{1-x}$ system.

Nevertheless, the work of Betts et al.^{4,5,6} on the Ge-Te system, when coupled with the radial distributions of Fawcett et al.¹⁰ on the Ge-Se system and the radial distributions presented here, yield a rather consistent picture of the relationship between crystalline and amorphous structures in the germanium chalcogenide systems. When the crystalline structure can be characterized by simple covalent bonding, with tetrahedral coordination of the Ge, as in GeS_2 , the interatomic distances in the crystalline and amorphous forms are almost exactly equal, within experimental error, and the areas are consistent with tetrahedral coordination of the Ge. When, on the other hand, the bonding in the crystalline materials is more complex, with distorted octahedral coordination and nearest neighbor distances which are significantly

longer than the sum of the covalent radii, the amorphous materials near that composition show interatomic distances which are covalent and lower coordinations.

This strong tendency for covalent bonding in the amorphous materials must lead us to search for an explanation of the crystal structures of GeS and GeSe in particular, as well as crystalline GeTe. It should be noted that crystalline GeS shows a marked distortion from the rock-salt structure in spite of the fact that the ionic radii have an almost ideal ratio for that structure. Hence, no argument can be made on that basis for the distortion. In their analysis of the structures of IV-VI compounds, Cohen et al.¹¹ argue that a large electronegativity difference (actually, antisymmetric potential) is required to support the rock-salt structure. If the electronegativity difference is small, there will be a distortion. In the Ge-chalcogenide sequence, however, the electronegativity differences in S and Se are significantly larger than in Te, yet the distortions in the former two are significantly larger than in the latter. Hence, their simple picture does not seem applicable. It should be noted, however, that they considered only the trigonal distortions of the sort found in GeTe, and not the orthorhombic type found in GeS and GeSe. Because of the relatively unique differences in structure between the crystalline and amorphous phases, a deeper understanding of the origin of the crystalline structures would be most desirable.

Since this paper presents strong arguments that the bonding is predominantly covalent in both regions (1) and (2) of the Ge-S system, it is interesting to question the origin of the existence of two separate glass-forming regions. We note, first of all, that there is an apparent conflict in the literature about these regions. As noted in KT1, Hilton et al.¹² indicate a glass forming region which is continuous from $x = 0$ to $x = 0.45$, approximately. The later report of Hilton¹³, however, indicates that the one sample they studied in the disputed region, with a composition of $x = 0.35$, is crystalline. Thus, the existence of an intermediate region of no glass-formation is found by both groups and there is a real phenomenon to be explained. We note, first of all, that the appearance of covalent bonding distances in both regions does not imply that the structural pattern is the

same in both regions. It is possible, for example, that the portion of region (1) close to GeS_2 does consist of $(\text{-S-})_n$ chains cross-linked by Ge atoms. Such a structure would end at GeS_2 . Region (2) might then consist of phase-separated glasses with compositions close to GeS_2 and GeS. The GeS would then be a covalently bonded type which is quite dissimilar to the crystalline form. On the other hand, the good agreement with both observed first neighbor peak areas obtained from the Random Covalent Model implies that it is possible that the glass structures do form a continuous structural pattern and that other reasons must be sought for the existence of two separated glass-forming regions.

The S-rich portion of region (1) is rather simple to rationalize on the same basis used to rationalize the glass-forming tendency of pure S. Region (2) can also be rationalized on the basis that it is right at the eutectic between GeS and GeS_2 ¹⁴. The major difficulty, then, comes in understanding why it is, as noted in KT2, that crystalline GeS_2 forms readily on the Ge-rich side of that compound, but does not form readily on the S-rich side. The question becomes all the more interesting when the phase diagram¹⁴ of the Ge-S system is studied. The liquidus maximum at GeS_2 is quite asymmetric, falling off quite slowly on the S-rich side relative to the Ge-rich side. Unless the melt behaves in an unusual manner, one would anticipate that it would be easier to form crystalline GeS_2 on the S-rich side, at the higher temperatures at which it becomes stable, than on the Ge-rich side. Since this is just the opposite of what is observed, it seems quite likely that the melt itself changes character at GeS_2 . On the S-rich side there is probably a great deal of the chain and ring like character of molten S retained in the melt, whereas this probably disappears on the Ge-rich side. This hypothesis also explains the asymmetric shape of the liquidus maximum, since it implies considerably more configurational entropy associated with the melt on the Ge-rich than the S-rich side. As a result, the melt is stable to much lower temperatures on the Ge-rich side.

In conclusion, then, it appears as if both glass-forming regions in the Ge-S system are characterized by covalent bonding. The radial distributions show no evidence of an octahedrally coordinated, doubly ionized Ge species. The existence of two separated glass-forming regions appears to result from characteristics of the melt, rather than structural features of the glasses.

Hence, the bonding scheme in the glassy Ge-S system appears to be quite similar to that found previously for the amorphous Ge-Te system.

FIGURE CAPTIONS

- Fig. 1. Scaled, polarization corrected, diffracted intensity as a function of $s(=4\pi \sin \theta / \lambda)$ for the sample with $x=0.33$. The dashed curve represents the scattering which is independent of atomic configurations.
- Fig. 2. Scaled, polarization corrected, diffracted intensity as a function of $s(=4\pi \sin \theta / \lambda)$ for the sample with $x=0.42$. The dashed curve represents the scattering which is independent of atomic configurations.
- Fig. 3. Calculated radial distribution for the sample with $x=0.33$.
- Fig. 4. Calculated radial distribution for the sample with $x=0.42$.
- Fig. 5. Hypothetical radial distribution for glassy GeS calculated on the basis of a phase separated model of the $x=0.42$ sample. This distribution was obtained by subtracting a fraction of Fig. 1 from Fig. 2 and then renormalizing to the composition $x=0.5$.

FOOTNOTES

- * This research was supported by the Advanced Research Projects Agency of the Department of Defense and was monitored by U.S. Army Research Office-Durham under Contract number DAHCO4-70-C-0044 and by the Advanced Research Projects Agency through the Center for Materials Research at Stanford University.
- 1) Y. Kawamoto and S. Tsuchihashi, *J. Amer. Ceram. Soc.* **52**, 626 (1969) Henceforth, denoted KT1.
 - 2) Y. Kawamoto and S. Tsuchihashi, *J. Amer. Ceram. Soc.* **54**, 131 (1971). Henceforth, denoted KT2.
 - 3) A. Bienenstock, F. Betts and S.R.Ovshinsky, *J. Non-Cryst. Solids* **2**, 347 (1970).
 - 4) F. Betts, A. Bienenstock and S.R.Ovshinsky, *J. Non-Cryst. Solids* **4**, 554 (1970).
 - 5) F. Betts, A. Bienenstock, D.T. Keating and J. deNeufville, submitted for publication.
 - 6) F. Betts, Ph.D. thesis, Stanford University, 1972. Unpublished.
 - 7) R. Benesch, M.S. thesis, University of Alberta, 1967. Unpublished.
 - 8) W.H. Zachariasen, *J. Chem. Phys.* **4**, 618 (1936).
 - 9) W.H. Zachariasen, *Phys. Rev.* **40**, 917 (1932).
 - 10) R.W. Fawcett, C.N.J. Wagner and G.S. Cargill, III, to be published in the Proceedings of the Fourth International Conference on Amorphous and Liquid Semiconductors, Ann Arbor, 1971.
 - 11) M.H. Cohen, L.M. Falicov and S. Golin, *IBM J. Res. Dev.* **8**, 215 (1964).
 - 12) A.R. Hilton, C.E. Jones and M. Braw, *Infrared Phys.* **4**, 213 (1964).
 - 13) A.R. Hilton, Texas Instruments Report No. 08-65-121, 30 September, 1965. Texas Instruments, Inc. Unpublished.
 - 14) C.-H. Liu, A.S. Pashinkin and A.V. Novoselova, *Dokl. Chem., Proc. Acad. Sci., USSR*, **151**, 662 (1963).

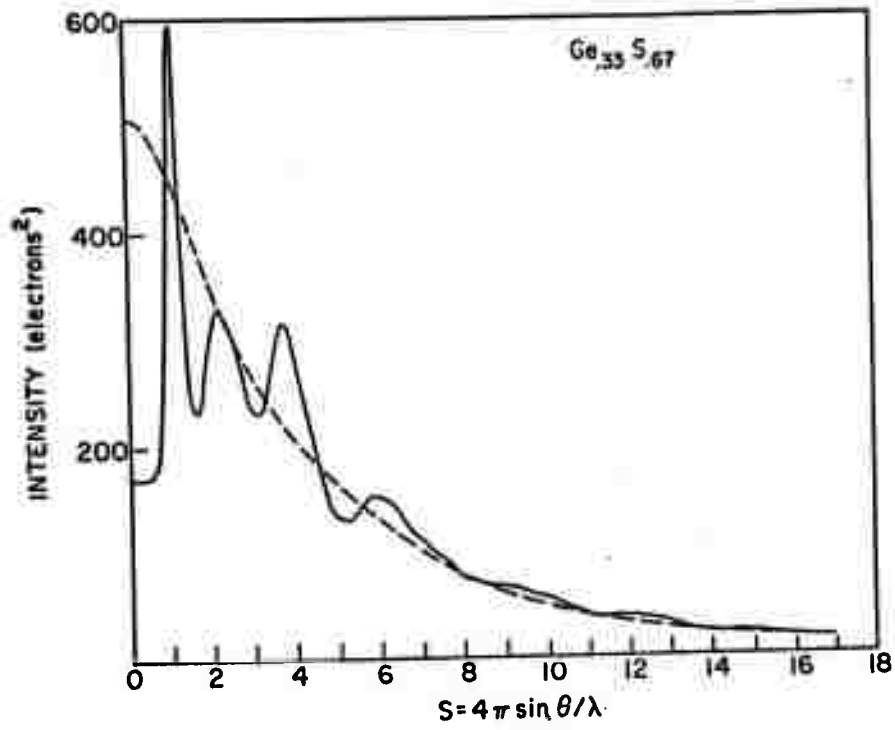


Fig 1

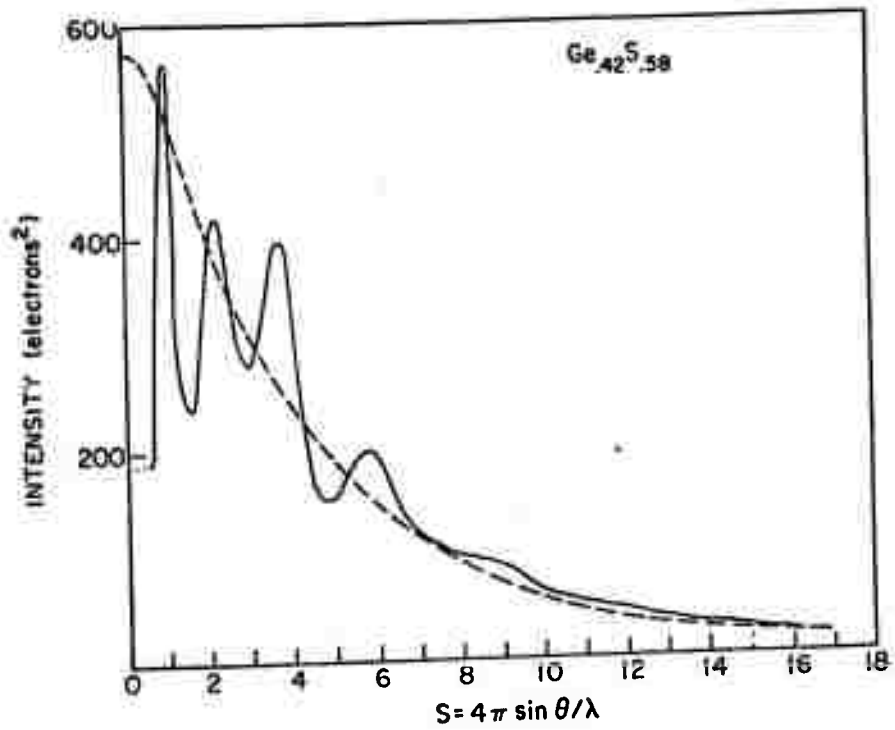


Fig 2

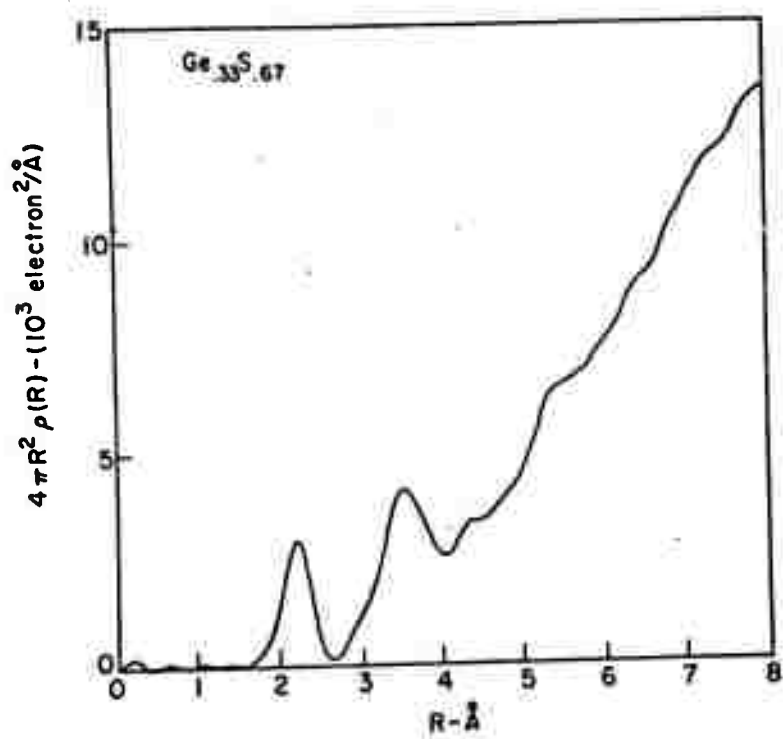


Fig 3

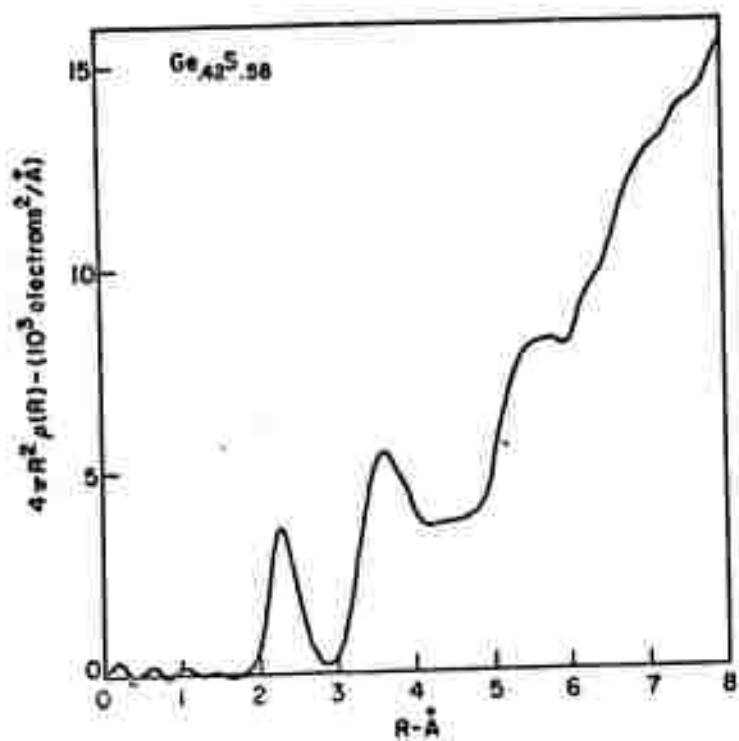
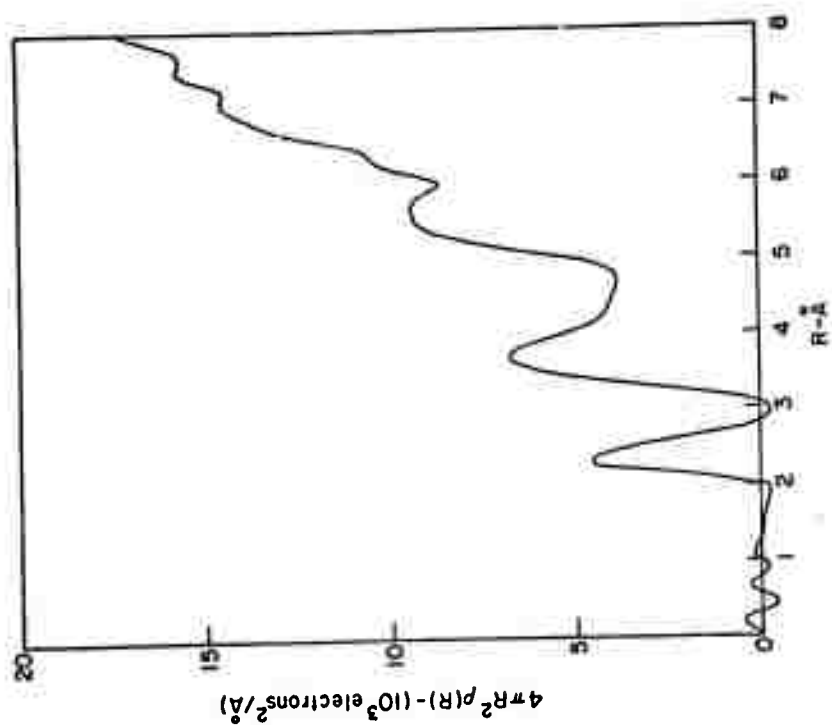


Fig 4

Fig 5



ANALYSIS OF PHOTOCONDUCTIVITY IN AMORPHOUS CHALCOGENIDES

T. C. Arnoldussen and R. H. Bube*
Department of Materials Science
Stanford University
Stanford, California 94305

and
E. A. Fegen and S. Holsberg**
Energy Conversion Devices, Inc.
Troy, Michigan 48064

ABSTRACT

Starting with standard semiconductor recombination statistics and a generalized distribution of localized states within the mobility gap of an amorphous semiconductor, a model for photoconductivity has been developed. Consistency with experimental phenomena requires the inclusion in this model not only of the traditional non-localized to localized state recombination transitions, but also of two types of localized to localized state recombination transitions: (a) from states nearer than a critical energy to the conduction edge, to similar states nearer than a critical energy to the valence edge; and (b) from states near the mobility edges to states near the thermal equilibrium Fermi level. Such a model has general applicability to a variety of different types of amorphous chalcogenides, encompasses previously reported variations of photoconductivity with intensity and temperature, and provides a way of estimating the characteristic parameters of localized states in these materials. Quantitative application of the model is made to photoconductivity data for three amorphous chalcogenides.

* Sponsored by the Advanced Research Projects Agency under Contract No. DARC04-70-C-0044.

** Sponsored by the Advanced Research Projects Agency under Contract No. DARC-70-C-0187.

INTRODUCTION

Two features of amorphous materials of considerable interest are the density and energy-distribution of localized states, and the nature of the charge transport process. We have obtained measurements of the intensity and temperature dependence of photoconductivity for several amorphous chalcogenides over a wider range of these variables than has previously been reported. The various regimes thus defined serve as realistic physical constraints on the kind of photoconductivity model that is constructed in terms of the localized states and transport processes present.

Discussion of recombination statistics in semiconductors generally starts with the analysis of Shockley and Read¹ and its various elaborations. Almost all such treatments, whether involving discrete levels, distributions of levels, or multivalent defects, consider only those recombination transitions in which band-to-level or level-to-band processes are involved. This is the starting point also for the development of our model in this paper, but we show that faithfulness to the experimental data requires in addition the consideration of two types of localized-to-localized level transitions. It is possible in a consistent way to develop a photoconductivity model which is able to describe all the regimes of intensity and temperature variation, and thereby to provide a means for determining the characteristic parameters of the localized state distribution and of the transport processes.

PHOTOCONDUCTIVITY CHARACTERISTICS

A maximum in the temperature dependence of photoconductivity has been reported for a variety of amorphous materials.²⁻⁹ Also reported have been a linear variation of photoconductivity with intensity in the small-signal case and a square-root variation in the large signal case. The photoconductivity characteristics we measure include such behavior

(4) In the low-temperature region, the photoconductivity is much larger than the dark conductivity, varies linearly with intensity, and approaches a constant value asymptotically. A constant photoconductivity at low temperatures, barring the ~~presence~~ exactly compensating opposite temperature dependence of carrier density and mobility, indicates constant carrier density and mobility. The low-temperature constant value of mobility is designated μ_{LT} .

DEFINITION OF TERMS

The basis for our model is the assumption of a distribution of non-localized (NL) states above a conduction mobility edge and below a valence mobility edge, and a distribution of localized (L) states between these two edges. Figure 3 illustrates the principal features of the model.

Energies are measured from the valence mobility edge. The energy E_G indicates the location of the conduction mobility edge, and we refer to E_G as the "thermal bandgap." It is assumed that conductivity by electrons takes place at or above the conduction edge in non-localized states with an effective density N_c , and that conductivity by holes takes place at or below the valence edge in non-localized states with an effective density N_v .

We assume that localized states are of two general types; those that are neutral when empty of electrons, with distribution $g_c(E)$ $\text{cm}^{-3} \text{eV}^{-1}$, which we call C states; and those that are neutral when filled with electrons, with distribution $g_v(E)$ $\text{cm}^{-3} \text{eV}^{-1}$, which we call V states. A positively charged V state with one missing electron is said to be occupied by a hole. This choice of terminology is dictated by the fact that such C states might be identified with conduction-band-like states, and V states with valence-band-like states, because of the similarity of the dependence of charge state on occupancy. Such an identification would

end other significant variations as well.

Data on the temperature and excitation intensity dependence of photoconductivity in amorphous chalcogenides are available for three materials considered in this paper: $\text{Ge}_{15}\text{Te}_{81}\text{Sb}_2\text{S}_2$, $\text{S}_{11}\text{Ge}_{11}\text{As}_{35}\text{P}_{20}\text{Te}_{40}$, and $\text{Ge}_{16}\text{As}_{35}\text{Te}_{28}\text{S}_{21}$. The photoconductivity characteristics of these three materials are quite similar. Actual data for $\text{Ge}_{15}\text{Te}_{81}\text{Sb}_2\text{S}_2$ are shown in Figure 1, and for the other two materials in Figure 2. The most carefully controlled and detailed measurements to date have been made on the $\text{Ge}_{15}\text{Te}_{81}\text{Sb}_2\text{S}_2$. Summaries of the parameters of the data of most interest are given in Table 1.

The following qualitative properties may be discerned.

- (1) In the high-temperature region above the maximum, the photoconductivity is smaller than the dark conductivity, varies linearly with excitation intensity, and increases exponentially with $1/T$ with an activation energy of E^+ .
- (2) In the intermediate-temperature region immediately below the maximum, the photoconductivity decreases exponentially with $1/T$ with an activation energy of E^- , varies as the square-root of the intensity for high intensities and linearly with intensity for low intensities.
- (3) Between these two regions, the photoconductivity reaches a maximum value at T_{\max} . It follows that the value of T_{\max} shifts to lower temperatures with decreasing excitation intensity if the photoconductivity in the intermediate-temperature region varies as the square-root of the intensity, and is intensity independent if the intermediate-temperature region is characterized by a linear dependence of photoconductivity on intensity. It likewise follows that in a range in which T_{\max} is shifting with intensity, the apparent activation energy for the shift in the maximum photoconductivity, $E_{\max} = 2(E^+ + E^-)$.

be consistent with the assumptions of the CPO model of an amorphous material.¹² Such an identification, however, is not a necessary ingredient of the model being developed here, and the final choice of whether or not to identify states near the conduction edge as C states and states near the valence edge as V states must be derived from the degree of quantitative agreement between model-predicted and experimentally measured parameters. For consistency in the following discussion, we will speak as if C states extended into the gap from the conduction edge, and as if V states extended into the gap from the valence edge.

We assume that recombination takes place either by interaction between a carrier in an NL state and a carrier in an L state, or by interaction of an electron in a C state with a hole in a V state. We neglect the direct recombination between NL electrons and NL holes, as well as interactions between two C states, between two V states, or between a neutral C state and a neutral V state. The recombination coefficients can then be defined as shown in Table II.

GENERAL FORMULATION OF THE MODEL

The formal procedure for calculating the steady-state photo-excited carrier concentration is to (a) write the steady-state occupancy function for a single L level in terms of all possible transitions to other L and NL states, and (b) write the free carrier continuity equation in terms of these occupancy functions integrated over all L states.

In a steady state, the rate at which electrons enter a C state, for example, is equal to the rate at which electrons leave that state. The occupancy function $f_C(E)$ for a C state is given by

$$\sum_i (R_{in})_i [1 - f_C(E)] g_C(E) = \sum_j (R_{out})_j f_C(E) g_C(E) \quad (1)$$

where $(R_{in})_i$ is the product of the electron concentration in the initial state i and the rate constant for an electronic transition from state i to a $g_C(E)$

state; and $(R_{out})_j$ is the product of concentration of available final states j and the rate constant for an electronic transition from a $g_C(E)$ state to state j .

Then

$$f_C(E) = \frac{\sum_i (R_{in})_i + \sum_i (R_{in})_i \uparrow}{\sum_i (R_{in})_i + \sum_i (R_{in})_i \uparrow + \sum_j (R_{out})_j + \sum_j (R_{out})_j \uparrow} \quad (2)$$

where we have separated the terms into upward (\uparrow) and downward (\downarrow) transitions of electrons into or out of the $g_C(E)$ state. A similar expression can be written for $f_V(E)$, the occupancy of V states by holes.

All of the terms in Eq. (2) can be written out explicitly using the quantities previously defined.

$$\sum_i (R_{in})_i \downarrow = n C_C^0(E) \quad (3)$$

$$\sum_i (R_{in})_i \uparrow = N_V C_C^0(E) e^{-E/kT} + 2 \int_0^E K(E, E') e^{(E'-E)/kT} [1 - f_V(E')] g_V(E') dE' \quad (4)$$

$$\sum_j (R_{out})_j \downarrow = \frac{1}{2} p C_C^0(E) + \frac{1}{2} \int_0^E K(E, E') f_V(E') g_V(E') dE' \quad (5)$$

$$\sum_j (R_{out})_j \uparrow = \frac{1}{2} N_C C_C^0(E) e^{(E-E_C)/kT} \quad (6)$$

The continuity equation for NL electrons under steady-state excitation P , the rate of generation of NL electron-hole pairs by incident light, is given by

$$\begin{aligned} \frac{dn}{dt} = 0 = P - \int_0^{E_C} C_C^0(E) [1 - f_C(E)] g_C(E) dE - \frac{1}{2} \int_0^{E_C} N_C C_C^0(E) e^{(E-E_C)/kT} f_C(E) g_C(E) dE \\ + \frac{1}{2} \int_0^{E_C} N_V C_C^0(E) e^{(E-E_C)/kT} f_V(E) g_V(E) dE \\ + \int_0^{E_C} N_C C_C^0(E) e^{(E-E_C)/kT} [1 - f_V(E)] g_V(E) dE \end{aligned} \quad (7)$$

The factors $1/2$ and 2 enter these equations as a result of assuming that the L states are s -like with a spin degeneracy of 2 , capable of being occupied by only

"steps." The transition rate of the slowest step in a given path controls the overall recombination rate for that path, whereas the overall rate of the fastest path dominates the total recombination rate of the system.

We need to deal with two types of path. First there is the possibility of the capture of a NL carrier at a L state with subsequent capture of the oppositely charged NL carrier; this is a two-step process. Second, an electron in an NL state could be captured by a C state, then make a transition to a V state, which finally captures a NL hole; this is a three-step process. We shall neglect more complicated possible paths.

For any given step, the transition rate is

$$r_{ij} = n_i c_{ij} p_j - n_i^0 c_{ij} p_j^0 \quad (8)$$

where the i and j refer respectively to the initial and final states of the electron, n_i is the concentration of electrons in the initial state, p_j is the concentration of holes (or states available to an electron) in the final state, c_{ij} is the rate constant for this transition, and the superscript 0 denotes thermal equilibrium values. The slowest step rate r_{ij} for each path determines the individual path rates; the sum of all these parallel path rates is the total recombination rate.

For a given condition of temperature and light intensity, however, only a fraction of all possible paths will contribute significantly. If these dominant transitions should all be of the same type, but with some energy spread in the initial and final states, we can write

$$r = \sum_{ji} c_{ji} \int_{ji} n_i n_j dE_i dE_j \quad (9)$$

where $r(E_i, E_j)$ is the continuous analog of the discrete r_{ij} 's.

For example, if localized-localized transitions dominate with electrons in C states with density $g_c(E_i)$ between E_{i1} and E_{i2} recombining with holes in V states with density $g_v(E_j)$ between E_{j1} and E_{j2} , the rate

of an electronic charge. A continuity equation similar to Eq. (7) could be written for NL holes. If n and p are the NL electron and hole concentrations in the light, then $\Delta n = n - n_0$ and $\Delta p = p - p_0$ are the excess photo-excited carrier concentrations expressed in terms of the thermal equilibrium concentrations n_0 and p_0 .

Relationships like those given in Eqs. (2) and (7) can be used in principle to calculate the steady-state photoexcited carrier concentrations as a function of temperature and light intensity, provided that certain assumptions are made about the energy dependence of the densities of L states and of the rate coefficients. We have done such calculations for several cases in detail, but feel that to present them here in toto would tend to obscure the physical processes giving rise to the observed photoconductivity behavior. We choose instead to follow an alternate equivalent approach, hopefully richer in physical insight.

The occupation function given in Eq. (2) can be simplified by considering specific energy ranges of interest. Table III summarizes the inequalities that hold for C states, where the concepts of electron (located at E_{dn}^c) and hole (located at E_{dp}^c) demarcation levels have been introduced. The statements given in Table III serve to define the energies introduced. Similar statements can be made for the V states, their occupation functions, and their demarcation levels E_{dn}^v and E_{dp}^v .

Table III also contains a summary for C states of the simplified form of the occupation function which is obtained in the four energy ranges into which the Fermi levels and demarcation levels divide the mobility gap. Again similar statements can be made for V states.

METHOD OF "PATHS AND STEPS"

Many parallel "paths" exist by which an electron can make a transition from a NL conduction state to recombine with a hole in a NL valence state. Each such path may be composed of a number of individual

is assumed, the carrier density depends only slightly from a linear dependence on light intensity in the large-signal case, and although a maximum in the photoconductivity is found, a variation of carrier density with $1/T$ much slower than exponential is predicted for both higher and lower temperatures. The maximum in the photoconductivity is a general characteristic of all forms of the model, and occurs at or near the transition from the large-signal to the small-signal regime with increasing temperature.

As an example of the properties of an exponential L state distribution, consider a symmetric distribution, $g_c(E) = g_v(E_c - E)$, where $g_c(E) = G e^{-(E-E_c)/kT}$ and where T is a constant describing the rate of the exponential variation with temperature. Two types of result are found, depending on whether the decrease in the exponential L state distribution is less or more rapid than the decrease in the Boltzmann tail of the occupation function. For "diffuse" exponential distributions ($T \gg T$), the carrier density varies linearly with light intensity as expected in the small-signal case and as the $T^2/(T+T^*)$ power of intensity in the large-signal case (still close to unity), and neither above nor below the maximum is an exponential variation of carrier density with $1/T$ predicted. The "sharp" exponential distribution ($T^* < T$) shows the first practical signs of approaching the experimental data, and thus provides the clue as to what changes should be made in the model. For a "sharp" distribution, the carrier density varies linearly with light intensity in the small-signal case and as the square-root of the intensity in the large-signal case; furthermore, at temperatures above that of the maximum photoconductivity the carrier density increases exponentially with $1/T$. At temperatures below the maximum photoconductivity, however, even the "sharp" exponential distribution of L states does not give a rapid variation of carrier density with temperature. Analytical expressions for the variation of carrier density with intensity and temperature are summarized in Table IV

equation becomes

$$P = \int_{E_{j1}}^{E_{j2}} dE_j \int_{E_{i1}}^{E_{i2}} dE_i \frac{1}{2} K(E_i, E_j) g_c(E_i) g_v(E_j) \cdot \left[z_c(E_i) \bar{z}_v(E_j) - z_c^0(E_i) \bar{z}_v^0(E_j) \right] \quad (10)$$

Or if the dominant process were the capture of NL holes by C states between

E_1 and E_2 , the rate equation is

$$P = \frac{1}{2} p \int_{E_1}^{E_2} C_h^-(E) g_c(E) f_c(E) dE - \frac{1}{2} p_0 \int_{E_1}^{E_2} C_h^-(E) g_c(E) f_c^0(E) dE \quad (11)$$

Any other dominant rate process can be written in analogous form. Of course, the problem then becomes one of determining which types of transition are dominant under specific conditions of temperature and excitation intensity.

DEVELOPMENT OF THE MODEL

NL to L Transitions, and Uniform or Exponential Distribution of L States

The simplest type of model with the general characteristic outlined above is that in which only NL to L transitions are considered, and in which some continuous distribution of L states is assumed, e.g., uniform or exponential in density with energy. This is the type of model closest to the semiconductor analog, and it is as convenient for this model to obtain the detailed solution of Eqs. (2) and (7) as it is to pursue the more physically oriented method of paths and steps. Simmons and Taylor¹³ have examined this model in some detail, including symmetric and asymmetric variations of an exponential L state distribution. Because it ultimately falls short of adequacy in describing the experimental photoconductivity results, we shall not devote much attention here to this form of the model.

We may take the simplified forms of Eqs. (3) through (6) for this model, calculate explicitly the occupancy functions, and perform the integrations over the chosen L state distribution. If a uniform distribution of C and V states

for the uniform, "diffuse" exponential and "sharp" exponential distributions of localized states.

This experience leads directly to the conclusion that regions in which the carrier density increases exponentially with $1/T$ at temperatures above the maximum and decreases exponentially with $1/T$ at temperatures below the maximum, exist together only if the density of effective recombination centers (the product of the density of states and the appropriate rate coefficient) is limited to regions of the mobility gap lying within some energy E_V^* from the valence edge and within $(E_C - E_V^*)$ from the conduction edge, as indicated in Figure 3. Such a condition can be met in several different ways, e.g., (a) by a single discrete C level and a single discrete V level; (b) by a rapid decrease in density of V levels as the energy exceeds E_V^* , and a rapid increase in density of C levels as the energy exceeds E_C^* , the variation in the density of C and V levels over other energy ranges being much slower; or (c) by a rapid decrease in the appropriate recombination rate coefficient as the energy exceeds E_V^* , and a rapid increase in the rate coefficient as the energy exceeds E_C^* . Although one may wish to discount possibility (a) in an amorphous material, a unique choice between (b) and (c) is not possible from the photoconductivity results alone.

L to L Transitions, Abrupt Distribution of L States

The model described to this point contains only recombination NL to L transitions. There are both external and internal reasons for considering the effect of L to L transitions, such as those indicated as Transition 2 in Figure 3.

Weiser et al.⁶ have previously suggested a recombination process in As_2Se_3 - As_2Te_3 materials which corresponds to Transition 2, and have subsequently shown the existence of apparently corresponding luminescence emission.¹⁴ In describing their results, Weiser et al. postulate a "recombination gap" with smaller magnitude than the "mobility gap," which corresponds to the

energy level at which carriers in L states become too bound to move sufficiently to encounter probable recombination with similarly migrating holes. Thus the model of Weiser et al. can be identified as choice (c) above with a particular interpretation for the energy dependence of $K(E, E')$. Another interpretation of this energy dependence might disregard migration of carriers in L states over appreciable distances completely, and be related instead to the extent of pair-overlap between electrons and holes on neighboring C and V states respectively.

A reason for including L to L transitions also arises from within our model itself. When a symmetric or asymmetric abrupt distribution of L states is used to calculate the carrier density in a model involving only NL to L transitions, all of the appropriate types of temperature dependence are possible, but when the actual values of the activation energies from these temperature ranges are compared with the predicted value of the dark conductivity activation energy, disagreement is frequently found. One way to attempt to overcome this disagreement is to suppose the possibility of a thermally activated mobility for the NL carriers. Although this is an apparently helpful inclusion, particularly since it also seems indicated by the temperature dependence of the thermoelectric power where this has been measured,¹¹ it is by itself not adequate to remove the disagreement. It is possible to remove the disagreement, however, by including recombination transitions from L states near the conduction edge (Transition 2 in Figure 3) to L states near the valence edge. The actual expressions derived from our model are given in the following section, but Table V gives an indication of the nature of the resolution for the $Ge_{15}Te_{85}Sb_2S_2$ material in the symmetric L distribution approximation.

To this point of the development, with effective recombination centers restricted to regions of the mobility gap near the edges, we conclude that the high-temperature exponential variation of carrier density with $1/T$ can be described in terms of either Transition 1 (NL to L) or Transition 2 (L to L) governing the recombination rate. The exponential variation of carrier density with $1/T$ in the intermediate temperature range, and the square-root variation with intensity (at high intensities) can be described in terms of Transition 3 governing.

L to L Transitions Including States Near Fermi Level, Abrupt Distribution of L States with Tails

None of the transitions discussed so far are able to account for both the exponential variation of carrier density with $1/T$ and the linear dependence on intensity for low intensities as observed in the intermediate temperature range. If the square-root variation at high intensities arises physically from the L to L transitions between pairs of states with varying occupancy, then a linear variation at low intensities can be expected if transitions occur predominantly from one set of states with changing occupancy to another set of states with approximately constant occupancy. Guided by the often cited evidence of a fairly high density of states near the thermal equilibrium Fermi level¹⁶, we find that the linear variation with intensity at low intensities in the intermediate temperature range can be described in terms of transitions from the L states near the mobility edges to L states near the equilibrium Fermi level (with density $N_{fo} \text{ cm}^{-3}$). Such transitions are indicated as Transitions 3 in Figure 3, with rate coefficients K' and K'' .

For generality we consider both symmetric and asymmetric forms of this basic model.

CALCULATION OF PHOTOCONDUCTIVITY FROM GENERAL MODEL

In this section we develop expressions for the photoconductivity on the basis of our general model, using the method of paths and steps as outlined above. In keeping with experimental results, we assume an asymmetric distribution of L states, leading to conduction by holes, or an asymmetric distribution of L states with greater hole than electron mobility. We express the mobility of NL holes as $\mu_o e^{-E_h/kT}$, allowing final comparison with the numerical data to decide as to the need for or the value of E_h .

High-Temperature Region: $\Delta n, \Delta p \ll n_o, p_o$

The dominant recombination path is either that involving Transitions 1 and 4, or that involving Transitions 2 and 4. Transitions 4 will always dominate in these paths over Transitions 1 and 2, unless the states involved are C states below E_{dn}^c or V states above E_{dp}^v . These latter conditions are important only in the low-temperature range, and there it can be shown that the dominant second step, whether Transition 1, 2, or 3, is equal to Transition 4 in rate.

Near thermal equilibrium the condition that states at the Fermi level govern charge neutrality gives

$$\frac{\Delta n}{\Delta p} = \frac{n_o}{p_o} \left[\frac{e^{(E_h - E_{dp})/kT}}{e^{(E_h - E_{dn})/kT}} \right] \quad (12)$$

For states near the mobility edges, $f_o(s) = \exp [(E_h - s)/kT]$, and $\bar{f}_v(E) = 2 \exp [(E - E_{fp})/kT]$.

If Transition 1 is more important than Transition 2 at high temperatures, then from the above relationships and an equation like Eq. (11) to account for electrons being captured at or below E_h^+ , and holes being captured at or above E_h^+ , we obtain

$$\Delta \sigma_{HT-1} = \frac{N_V e \mu_0 e^{-E_V/KT}}{2 \left[g_C(E_V^+) C_V^-(E_V^+) e^{(E_V^+ - E_V^-)/KT} + \frac{N_C}{N_V} g_V(E_V^+) C_V^-(E_V^+) e^{(E_V^+ - E_V^- - E_{I0} - E_C)/KT} \right] \left[1 + \frac{g_C(E_{I0})}{g_V(E_{I0})} \right]} \quad (13)$$

This result, as well as others that follow, are of the same basic form regardless of whether discrete defect states at E_V^+ and E_C^+ are assumed, or whether E_V^+ and E_C^+ mark instead the energies where a slow tailing of states from the mobility edge falls to a much smaller density of states as indicated in Figure 3.

If Transition 2 is more important than Transition 1 in the high-temperature region, an equation like Eq. (10) gives

$$\Delta \sigma_{HT-2} = \frac{N_V e \mu_0 e^{-E_V/KT} e^{(E_V^+ - E_V^- - E_{I0})/KT}}{2 (KT)^2 K(E_V^+, E_V^-) g_C(E_V^+) g_V(E_V^-) \left[1 + \frac{g_C(E_{I0})}{g_V(E_{I0})} \right]} \quad (14)$$

Intermediate-Temperature Region, Low Intensities: $\Delta n, \Delta p < n_0, p_0$

Conditions are still close to those characteristic of thermal equilibrium. The lowered temperature has depopulated the states near the mobility edges associated with E_C^+ and E_V^+ , while the states near the Fermi level remain largely populated. It is proposed that under these conditions Transitions 3 dominate over Transitions 2, even though the transition coefficients K' and K'' may be smaller than the coefficient K .

Charge neutrality is still governed by states near E_{I0} , giving the relationship of Eq. (12). In the same way that the photoconductivity in the high-temperature region was calculated above for Transition 2 governing, we can use an equation like Eq. (10) to calculate the photoconductivity in the intermediate-temperature range and low light intensities with Transitions 3 dominating.

$$\Delta \sigma_{IT-low} = \frac{N_V e \mu_0 e^{-E_V/KT}}{K(E_C^+, E_V^-) g_C(E_C^+) g_V(E_V^-) e^{(E_C^+ - E_V^-)/KT} + K'(E_{I0}, E_V^-) g_C(E_V^-) e^{(E_{I0} - E_V^-)/KT} + K''(E_{I0}, E_V^-) g_C(E_V^-) e^{(E_{I0} - E_V^- - E_{I0})/KT}} \quad (15)$$

Intermediate-Temperature Region, High Intensities: $\Delta n, \Delta p \gg n_0, p_0$

With increasing light intensity in the intermediate-temperature region we pass to the large-signal case and away from thermal equilibrium. The steady-state Fermi levels with energy E_{Fn} and E_{fp} are split; so also are the electron and hole demarcation levels. If the demarcation level splitting is not so great that $E_{Fn}^+ > E_C^+$ or $E_{fp}^- < E_V^+$, then the occupation of C states above E_C^+ and of V states below E_V^+ are still given respectively by the same $f_C(E)$ and $\bar{f}_V(E)$ functions used above. But if the demarcation levels are sufficiently split that the bulk of those states near the thermal equilibrium Fermi level, which previously had been almost entirely populated, now fell between the demarcation levels, the approximation for the occupation function given in Table III indicates that these states are now quite depopulated. Charge neutrality under these new conditions will be governed by those states above E_C^+ and below E_V^+ , which are now more populated. This new charge neutrality condition, under the implicit assumption that there is an abrupt change in the density of states at E_C^+ and E_V^+ , gives in place of Eq. (12),

$$\frac{\Delta n}{\Delta p} \sim \frac{n}{p} \sim \frac{N}{P} \frac{g_V(E_V^+)}{g_C(E_C^+)} e^{(E_V^+ - E_C^+)/KT} \quad (16)$$

Because of the increased population of the states near the mobility edges, Transition 2 is more important than Transitions 3, with the result that

$$\Delta\sigma_{\text{IT-high}} = \left[\frac{N_V e \mu_0}{4kT^2} \frac{s^{-E_F/kT} e^{-E_V^*/kT}}{2kT E_V(E_V^*)} \right]^{1/2} \quad (17)$$

Comparison of Eqs. (15) and (17) indicates how it is possible to pass from a linear variation of carrier density on intensity to a square-root variation with increasing intensity, while at the same time maintaining the same activation energy for the exponential decrease in carrier density with $1/T$ (if K'' term in denominator of Eq. (15) dominates).

Low-Temperature Region: $\Delta n, \Delta p \gg n_0, p_0$

At low temperatures where the photoconductivity has reached a constant asymptotic value, the demarcation levels are so widely split that essentially all the localized states in the mobility gap lie between the demarcation levels. Table III indicates that the occupation function of any C state is

$$f_C(E) \approx \sum_i (R_i \psi_i) / \sum_j (R_j \psi_j) \quad (18)$$

A similar relation holds for V states.

We have assumed that the only downward transitions into a C state of significance are those associated with trapping of NL electrons by neutral C states, i.e., $\sum_i (R_i \psi_i) = n C_0^0(E)$. The total capture rate by this level is $n C_0^0(E) g_C(E)$. But the total downward transition rate out of this state by Transition 1, 2 or 3 is simply $g_C(E) f_C(E) \sum_j (R_j \psi_j)$. It follows from Eq. (18) that whichever step or steps of Transition 1, 2 or 3 dominates, it is just equal to the neutral trapping rate of NL electrons in C states. A similar statement can be made for holes being trapped by V states. For the low-temperature region, therefore,

$$\Delta\sigma \approx \Delta n \int_0^{E_G} C_0^0(E) g_C(E) dE + \Delta p \int_0^{E_G} C_0^0(E) g_V(E) dE \quad (19)$$

If Transition 2 or 3 is faster than Transition 1, only the smaller of the two terms given in Eq. (19) controls the recombination rate.

Replacing the lower limit of the first integral in Eq. (19) by E_C^* , and the upper limit of the second integral in Eq. (19) by E_V^* , and taking $\Delta n \approx \Delta p$ in this limit, we obtain

$$\Delta\sigma_{\text{LT}} = \frac{F e \mu_0 / L T}{\int_{E_C^*}^{E_G} C_0^0(E) g_C(E) dE + \int_0^{E_V^*} C_0^0(E) g_V(E) dE} \quad (20)$$

APPLICATION OF THE MODEL

Before applying the model to the quantitative evaluation of measured photoconductivity values for three amorphous materials, we may point out that the model proposed by Waiser et al. [10] for data on As_2Se_3 - As_2Te_3 corresponds to our symmetric model in which one passes with increasing excitation intensity from what we have called the high-temperature regime with Transition 2 governing at low intensities, to what we have called the intermediate-temperature regime with Transition 2 governing at high intensities, i.e., a change from one side of the maximum to the other with increasing intensity. It is this behavior which is responsible for the characteristic crossing of photoconductivity vs. light intensity curves measured at various temperatures near the maximum.

Characteristic energies derived from the data of Figures 1 and 2 are summarized in Table VI. Since thermoelectric power vs. temperature is currently available only for the $\text{Ge}_{15}\text{Te}_{81}\text{Sb}_{22}$ material, [11] only symmetric model results are given for the other two materials. It is apparent that the characteristic energies derived are not critically dependent on the form of the model. The $\text{Ge}_{16}\text{As}_{35}\text{Te}_{28}\text{S}_{21}$ appears to be reasonably fit by a symmetric model without a thermally-activated mobility.

An example of a detailed quantitative analysis for $\text{Ge}_{15}\text{Te}_{81}\text{Sb}_{22}$ is given in Table VII. Ten sources of information are available for the determination of the model parameters: values of the activation energy for photoconductivity in the high- and intermediate-temperature regions, and for

the dark conductivity; values of the magnitude of the photoconductivity in the high-, intermediate- (both high and low intensities) and low-temperature regions, and of the dark conductivity; a value for the temperature dependence of the bandgap, $b = -6.6 \times 10^{-4}$ eV/K, obtained from the measured shift of the optical absorption edge near 300°K at the 1 percent transmission point; and a value of the ratio of the mobility in the low-temperature region μ_{LT} to the pre-exponential factor of the higher-temperature mobility μ_0 .

This last quantity, the mobility ratio μ_{LT}/μ_0 , is obtained as follows. If it is assumed that the exponential variation of the mobility continues at least somewhat below the temperature T' at which the intermediate-temperature photoconductivity begins to deviate from exponential variation with $1/T$, then T' can be interpreted as that temperature at which the demarcation levels are just passing through the density of effective recombination state "shoulders" at E_V^+ and E_C^+ .¹⁷ At the temperature at which the demarcation levels are just at E_V^+ and E_C^+ , the photoconductivity is given by

$$\Delta\sigma' = \frac{F \mu_0 e^{-E_g/kT}}{\left[C_V^0(E^+)(E^+) + \frac{\Delta n}{\Delta p} C_C^0(E^+)g(E^+) \right] kT}. \quad (21)$$

By comparing Eqs. (21) and (20), it is possible to write an expression for μ_{LT}/μ_0 , assuming $\Delta n \approx \Delta p$, in terms of the measured values of the low-temperature photoconductivity and the photoconductivity at T' .

All of the quantities listed in Table VII can then be expressed in terms of μ_0 and C^0 , for which reasonable values have been assumed to obtain the actual numbers listed in Table VII. Calculations were carried out for each of the three forms of the model for which energy values are given in Table VI. The room-temperature value of the mobility derived in this way is $0.2 \text{ cm}^2/\text{V-sec}$, varying with temperature with an activation energy $E_g = 0.11 \text{ eV}$, with a constant value of μ_{LT} at low temperatures. The

numbers obtained appear fairly reasonable, although there may be some internal discrepancy between the assumed form of the asymmetry (see note c in Table VI) in the asymmetrical forms of the model and the actual calculated values of $g_C(E^+)$ and $g_V(E^+)$.

If numerical values similar to those given in Table VII are calculated under the assumption that the C states lie close to the valence edge and the V states lie close to the conduction edge (the type of situation that might be expected if the assumed tails of band-like states were replaced by a conventional donor and acceptor model of imperfection states), the values so obtained are in almost every case less reasonable than those given in Table VII, and are in many cases beyond the range of possibility. Insofar as the model is applicable, therefore, it indicates that the C states can be considered as conduction-band-like in character lying near the conduction edge, and that the V states can be considered as valence-band-like in character lying near the valence edge.

Comparison of Tables I and VI shows that in the symmetric form of the model, the values of optical gap are larger than the values of the thermal gap, particularly for $\text{Ge}_{13}\text{Te}_{81}\text{Sb}_2$ and $\text{Si}_{11}\text{Ge}_{45}\text{As}_{35}\text{P}_{30}$. The asymmetric form of the model releases the constraint on the value of the gap and leaves it undetermined from photoconductivity and dark conductivity data alone. Since a number of reasons exist for thinking that the optical gap might be naturally larger, this disagreement in gaps does not constitute a compelling argument *per se* in favor of an asymmetric model.

CONCLUSIONS

A model based on sound semiconductor recombination statistics has been broadened, in accordance with the experimental data on the dependence of photoconductivity on intensity and temperature, to include three basic types of recombination process. This model is adequate for the description of previous published results, as well as for the more extensive measurements

on three chalcogenide alloys in the present investigation. Application of the model permits us to calculate a number of characteristic parameters of the localized level distribution and of the charge transport processes. The reasonable magnitudes of these values support the general validity of the model. It is hoped that the model can be used analytically in connection with further investigation involving material variations, in order to interpret electronic changes brought about by compositional alterations.

It should be recognized, however, that there are at least two major conclusions to which the model does not unambiguously lead. First, the model does not depend upon (or require) a particular "structure" in the density of localized states distribution in energy. What is required is that the density of effective recombination centers must be rapidly increasing as either the conduction edge or the valence edge is approached more closely than some critical energy. Such a variation of effective centers can indeed result from a real variation in the density of the centers with energy, but it can also result from a slowly-varying density of centers and a rapidly varying recombination rate coefficient with energy.

Second, the model does not depend in any critical way upon the actual variation of the density of effective recombination centers between 0 and E_v^* , or between E_v^* and E_c^* , or between E_c^* and E_g . As long as the density of effective recombination centers of V-type decreases rapidly as the energy exceeds E_v^* , and the density of effective recombination centers of C-type increases rapidly as the energy exceeds E_c^* , the general features of the model (except for factors of order unity) are preserved.

Application of the model to a greater range of measurements for a greater variety of materials may help to resolve these ambiguities.

TABLE I

Photoconductivity Parameters

	$\text{Ge}_{15}\text{Te}_{81}\text{Sb}_2$	$\text{Si}_{11}\text{Ge}_{11}\text{As}_{35}\text{P}_{35}\text{Te}_{40}$	$\text{Ge}_{16}\text{As}_{35}\text{Te}_{28}\text{S}_{21}$
E^+ , eV	0.16	0.19	(0.27) ^a
E^- , eV	0.18	0.20	0.30
E_g , eV	0.44	0.44	0.57
E_G^0 , eV ^b	0.95	1.07	1.25
E_{th} , eV ^c	0.33	-	-

^a Not measured directly but inferred from measured E^- and measured shift of T_{max} with intensity.

^b Optical bandgap at 0° K as obtained from measured optical absorption at 300° K and a temperature coefficient of -6×10^{-4} eV/degree. The measured value of the temperature coefficient for $\text{Ge}_{15}\text{Te}_{81}\text{Sb}_2$ is -6.6×10^{-4} eV/degree at 300° K, as determined from optical absorption at 1 percent transmission.

^c Activation energy deduced from the temperature dependence of thermoelectric power,¹¹ $\alpha = 0.23 + 10^3(0.35/T)$ mV/degree.

TABLE II

Recombination Coefficients

- $C_e^+(E)$ - capture coefficient for NL electron by hole in V level at E
 $C_h^-(E)$ - capture coefficient for NL hole by electron in C level at E
 $C_e^0(E)$ - capture coefficient for NL electron by empty C level at E
 $C_h^0(E)$ - capture coefficient for NL hole by electron-occupied V level at E
 $\tau(E, E')$ - transition rate coefficient for electron initially in C state at E recombining with hole in V state at E'.

Note: We assume that $C_e^+(E)$, $C_h^-(E)$ are Coulomb-attractive centers are much larger than $C_e^0(E)$, $C_h^0(E)$ as neutral centers.

TABLE III

Simplified Forms of $f_c(E)$ in Various Energy Ranges

Relevant Inequalities:

- Above (Below) $E_{in} + kT \ln 2$ $\sum_1 (E_{in} \downarrow)_1 < (>) \sum_j (E_{out} \uparrow)_j$
 Above (Below) $E_{fp} + kT \ln 2$ $\sum_1 (E_{in} \uparrow)_1 < (>) \sum_j (E_{out} \downarrow)_j$
 Above (Below) E_{dn}^c $\sum_j (E_{out} \downarrow)_j < (>) \sum_j (E_{out} \uparrow)_j$
 Above (Below) E_{dp}^c $\sum_1 (E_{in} \uparrow)_1 < (>) \sum_1 (E_{in} \downarrow)_1$

E_{in} , E_{fp} are respectively the steady-state electron and hole formal level energies.

E_{dn}^c , E_{dp}^c are respectively the electron and hole demarcation level energies for C states.

Simplified Forms of $f_c(E)$:

$$\begin{aligned}
 E > E_{dn}^c, \quad f_c(E) &\approx \sum_1 (E_{in} \downarrow)_1 / \sum_j (E_{out} \uparrow)_j \approx 2 \cdot e^{(E_{in} - E)/kT} \\
 E_{dp}^c < E < E_{dn}^c, \quad f_c(E) &\approx \sum_1 (E_{in} \downarrow)_1 / \sum_j (E_{out} \downarrow)_j < 1 \\
 E_{fp} + kT \ln 2 < E < E_{dp}^c, \quad f_c(E) &\approx \sum_1 (E_{in} \uparrow)_1 / \sum_j (E_{out} \downarrow)_j \approx 2 \cdot e^{(E - E_{fp})/kT} \\
 E < E_{fp} + kT \ln 2, \quad f_c(E) &\approx 1
 \end{aligned}$$

TABLE IV

Expressions for the Carrier Density for Symmetric Uniform and Exponential L State Distributions

	Uniform	"Diffuse" Exponential $T^* > T$	"Sharp" Exponential $T^* < T$
Small-signal $\Delta n \ll n_0$ High-temperature side of maximum	$\frac{F}{2 C^0 G K T \ln(C^\pm / 2C^0)}$	$\frac{F (C^0 / C^\pm)^{T/T^*} e^{(E_G - E_{f0})/KT^*}}{4 C^0 G K T [1 - (2C^0 / C^\pm)^{T/T^*}]}$	$\frac{F \left(\frac{1}{KT^*} - \frac{1}{KT} \right)}{4 C^\pm G} e^{(E_G - E_{f0})/KT}$
Large-signal $\Delta n \gg n_0$ Low-temperature side of maximum	$\frac{F}{2 C^0 G K T \ln \left[\frac{\Delta n^2}{n_0^2} \frac{C^\pm}{2 C^0} \right]}$	$\left(\frac{F}{4 C^0 G K T} \right)^{\frac{T^*}{T+T^*}} \left(N_c \frac{C^0}{C^\pm} \right)^{\frac{T}{T+T^*}}$	$\left[\frac{F N_c}{2 C^\pm G} \left(\frac{1}{KT^*} - \frac{1}{KT} \right) \right]^{1/2}$

TABLE V

Tests for Consistency between Photoconductivity and Dark Conductivity Activation Energies
for $\text{Ge}_{15}\text{Te}_{81}\text{Sb}_2\text{S}_2$

Model	E^+ , eV	E^- , eV	Predicted E_σ , eV	Measured E_σ , eV
Symmetric NL to L Transitions Only No Mobility Activation Energy	$\frac{E_0}{2} - E^*$ 0.16	$\frac{E^*}{2}$ 0.18	$\frac{E_0}{2}$ 0.52	0.44
Symmetric NL to L Transitions Only Mobility Activation Energy, E_μ	$\frac{E_G}{2} - E^* - E_\mu$ 0.16	$\frac{E^*}{2} + E_\mu$ 0.18	$\frac{E_G}{2} + E_\mu$ $0.52 + 2 E_\mu$	0.44
Symmetric L to L Transitions in Intermediate- Temperature Range Mobility Activation Energy, E_μ NL to L Transitions in High-Temperature Range	$\frac{E_G}{2} - E^* - E_\mu$ 0.16	$E^* + E_\mu$ 0.18	$\frac{E_G}{2} + E_\mu$ $0.34 + E_\mu$	0.44 (Indicates $E_\mu = 0.1$ eV)

TABLE VI

Characteristic Energy Values as Obtained from Experiment by Application of the Model

Material	Model Form	E_v^0 , eV ^a	E_c^0 , eV ^a	E_{fo}^0 , eV	E_{μ} , eV
$Ge_{15}Te_{81}Sb_2S_2$	Symmetric, Transition 1 dominant at high T	0.08	0.60	0.34	0.10
	Asymmetric, ^c Transition 1 dominant at high T	(0.07) ^b	0.60	(0.33) ^b	(0.11) ^b
	Asymmetric, ^c Transitions 2 dominant at high T	(0.07) ^b	(0.67) ^b	(0.33) ^b	(0.11) ^b
$Si_{11}Ge_{11}As_{35}P_3Te_{40}$	Symmetric, Transition 1 dominant at high T	0.15	0.63	0.39	0.05
$Ge_{16}As_{35}Te_{28}S_{21}$	Symmetric, Transition 1 dominant at high T	0.30	0.84	0.57	0.00

$$^a E_v^* = E_v^0 - bT(E_v^0/E_G^0) ; E_c^* = E_c^0 - bT(E_c^0/E_G^0) ; E_{fo} = E_{fo}^0 - bT$$

^b Values not determinate from photoconductivity alone; value of $E_{fo}^0 = 0.33$ eV obtained from thermoelectric data

$$^c N_c < N_v ; (E_G - E_c^*) > E_v^* ; \epsilon_c(E_c^*) < \epsilon_v(E_v^*) ; E_{fo} < E_G/2$$

TABLE VII

Numerical Values of Parameters *

for $Ge_{15}Te_{81}Sb_2S_2$ for the Models Listed in Table VI

Parameter	Symmetric, Transition 1 dominant at high T	Asymmetric, Transition 1 dominant at high T	Asymmetric, Transition 2 dominant at high T
μ_{LT} , cm ² /V-sec	0.0036	0.0012	0.0012
C^- , cm ³ /sec	9×10^{-8}	Undetermined	Undetermined
$\epsilon_c(E_c^*)$, cm ⁻³ eV ⁻¹	1.5×10^{19}	$(1.4 \times 10^{20})^a$	10^{20}
K , cm ³ /sec	2.1×10^{-7}	2.3×10^{-6}	2.3×10^{-8}
$\epsilon_v(E_v^*)$, cm ⁻³ eV ⁻¹	1.5×10^{19}	1.1×10^{19}	1.1×10^{19}
N_v , cm ⁻³	2.8×10^{18}	1.2×10^{19}	1.2×10^{19}
$K^+ N_{fo}$, sec ⁻¹	2.0×10^6	1.3×10^7	1.3×10^7

* Assuming values of $\mu_{fo} = 10$ cm²/V-sec and $C^0 = 10^{-9}$ cm³/sec.

^a Determinable only if C^- of symmetric case is assumed to hold;
 $\epsilon_c(E_c^*) \propto 1/C^-$.

FIGURE CAPTIONS

Figure 1. Dark conductivity and AC photoconductivity (16 Hz chopping rate) as a function of temperature for $\text{Ge}_{15}\text{Te}_{81}\text{Sb}_2\text{S}_2$ (1.1 micron thick sputtered sample, coplanar electrodes) for different photo-excitation intensities. Excitation was by a 100W tungsten-halogen lamp with color temperature of about 3000°K and maximum output at 1.06 microns; $f = 1$ corresponds to an incident flux of 1.36×10^{17} photons $\text{cm}^{-2} \text{sec}^{-1}$, evaluated at 1.06 microns. An absorption constant of $2.6 \times 10^4 \text{ cm}^{-1}$ was measured at 1.06 microns and used to calculate the excitation density. The dashed portions of the photoconductivity curves at low excitation intensities correspond to photoconductivity response times comparable to or greater than the reciprocal of the chopping rate.

Figure 2. Dark conductivity and AC photoconductivity as a function of temperature for (a) $\text{Si}_{11}\text{Ge}_{45}\text{As}_{35}\text{P}_{340}$, evaporated layer, coplanar electrodes; and (b) $\text{Ge}_{16}\text{As}_{35}\text{Te}_{28}\text{S}_{21}$, evaporated layer, coplanar electrodes. Conditions are similar to those for Figure 1 but not necessarily quantitatively identical.

Figure 3. (a) Schematic energy level diagram for the proposed model. Localized states extend into the mobility gap from the conduction and valence edges. With increasing energy above the valence edge, the density of effective recombination centers (see text) decreases sharply as the energy exceeds E_v^* for V states, and increases sharply as the energy exceeds E_c^* for C states. The equilibrium Fermi level lies E_{F0} above the valence edge; since the conductivity is p-type, $E_{F0} \leq E_g/2$. (b) Typical transitions between individual states in the distribution shown in (a). In the high-temperature range, transitions 1 or 2 dominate; in the intermediate-temperature range, transition 2 dominates at high intensities and transition 3 at low

REFERENCES

1. W. Shockley and W.T. Read, *Phys. Rev.* **87**, 835 (1952)
2. B.T. Kolomiets and V.M. Lyubin, *Sov. Phys.-Solid State* **2**, 46 (1960)
3. B.T. Kolomiets and V.M. Lyubin, *Sov. Phys.-Solid State* **4**, 291 (1962)
4. E. Fagen and H. Fritzsche, *J. Non-Cryst. Solids* **4**, 480 (1970)
5. W.E. Howard and R. Tsu, *Phys. Rev. B*, **4**, 4709 (1970)
6. K. Weiser, R. Fisher, and M.H. Brodsky, *Proc. 10th Internat. Semicond. Conf.*, Cambridge, Mass., p. 667 (1970)
7. B.T. Kolomiets and E.H. Raepopova, *Sov. Phys.-Semicond.* **4**, 1041 (1971)
8. V.I. Kruglov and L.P. Strakhov, *Sov. Phys.-Semicond.* **4**, 1316 (1971)
9. B.T. Kolomiets, Yu.V. Rukhlyadev, and V.P. Shilo, *J. Non-Cryst. Solids* **5**, 389, 402 (1971)
10. First Semi-Annual Technical Report to ARPA by Energy Conversion Devices, Inc., on Contract DAKC15-70-C-0187, June 1971.
11. H.K. Rockstad, R.A. Flasck, and S. Iwasa, 4th Internat. Conf. on Amorph. and Liquid Semicond., Ann Arbor, Michigan, August 1971, Paper DA4.
12. M.H. Cohen, H. Fritzsche and S.R. Ovshinsky, *Phys. Rev. Letters* **22**, 1065 (1969)
13. J.G. Simmons and G.W. Taylor, 4th Internat. Conf. on Amorph. and Liquid Semicond., Ann Arbor, Michigan, August 1971, Papers JB3 and JB4.
14. R. Fischer, U. Heim, F. Stern and K. Weiser, *Phys. Rev. Letters* **26**, 1182 (1971)
15. H. Fritzsche, *J. Non-Cryst. Solids* **5**, 49 (1971); H. Rockstad, *J. Non-Cryst. Solids* **2**, 192 (1970)
16. In changing the limits in this way, we have implicitly assumed that it is the density of states functions, $g_c(E)$ and $g_v(E)$, themselves which undergo an abrupt change with energy. The form of the results is not changed by this assumption.
17. This interpretation is certainly appropriate at least for high intensities in the intermediate-temperature region, from which the data were taken for the calculation.

intensities; in the low-temperature region, transitions 4 dominate.

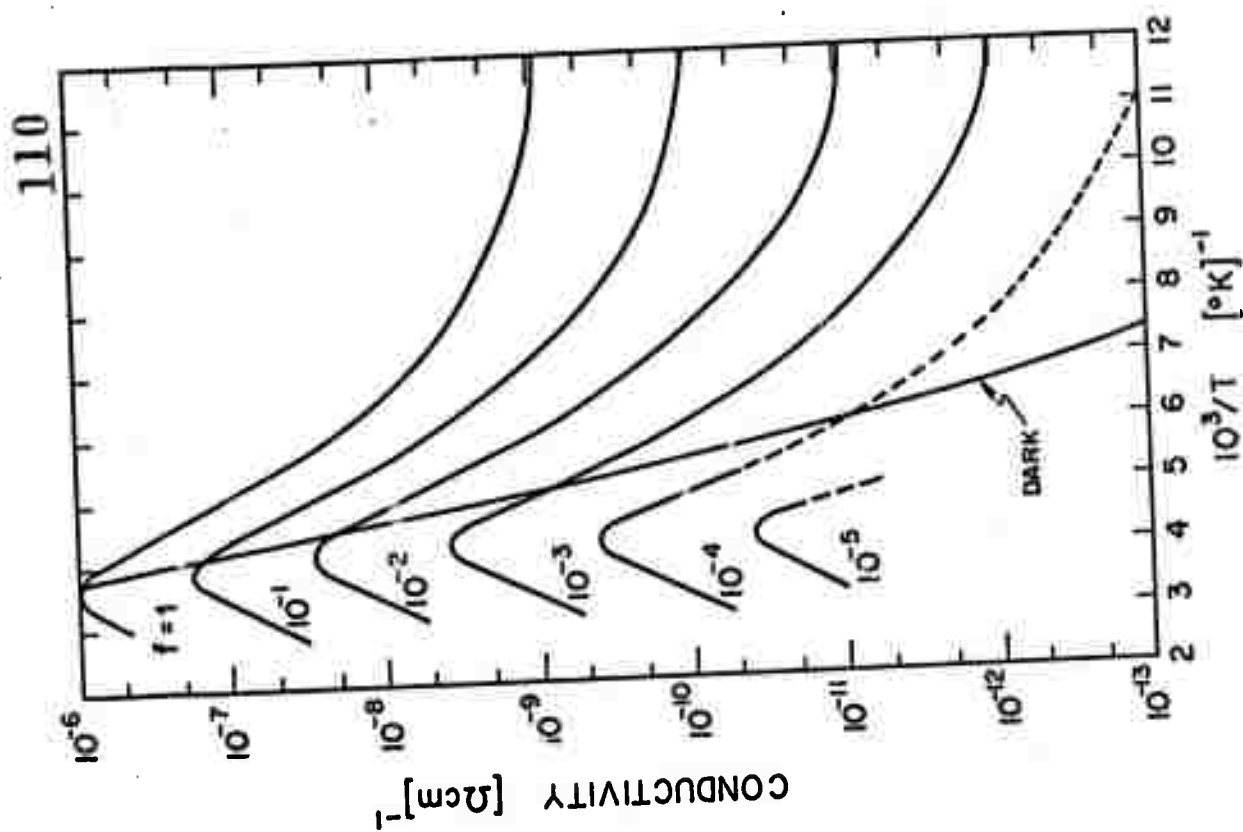


Fig. 1

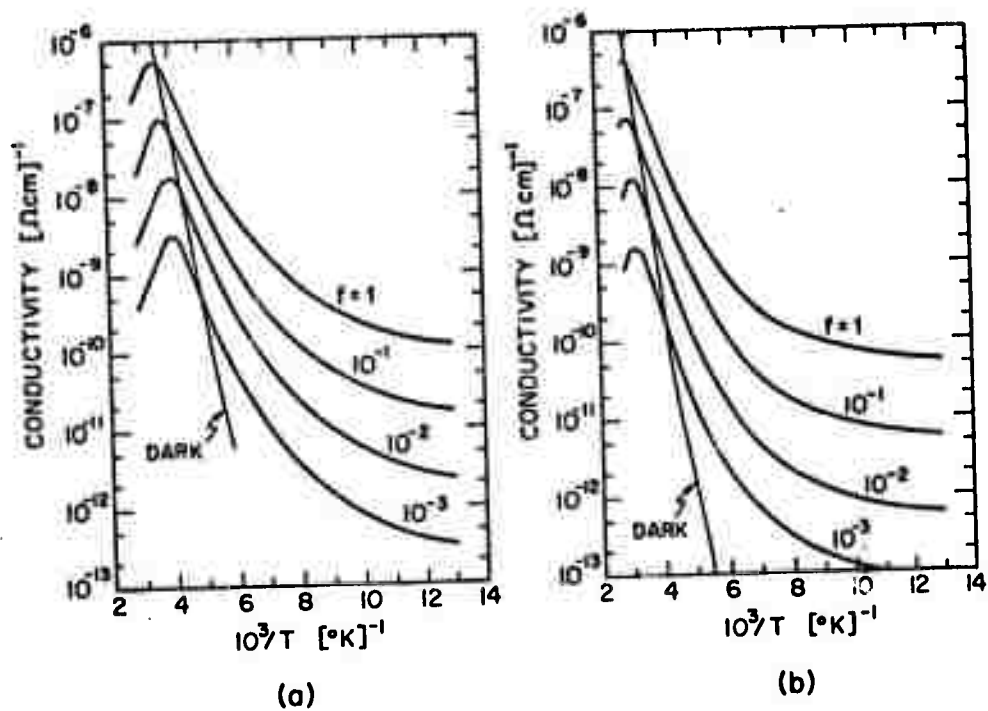
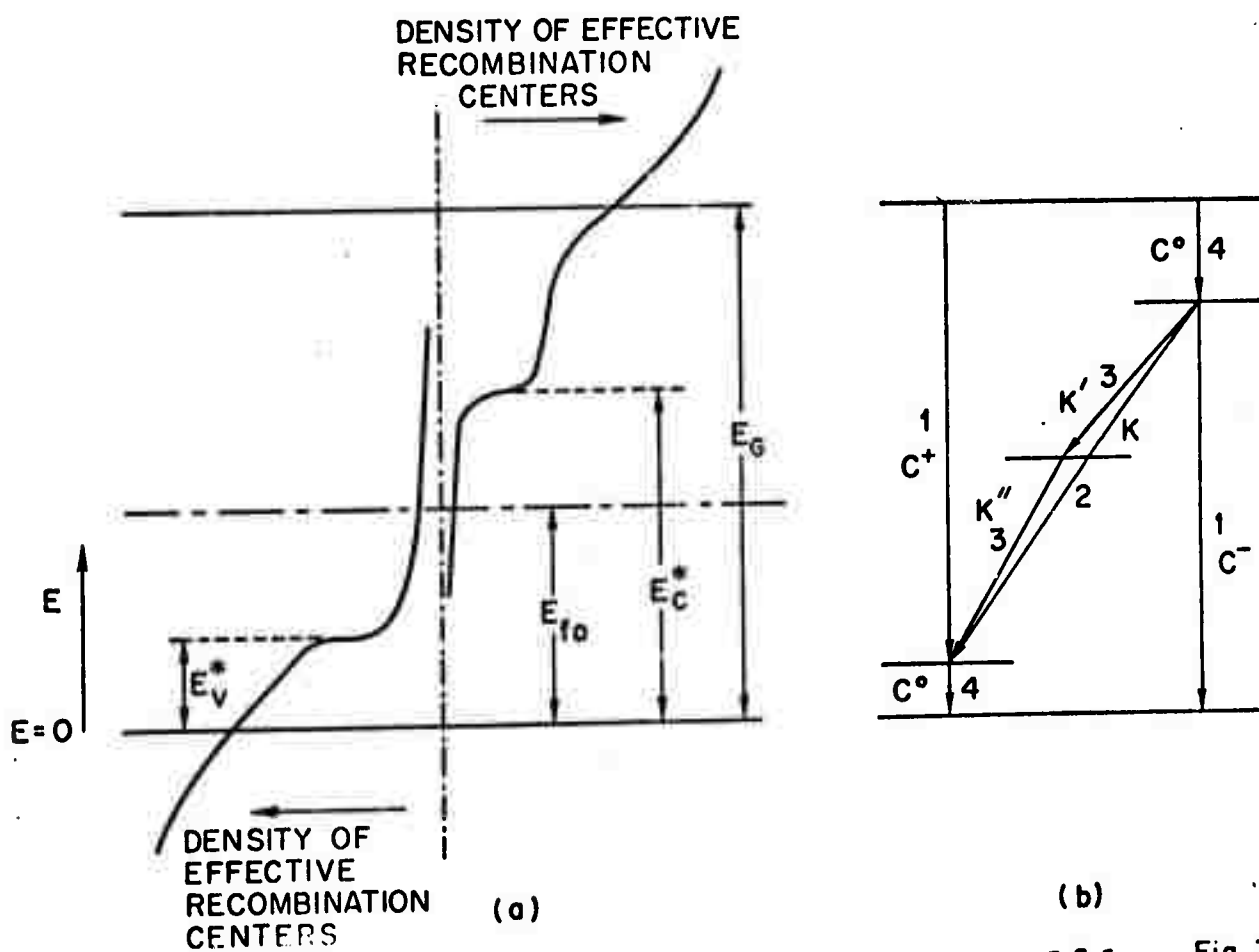


Fig. 2



(b)